UNIVERSITY OF CALIFORNIA, MERCED

Models of vascular development

A dissertation submitted in partial satisfaction of the requirements for the degree of Doctor of Philosophy

in

Materials and Biomaterials Science and Engineering

by

Jose E. Zamora Alvarado

Committee in charge:
Professor Kara E. McCloskey, Primary Advisor
Professor Joel Spencer, Chair
Professor Ajay Gopinathan
Professor Jennifer Manilay

The Dissertation of Jose E. Zamora Alvarado is approved, and it is acceptable in quality and form for publication on microfilm and electronically

_____

Professor Kara E. McCloskey, Primary Advisor

_____

Professor Joel Spencer, Chair

_____

Professor Ajay Gopinathan

_____

Professor Jennifer Manilay

University of California, Merced
2024

ACKNOWLEDGEMENTS

The research in this document was supported and funded by the NSF-Science and Technology Center (STC) for the Emergent Behavior of Integrated Biological Systems (EBICS) Award no. 0939511, Center for Engineering MechanoBiology (CEMB), an NSF Science and Technology Center, under grant agreement CMMI: 15-48571, and NSF-CREST: Center for Cellular and Biomolecular Machines Fellowship award numbers NSF-HRD-1547848 and NSF-HRD-2112675.

CURRICULUM VITAE

Jose E. Zamora Alvarado

jzamora@ucmerced.edu | (661) 577-2737
www.linkedin.com/pub/jose-zamora/86/88b/740/

EDUCATION

Ph.D., Materials and Biomaterials Science and Engineering. **Spring 2017 – Spring 2024**
University of California, Merced
GPA: 3.97

Dissertation Title: Models of Vascular Development
Ph.D. Candidate
Anticipated graduation date: 2024
Advisor: Kara E. McCloskey, PhD
Co-Advisor: Ajay Gopinathan, PhD

M.S. Materials and Biomaterials Science and Engineering **Spring 2020**
University of California, Merced
Dissertation Title: Experimental and Computational Models of Vascular Development

B.S. Biological Sciences, B.S. Physics **Fall 2016**
University of California, Merced

- Biology B.S. – Emphasis on Human Biology
- Physics B.S. – No Emphasis

RESEARCH EXPERIENCE

Graduate Researcher
Dr. Kara McCloskey and Dr. Ajay Gopinathan **Spring 2017 – Present**
University of California, Merced

Field: Cardiovascular tissue engineering and its integration with Biophysics.
Project 1: I am developing a computational model that explores the relative importance of biological processes in cellular organization. The goal is to explore the extend that stem cell differentiation impacts organization in developing tissues.
Project 2: I'm building a platform for long term (months) development of functional and perfusable vascular networks (in vitro blood vessels) for future incorporation into organoid models.

Undergraduate Researcher
Dr. Kara McCloskey **May 2014 – Fall 2016**
University of California, Merced

Project: Site Directed Differentiation of Stem Cells using Insoluble vascular endothelial growth factor (VEGF).

- *I showed via flow cytometry that insoluble VEGF was more than sufficient to differentiate stem cell into vascular progenitor cells (VPC, Flk-1 positive cells)*
- *Later showed that no VEGF was needed to produce VPCs*

Undergraduate Researcher
Dr. Ajay Gopinathan **Summer 2015 –Fall 2016**

University of California, Merced

- *Computational modeling of vessel formation.*
- *Use Traction force microscopy to explore force generated by differentiating stem cells.*

TEACHING

Technical Writing - Lab Sections (ENGR 156, TA) **Spring 2023**
University of California, Merced
Polymeric Materials - Discussion/Lab Sections (MBSE 224, TA) **Fall 2020**
University of California, Merced
Mech Behavior of Materials - Discussion/Lab Sections (MSE 121, TA) **Fall 2020**
University of California, Merced
Kinetics and Processing - Discussion/Lab Sections (MSE 111, TA) **Fall 2020**
University of California, Merced
Nanodevice Fabrication - Discussion/Lab Sections (MSE 126, TA) **Spring 2020**
University of California, Merced
Introduction to Modern Physics - Discussion/Lab Sections (PHYS 10, TA) **Fall 2019**
University of California, Merced
Instructor for Introduction to Material Science - Discussion/Lab Sections (ENGR 45, TA) **Spring 2019**
University of California, Merced
Instructor for Introduction to Material Science - Discussion/Lab Sections (ENGR 45, TA) **Spring 2018**
University of California, Merced

FELLOWSHIPS

Dissertation Fellowship
University of California, Merced

- *Recipient of Graduate Deans Dissertation Fellowship* **Spring 2022**

Central Valley Fellowship
University of California, Merced

- *Recipient Central Valley Fellowship* **Fall 2021**

NSF-CREST: Center for Cellular and Bio-Molecular Machines (CCBM)
University of California, Merced

- *Recipient of Summer NSF-CREST Fellowship* **Summer 2023**
- *Recipient of NSF-CREST Scholar Mentor Fellowship* **Spring 2023**
- *Recipient of NSF-CREST Scholar Mentor Fellowship* **Fall 2022**
- *Recipient of Semester NSF-CREST Fellowship* **Fall 2022**
- *Recipient of NSF-CREST Scholar Mentor Fellowship* **Summer 2022**
- *Recipient of Semester NSF-CREST Scholar Mentor Fellowship* **Fall 2021**
- *Recipient of NSF-CREST Scholar Mentor Fellowship* **Summer 2021**
- *Recipient of Semester NSF-CREST Fellowship* **Spring 2021**
- *Recipient of Semester NSF-CREST Scholar Mentor Fellowship* **Spring 2021**
- *Recipient of Semester NSF-CREST Scholar Mentor Fellowship* **Fall 2020**
- *Recipient of Semester NSF-CREST Scholar Mentor Fellowship* **Spring 2020**
- *Recipient of Semester NSF-CREST Fellowship* **Fall 2018**
- *Recipient of Semester NSF-CREST Fellowship* **Fall 2017**
- *Recipient of Semester NSF-CREST Fellowship* **Spring 2017**

Materials and Biomaterials Science and Engineering Summer Fellowship
University of California, Merced

- *Recipient of MBSE Fellowship* **Summer 2022**
- *Recipient of MBSE Fellowship* **Summer 2021**
- *Recipient of MBSE Fellowship* **Summer 2020**

Biological Engineering and Small-scale Technologies Summer Fellowship
University of California, Merced

- *Recipient of BEST Fellowship* **Summer 2019**
- *Recipient of BEST Fellowship* **Summer 2018**
- *Recipient of BEST Fellowship* **Summer 2017**

RESEARCH TRAINING AWARDS

NSF-CREST: Seed Project Award ($5000) **Spring 2020**
Recipient of the CCBM's Seed project award to explore vascular network formation.
Collaboration with Dr. Joel Spencer
University of California, Merced

NSF-CREST: Summer Hands-on Training Modules
University of California, Merced

- *Selected for NSF-CREST Spectroscopy and Imaging workshop.* **Summer 2018**
- *Selected for NSF-CREST NanoBiofabrication workshop.* **Summer 2017**
- *Selected for NSF-CREST Scientific Computing workshop.* **Summer 2017**

NSF: Interdisciplinary Computational Graduate Education Program **Spring 2017**
University of California, Merced

NSF-CREST: Center for Cellular and Bio-Molecular Machines (CCBM) (Undergraduate Scholar) **Fall 2016**
University of California, Merced

Physics: Undergraduate Research Grant **Summer 2016**
University of California, Merced

NanoBio Research Program (Summer Workshop) **Summer 2015**
University of Illinois at Urbana-Champaign

Center of Integrated Nanomechanical Systems (COINS) REU **Summer 2014**
University of California, Merced

AWARDS AND ACHIVEMENTS

Most Outstanding Graduate Student Award **AY 2020-21**
University of California, Merced

PUBLICATIONS

1. Patrick S Noerr, **Jose E Zamora Alvarado** , Farnaz Golnaraghi, Kara E. McCloskey, Ajay Gopinathan , Kinjal Dasbiswas; *Optimal mechanical interactions direct multicellular network formation on elastic substrates,* PNAS. **(**2023-02-06). https://doi.org/10.48550/arXiv.2205.14088

2. Drew E. Glaser, William S. Turner, Nicole Madfis, Lian Wong, **Jose Zamora**, Nicholas White, Samuel Reyes, Andrew B. Burns, Ajay Gopinathan and Kara E. McCloskey; *Multifactorial Optimizations for Directing Endothelial Fate from Stem Cells,* PlosOne. http://dx.doi.org/10.1371/journal.pone.0166663

MANUSCRIPTS SUBMITTED

- **Jose E. Zamora Alvarado**, Ajay Gopinathan, & Kara E. McCloskey, (*2023),* Motility and Proliferation Drive the Emergence of Patterns in Co-cultures of Differentiating Vascular Progenitor Cells (Submitted to PlosOne)

- Rachel Hatano, Ariell M. Smith, Ritu Raman, **Jose E. Zamora**, Rashid Bashir, Kara McCloskey (2023), Comparing Fabrication Techniques for Engineered Cardiac Tissue (Submitted to JBMR)

MANUSCRIPTS IN PREPARATION

- Metzli I. Montero, Pravien Rajaram, **Jose E. Zamora Alvarado**, Roberto Andresen Eguiluz, Kara McCloskey, Ryan Baxter, (*2023), Cannabidiol Toxicity driven by Hydroxyquinone Formation* (**Manuscript**)
- **Jose E. Zamora Alvarado**, Diana Cruz-Garcia, Jessalyn Arteta, Kara E. McCloskey, (*2023*), *Perivascular tri-cultures generate perfusable vasculature* (**Manuscript**)

PRESENTATIONS

- **Jose E. Zamora**, Kara E. McCloskey. "Mural Cell Signaling in Perfusable Vasculature" BMES 2022 Conference, San Antonio, TX. October 12-15, 2022. *Talk*
- **Jose E. Zamora**, Kara E. McCloskey. "Role of Mural Cell Signaling in Microvascular Dimensions and Stability" BMES 2022 CMBE Conference, Indian Wells, CA. January 3-7, 2022. *Poster*
- **Jose E. Zamora**, Mikahl Banwarth-Kuhn, Suraj Sahu, Ajay Gopinathan, Suzanne Sindi, Kara E. McCloskey. "Experimental and Computational Models of Vascular Development" CCBM Seminar, UC Merced, CA. November 9, 2021. *Talk*
- **Jose E. Zamora**, Mikahl Banwarth-Kuhn, Ajay Gopinathan, Suzanne Sindi, Kara E. McCloskey. "Experimental and Computational Models of Vascular Development" SLAAM Seminar, UC Merced, CA. April 5, 2021. *Talk*
- **Jose E. Zamora**, Ajay Gopinathan, Kara E. McCloskey. "Stochastic Spatial and Temporal Population-based Model For Co-emergence of Vascular Patterns" MathBio Seminar, UC Merced, CA. March 3, 2020. *Talk*
- **Jose E. Zamora**, Kara E. McCloskey. "Perivascular bi- and tri- cultures with smooth muscle cells generate perfusable vasculature" EBICS Retreat, Atlanta, GA. July 29-21, 2019. *Talk*
- **Jose E. Zamora**, Ajay Gopinathan, Kara E. McCloskey. "Stochastic Spatial and Temporal Population-based Model For Co-emergence of Vascular Patterns" EBICS Retreat, Atlanta, GA. July 29-31, 2019. *Poster*
- **Jose E. Zamora**, Ajay Gopinathan, Kara E. McCloskey. "Stochastic Spatial and Temporal Population-based Model For Co-emergence of Vascular Patterns" UC BioSymposium, UC Merced, CA. June 21-23, 2019. *Talk*
- **Jose E. Zamora**, Ajay Gopinathan, Kara E. McCloskey. "Stochastic Spatial and Temporal Population-based Model For Co-emergence of Vascular Patterns" NSF-CREST Open house, UC Merced, CA. October 23, 2018. *Poster*
- **Jose E. Zamora**, Ajay Gopinathan, Kara E. McCloskey. "Stochastic Spatial and Temporal Population-based Model For Co-emergence of Vascular Patterns" BMES, Atlanta, GA. October 17, 2018. *Poster*

- **Jose E. Zamora**, Ajay Gopinathan, Kara E. McCloskey. "Stochastic Spatial and Temporal Population-based Model For Co-emergence of Vascular Patterns" UC Systemwide Bioengineering Symposium, UC Riverside, CA. June 21, 2018. *Talk*

- **Jose E. Zamora**, Ajay Gopinathan, Kara E. McCloskey. "Modeling Blood Vessel Formation" University Friends Circle, Merced, CA. April 3, 2018. *Grad Slam Talk*
- **Jose E. Zamora**, Ajay Gopinathan, Kara E. McCloskey. "Modeling Blood Vessel Formation" Lazar Piro Hosted Event featuring Chancellor Dorothy Leland, Turlock, CA. March 28, 2018. *Grad Slam Talk*
- **Jose E. Zamora**, Ajay Gopinathan, Kara E. McCloskey. "Exploring Vascular Development from the Cell's Perspective" EBICS NSF site visit, MIT, Cambridge, Massachusetts. January 11, 2018. *poster*
- **Jose E. Zamora**, Ajay Gopinathan, Kara E. McCloskey. "Spatial Patterning of Vascular Cell Fate" BMES 2017, Phoenix, Arizona, October 12, 2017. *poster*
- **Jose E. Zamora**, Ajay Gopinathan, Kara E. McCloskey. "Spatial Patterning of Vascular Cell Fate" CCBM Open House, UC Merced, California, September 2017. *poster*
- **Jose E. Zamora**, Ajay Gopinathan, Kara E. McCloskey. "Understanding Vascular Cell Differentiation from A Cell's Perspective" CCBM External Advisory Board Meeting, UC Merced, California, August 2017. *oral presentation*
- **Jose E. Zamora**, Ajay Gopinathan, Kara E. McCloskey. "Spatial Patterning of Vascular Cell Fate" CCBM External Advisory Board Meeting, UC Merced, California, August 2017. *poster*
- **Jose E. Zamora**, Ajay Gopinathan, Kara E. McCloskey. "Modeling Angiogenesis" Semi-Finalist: GradSLAM, UC Merced, California, April. 2017. *oral presentation*
- **Jose E. Zamora**, Ajay Gopinathan, Kara E. McCloskey. "Modeling Vascularization: Calculating spatial patterns for emerging co-populations" Physics Senior Thesis Defense, UC Merced, California, December 2016. *oral presentation*
- **Jose E. Zamora**, Ryan Burtzlaff, Nicholas S. White, Drew E. Glaser, Kara E. McCloskey. "Site Directed Differentiation of Stem Cells using Insoluble VEGF" Summer 2015 NanoBio Research Program, UIUC, Illinois, August 2015. *poster*
- **Jose E. Zamora**, Ryan Burtzlaff, Nicholas S. White, Drew E. Glaser, Kara E. McCloskey. "Site Directed Differentiation of Stem Cells using Insoluble VEGF" UIUC Workshop, UIUC, Illinois, April 2015. *poster*
- **Jose E. Zamora**, Ryan Burtzlaff, Nicholas S. White, Drew E. Glaser, Kara E. McCloskey. "Site Directed Differentiation of Stem Cells using Insoluble VEGF" BMES 2014 Annual Meeting, San Antonio, Texas, October 25. *poster*
- **Jose E. Zamora**, Ryan Burtzlaff, Nicholas S. White, Drew E. Glaser, Kara E. McCloskey. "Site Directed Differentiation of Stem Cells using Insoluble VEGF" Center of Integrated Nanomechanical Systems (COINS) Summer research poster presentation, UC Merced, CA, August 2014. *poster*

TECHNIQUES & SKILLS

- Computational languages: MATLAB (Proficient), Python (Proficient), Jupiter Notebook (Proficient), Linux (Intermediate), Java (intermediate), R (Novice)
- Cell Culture: Mouse embryonic stem cells (R1, A3, B2), endothelial cells (HUVEC, RAOEC, MCEC), Smooth muscle cells (RAOSMC, HuASMC), Pericytes (HAP), Human Stem cells (H9, HIPSC)
- Instrumentation: Microscopy (Scanning electron, confocal, fluorescent), Flow Cytometry (BD LSR II, ARIA II & III), Clean Room (Positive and Negative Lithography, Electrospinning, PDMS processing)
- Software: Word, PowerPoint, Excel, Prism, Flowjo, ImageJ

MENTORSHIP

Graduate Mentees:

- **Kaycee Change,** UC Merced, BEST Program **Fall 2018 – Spring 2019**
- **Nastaran Abbasizadeh,** UC Merced, BEST Program **Fall 2018 – Spring 2019**
- **Vaishnavi Girish,** UC Merced, BEST Program **Fall 2018 – Spring 2019**
- **Victor Hernandez,** UC Merced, BEST Program **Fall 2018 – Spring 2019**
- **Wenyan Guan,** UC Merced, BEST Program **Fall 2018 – Spring 2019**
- **Yile Fang,** UC Merced, MBSE Program **Spring 2019**

Undergraduate Mentees:

- **Tyler Guedry,** UC Merced BioChemistry Major**,** C-SIP scholar **Summer 2020 – Spring 2023**
  - Mentored, trained, and aided in his own research project. He presented at the summer symposium.
- **Jessalyn Arteta,** UC Merced Biology Major**,** C-SIP scholar **Summer 2020 – Spring 2023**
  - Mentored, trained, and aided in his own research project. She presented BMES.
- **Jacob Espinosa,** UC Merced BioEngineering Major**,** CAMP-REU scholar **Summer 2019 – present**
  - Mentored, trained, and aided in his own research project. He presented at the summer symposium.
- **Diana Cruz Garcia,** UC Merced BioEngineering Major**,** UC LEADS scholar **Summer 2019 – present**
  - Mentored, trained, and aided in her own research project. She presented at the summer symposium.
- **Win Teavir,** UC Merced Biology Major**,** UCLEADS scholar **Fall 2020 – Spring 2021**
  - Mentored, trained.
- **Maha Zaman,** UC Merced BioEngineering Major **Fall 2019 – Spring 2020**
  - Mentored, trained, and aided in her own research project.
- **Jallil Mancera,** UC Merced**,** human Biology Major **Summer 2019**
  - Mentored, trained, and aided in her own research project.
- **Cassandra Maldonado,** UC Merced Biology Major**,** CREST-CCBM scholar **Summer 2018 – 2019**
  - Summer REU student from Merced Community College. She presented at summer symposium.
- **Alexis Zamudio-Torres,** UC Merced Biology Major**,** SURF-REU scholar **Summer 2017 – 2019**
  - Mentored, trained, and aided in his own research project. He presented at summer symposium.
- **Cheukho Lui,** UC Merced BioEngineering **Spring 2018**
  - Undergraduate researcher, I trained in tissue culture.

High school Mentees:

- **Eduardo Guzman,** Science and Technology Enrichment Program (STEP)-NSF CREST **Summer 2018**
  - Summer High School student
  - Mentored, trained, and helped him get a close look into a research setting.
- **Emily Hernandez,** Science and Technology Enrichment Program (STEP)-NSF CREST **Summer 2018**
  - Summer High School student
  - Mentored, trained, and helped her get a close look into a research setting. Also, helped with College planning and application preparations.
- **Eugene Vang,** Science and Technology Enrichment Program (STEP)-NSF CREST **Summer 2017**
  - Summer High School student
  - Mentored, trained, and helped him get a close look into a research setting. Also, helped with College planning and application preparations.

LEADERSHIP

NSF CREST Student Leadership Council **Fall 2017 – 2021**
University of California, Merced
Arrange events with CREST fellows and scholars to foster a sense of community and discuss areas where the CREST center can improve.

Graduate Student Representative for TAPS Advisory Committee **Fall 2019 – 2021**
University of California, Merced
Arrange events with CREST fellows and scholars to foster a sense of community and discuss areas where the CREST center can improve.

NSF EBICS Student Leadership Council **Fall 2017 – Summer 2019**
University of California, Merced
Collaborations between multiple institutions to foster a sense of community and improve EBICS graduate student outreach and education.

Executive Board Member and Ambassador **Spring 2014 – Spring 2016**
UC Merced's Police Mentor program
University of California, Merced
Responsible for ensuring that UC Merced mentors had access to local elementary schools. Inspired local youth to pursue higher education rather than drugs or violence.

Founder/President **Spring 2013 – Fall 2015**
The Astronomy Club at UC Merced
University of California, Merced
Arranged stargazing outreach events, wrote grants to fund the purchase of new telescopes, guest lectured at local elementary schools, and lead discussions related to astronomy.

PROFESSIONAL EXPERIENCE

Undergraduate Student Assistant, Graduate Division **September 2015 – Fall 2016**
University of California, Merced

Summer Conference Assistant, Housing and Residence Life **June 2015 – August 2015**
University of California, Merced

Office Assistant, Housing and Residence Life **August 2013 – May 2015**
University of California, Merced

Maintenance Assistant, Housing and Residents Life **Summer 2013**
University of California, Merced

Construction Worker **Summer of 2011 & 2012**
Superior Construction

Cashier **August 2010 – July 2011**
Jack in the Box

SERVICE & OUTREACH

Lab Tours

Lead tours to visiting K12 students, California central valley community members, and UC Merced students.

- **MBSE recruitment – Grad recruitment -** *"Cardiovascular lab tour"* **Spring 2020**
- **Burbank elementary school visit –** "Astronomy tour" **Fall 2019**
- **NSF CREST – STEM Camp -** *"Cardiovascular lab tour!"* **Summer 2019**
- **NSF CREST – CREST Science and computing research Summer Program -** *"Cardiovascular lab tour!"* **Summer 2019**
- **NSF CREST – CREST STEP -** *"Cardiovascular lab tour!"* **Summer 2019**
- **NSF CREST – CREST Open House -** *"Cardiovascular lab tour!"* **Fall 2018**
- **NSF CREST – Patterson High School** *"Why Bioengineering is cool!"* **Fall 2018**
- **NSF EBICS – Merced County Track Team Visit** *"What is Bioengineering?"* **Spring 2018**
- **NSF CREST – Tulare Board of Trustee Visit** *"What is a Stem Cell?"* **Fall 2017**
- **Merced nAnomaterials Center for Energy and Sensing (MACES) – Beyer High School Visit** *"What does it mean to be a Stem Cell?"* **Fall 2017**
- **NSF CREST Open House** **Fall 2017**
- **NSF CREST Elementary school visit** **Fall 2017**

Guest Scientist

Presented and facilitated discussions surrounding popular science topics.

- **S.T.E.A.M Center, Merced,** *"Why did I go into research"* **Fall 2018**
- **Our Lady of Fatima Catholic Elementary School, Modesto,** *"Stem Cells for Young Scientist"* **Spring 2018**
- **CSU Stanislaus Science Day** *"Should We Engineer the Mosquito?"* **Fall 2017**
- **Our Lady of Fatima Catholic Elementary School, Modesto,** *"Effects of Climate Change"* **Spring 2017**
- **Our Lady of Fatima Catholic Elementary School, Modesto,** *"Astronomy 101"* **Spring 2016**

Models of Vascular Development

by

Jose E. Zamora Alvarado

in

Materials and Biomaterials Science and Engineering

UNIVERSITY OF CALIFORNIA, MERCED

Committee in charge:
Professor Kara E. McCloskey, Primary Advisor
Professor Joel Spencer, Chair
Professor Ajay Gopinathan
Professor Jennifer Manilay

ABSTRACT

Developing vascular cells have been shown to self-organize into unique structures in both two and three dimensions. Depending on the conditions, these cells may develop micropatterns with spatial segregation of different cell types in 2D or develop into perfusable vascular vessels in 3D. This self-organization arises from the interplay of motility, proliferation, differentiation, and cellular signaling; with the relative importance of these factors remaining unclear. In this dissertation, I report the development and use of a computational model to explore how motility, proliferation, and differentiation rates affect the emergence of micropatterns from differentiating vascular cells in a 2D *in silico* environment. Later, I explore the *in vitro* vascular development, via a microfluidic platform, of vascular networks that are functional, perfusable, and stable for more than two months. Firstly, I developed a stochastic on-lattice population-based model to study the emergence of vascular patterns from a starting distribution of stem cell induced vascular progenitor cells capable of differentiating into both endothelial cells and smooth muscle cells that are motile and proliferative. Our model yielded patterns that were qualitatively and quantitatively consistent with our experimental observations, for physiologically reasonable parameters. Our results suggest that, for such parameter values, it is the post-differentiation motility and proliferation rates that drive the formation of vascular patterns more than differentiation alone. This was shown to be true even when higher order effects like density dependent adhesions and paracrine signaling were considered. Secondly, microfluidic devices and organ-on-a-chip models have become good solutions for studying 3D cell cultures that more closely mimic physiologically relevant lengths and timescales. These devices allow for the incorporation of height into cultures by suspending cells in extracellular matrices, such as fibrin, that more closely mimic *in vivo* microenvironments. Here I also report the use of endothelial cells in culture with mural cells, smooth muscle cells and pericyte cell cultures, as ideal conditions for the successful development of perfusable vasculature within a three-channel microfluidic device. We found the use of these cells, in tri-culture, to lead to the development of physiologically narrow vessels that were functional and perfusable for more than two months. These findings hint at methods that could be employed for directing specific micropatterns or 3D structures that focus on controlling the motility and proliferation rates of differentiating stem cells. Furthermore, these studies aim to advance the field of organoid development, by providing a reliable method for developing fully vascularized organoids and organs that are stable for long time-scales.

TABLE OF CONTENTS

LIST OF FIGURES

LIST OF TABLES

APPENDIX

TABLES

FIGURES

VIDEOS

Chapter 1: Background

1.1 Introduction

The *in vivo* cellular microenvironment is a complex system made up of multiple cell types, cell-to-cell signaling interactions, varying extracellular matrix (ECM) components, and a plethora of soluble signals. All of which coexist within a small region of space termed the cell *niche*. One example is the stem cell niche, which uniquely contains all required components for maintaining and preserving the stem cell's self-renewal properties(1). This self-renewal and differentiation potential is what makes stem cells an exciting, but also a challenging topic of research. By understanding and exploiting the stem cell fate determination mechanisms we should be able to effectively generate endless amounts of specialized/mature cells and use them to aid in healing/replacing damaged tissues and/or organs(2). However, the collection and growth of these stem cells, for autologous treatment, can be difficult since large cell quantities are required from patients, and in some cases impractical such as those from aged or diseased individuals. Fortunately, the discovery of embryonic stem cells (ESC)(3) and induced pluripotent stem cells (iPSCs)(4) have emerged as great solution for producing, seemingly, limitless amounts of functional cells. A critical step in achieving this goal includes understanding and controlling the process by which designed multicellular tissues/organs are fed through either preexisting or newly generated vasculature. If successful, this could reduce, if not eliminate, the need for an organ transplant waiting lists.

Historically, *in vitro* research has mostly looked at cell cultures under a 2D lens, however this method of studying the emergence of complex *in vivo* structures, such as blood vessels, is ineffective. This is due to the characteristic 3D structures necessary for proper function, mainly their tube formation, known as its lumen, which is a fully 3D structure composed of multiple spatially orientated cells(5). Additionally, while traditional *in vitro* culture techniques have mostly focused on the use of biochemical signals as a way of guiding cell behaviors, including stem cell differentiation, our growing understanding on the impact that mechanical cues have on cell behavior has led to an embrace in the use of mechanical stimuli as a means for guiding specific cell behaviors, including migration, proliferation, apoptosis, and even stem cell differentiation. This is accomplished by the use of mechanically tunable two-dimensional (2D) hydrogels(6–11) and tunable three-dimensional (3D) collagen and fibrin hydrogels(12,13). These 3D lab-on-a-chip technologies are facilitated by microfluidic devices, which are micrometer to millimeter sized 3D housing units that allow height to play a role in cellular culture, providing researchers with the ability to more closely mimics the *in vivo* microenvironment. Furthermore, microfluidic devices have been shown to be ideally suited for studying complex cellular behavior such as vascular emergence(14) and tumor metastasis(15).

1.1.1 Stem Cells

Stem cells (SC) are defined as unspecialized cells that can differentiate, or turn, into other types of cells found within the body. Their unique self-renewal property and ability to differentiate into more specialized cells makes them an interesting, although difficult, field of study. The exact type of stem cell phenotype is determined by their differentiation potential, with totipotent stem cells (TSC) being the purest form. These TSCs arise in early zygote development, and have the ability to differentiate into all three germ linages (mesoderm, endoderm, and ectoderm) as well as placental tissue(16,17). Whereas pluripotent stem cells (PSC), similarly, have the potential to differentiate into a wide variety of cell types found within each of the three germ linages but have lost the capability to develop into placental tissues. Pluripotent stem cells can be acquired by harvesting the inner cell mass of a developing blastocyst(18), reprograming adult somatic cells(19), or via direct conversion (dedifferentiating) of unipotent stem cells(20). Furthermore, two main classes of specialized stem cells exist, appropriately named multipotent and unipotent stem cells. These stem cells are characterized by their ability to differentiate into *many* or *single* downstream cell types found within certain linages(21,22). These stem cells can be found throughout a mature organism's body and serve as a critical component in regulating homeostasis and wound healing.

1.1.2 Emergence of Vascular Cell Linages from Stem Cells:

During vertebrate development the emergence of the circulatory system precedes other organ systems(23). This is because of the need for efficient and continuous nutrient and oxygen delivery to the growing and differentiating tissues. Furthermore, it is endothelial cells (EC) that are an integral part in the formation of these vascular structures by lining the luminal side of vessels. These functional ECs emerge from EC progenitor cells, known as angioblasts, which in turn emerge from the mesoderm soon after gastrulation(24). Three key signaling molecules regulate the stem cell to mesoderm and EC precursor commitment: fibroblast growth factor 2 (FGF2), bone morphogenic protein 4 (BMP4) and Indian hedgehog (IHH), reviewed here(23). These early-stage EC populations coalesce to form the primary vascular plexus, in a process known as vasculogenesis. Subsequently, these ECs proliferate and coalesce into *cords*/*chains* of single ECs eventually, leading to tube formation(25). After the primary plexus is established, there is further specialization of the ECs leading to arterial, veinous, and lymphatic EC specialization, (reviewed in (23)).

Given the important role that ECs play in vascular development, some have postulated the use of these ECs for transplantation as a means of therapeutic vasculogenesis and treatment of ischemic tissues(26). However, the collection and growth of ECs for an autologous treatment is often difficult since large quantities of viable ECs are required from patients, and in some cases impractical, such is the case for aged and/or diseased individuals. Fortunately, the discovery of embryonic stem cells (ESC)(3) and induced pluripotent stem cells (iPSCs)(4) have emerged as great solution for producing, seemingly, limitless amounts of functional cells, including ECs.

ECs have successfully been derived from 3D embryoid bodies(26), a technique where ESCs are cultured as suspended aggregates and allowed to naturally differentiate(27,28). While not ideal, since EBs generate all cell across all germ linages, and of which ECs only account for <3%, it is necessary to further isolated/sort these low EC populations and further culture them to increase their cell density. In these early reports key marker expressions of platelet endothelial cell adhesion molecule 1 (PECAM1/CD31), vascular endothelial cadherin (VE-Cad), and the absence of GATA-binding factor 2 (GATA-2) were used to identify the EC phenotype. Later it was found that a population of vascular progenitor cell (VPC) derived from CD34+ EB derived mesoderm cells would serve as an intermediary between the mesoderm and vascular cell linages, such as ECs and mural cells(29). Here it was shown that ECs and SMCs could be generated via a three-step differentiation protocol: 1) culturing of EBs for 10 days, 2) isolation of CD34+ cells via immunomagnetic beads, and 3) subsequent culturing of CD34+ cells on gelatin-coated dishes with vascular cell linage control being achieved by the exogenous addition of either vascular endothelial growth factor (VEGF), for EC differentiation, or platelet derived growth factor beta ($PDGF_{\beta\beta}$), for vascular smooth muscle cell differentiation(30,31).

Simpler 2D platforms also exist that can induce EC and hematopoietic cell differentiation by relying on cocultures of stem cells seeded on sacrificial stromal or embryonic fibroblast cell monolayers. It has been shown that induced ECs and hematopoietic cells share a common progenitor cell; intimately linking the emergence of both cells and leading to an overlap in their marker expression, the most common of which is CD34(32). Furthermore, in both mouse and human ESCs, it has been shown that the emergence of CD34+ cells can be upregulated when coculturing stem cells with bone marrow stromal cells, leading to an effective method for both EC and hematopoietic differentiation via the upregulation of CD34+ cells(33,34). Here, human ESCs (hESCs) were specifically cocultured with macrophage colony-stimulating factor deficient stromal cell, OP9, monolayers leading to early, by as much as a week, hematopoietic differentiation compared to the EB method. Furthermore, it was shown that this method would yield up to 20% of CD34+ cells that expressed high hematopoietic potential, as seen in their higher expression levels of SCL, GATA-1, GATA-2, Flk-1, and CD45. Additionally, hidden within these CD34+ cells were CD31+, a known EC marker, cells that accounted for as much as 17% of the CD34+ population by day 9(34). Similar results have been achieved with cocultures of hESC and mouse embryonic fibroblasts (MEFs)(32). It was later shown that isolation and continued culturing of CD34+ cells under endothelial cell growth mediums, that included VEGF and FGF2, would lead to an increased expression of adherent EC markers, such as PECAM1/CD31 and VE-Cadherin(35).

Recently, the use of chemically defined mediums has showed that ECs can be derived without the use of a sacrificial monolayer nor serum based mediums(36,37). For example, the McCloskey lab uses a two-step differentiation protocol that focuses on 1)

differentiating stem cell into VPC, that are positive for VEGF receptor 2 (VEGFR2), known as KDR in humans and Flk-1 in mouse, instead of CD34, and 2) isolation of KDR/Flk-1 positive cells for further differentiation into ECs by culturing in EC specialized medium containing VEGF and bFGF(37–39). The use of VEGFR2+, a tyrosine kinase receptor, cells in tandem with or instead of CD34+ cells for VPC identification, while not new(40–42), has been shown to lead to greater specification of ECs phenotype(43). This is because differentiating stem cells that are CD34+ also express VEGFR2, these VEGFR2+ cells when isolated, have higher ECs differentiation potential when coupled with exogenous VEGF supplement. In this respect, VEGFR2+ cells have been shown to be highly sensitive to VEGF, its binding ligand, and critical in network and lumen formation(44). Most recently combinations of both chemically defined mediums and mechanical cues (in the form of substrate stiffness) has led to similar EC inductions results(45). These studies highlight the highly complex microenvironment that must be matched *in vitro* to develop highly specific cell linages of ECs.

1.1.3 Substrate Stiffness-Mediated Cellular Responses

Recall that within the *in vivo* microenvironment, cells are not only interacting with other cells, but also with their surrounding extracellular matrix (ECM). The physical proprieties, also known as mechanical properties, of this surrounding material has been shown to play a crucial role in cellular function and behavior. By *sensing* these mechanical properties, in the form of mechanical cues, cells can adapt and regulate their behavior to actively promote and/or maintain homeostasis(46). This process by which cells sense and respond to the mechanical cues in their microenvironment, is known as mechanotransduction, and it describes the methods by which cells *sense* their local microenvironment's mechanical properties and turn them into biological signals. This conversion of mechanical stimuli into biological signals enable cells to coordinate an appropriate responds to its changing microenvironment, by promoting cell adhesion, migration, proliferation, apoptosis, and/or differentiating(47–50). Cells have various mechanisms by which they can *senses* and respond to these mechanical cues, including cell-to-cell mediated adhesions, usually driven by cadherins(51), integrins(52), selectins(53), claudins(54), and connexins(55), or via cell-matrix adhesions, such as ECM bound integrins(52,56,57).

Integrins, the most common type of mechanosensors, are type I transmembrane proteins that line the cell's membrane and mostly aid in cell-ECM adhesions but can also function as a cell-cell adhesion by directly binding to surface receptor, such as CD31. They are found as heterodimers composed of two subunits, α and β, and can form up to 24 different functional α-β combinations(58). While different combinations of these subunits enable the binding of different ECM proteins, there can be redundancy and overlap in these combinations. For example, $\alpha IIb\beta 3$, $\alpha V\beta 3$, $\alpha V\beta 6$, $\alpha V\beta 1$, $\alpha 5\beta 1$, and $\alpha 8\beta 1$ heterodimer combinations are all able to bind the Arginine-Glycine-Aspartic acid (RGD) amino acid sequence (motif) of fibronectin, while fibrinogen can only be bound by

two of these RGD binding integrins, αIIbβ3 and αVβ3. Additionally, fibrinogen can be bound by non-RGD binding integrins, such as αMβ2 and αXβ2 which bind to the leucine-aspartic acid-valine (LDV) motif(58). Lastly, integrins are also able to bind surface receptors, such as CD31 which is expressed on the luminal side of blood vessels and can be bound by the αVβ3 integrin aiding in the transendothelial recruitment of leukocytes(59). This diversity in function facilitates the communication between cells and their surrounding microenvironment.

Mechanistically, once the integrin is bound there is a recruitment of focal adhesion proteins and cytoskeletal elements that coalesce to stabilize the cytosolic c-terminus of the adhesion. Here matrix stiffness has been shown to play an important role in increasing the degree of stability and f-actin recruitment, with high stiffness leading to higher stability and a greater assembly of actin stress fibers further leading to an increase in cell spread(60). Moreover, it has been shown that focal adhesions and f-actin recruitment are both Rho mediated, with increased Rho activity promoted by stiffer substrates and an attenuation of these results achieved upon RhoA inhibition by the pharmacological agent Y27632(60). The Rho family is responsible for initiating many downstream signaling cascades; one important one is the upregulation of Rho-associated kinase (ROCK). ROCK activation is important for its activation of myosin II, which when coupled with actin polymerization generating cellular forces that change the cell's shape and induces deformations equal in force to their surrounding microenvironment(46,50). It is understood that these changes are responsible for many of the cell's stiffness responses. In short, this interplay creates a feedback loop where the formation of focal contacts leads to the formation of actin stress fibers, which, in turn, regulates Rho concentrations. Furthermore, it has been shown that ROCK can also be activated by matrix stiffness alone via integrin stimulation(50). Alternatively, cadherins, another mechanosensor, transduces mechanical signals via the formation of both focal adhesion complexes and focal contacts in response to mechanical stimuli(51). In both cases, the formation of focal adhesion stimulates internal signaling proteins leading to changes in gene expression, cell morphology, migration, and/or survival and proliferation(46,49).

Another well-known mechanotransduction pathway, is the Hippo-YAP signaling network, specifically the non-canonical Hippo signaling pathway where Yes-associated proteins (YAP) and transcriptional coactivator with PDZ-binding motif (TAZ) are translocated into the nucleus under high stiffness substrates to initiate cell proliferation. YAP/TAZ has been implicated for their role in promoting homeostasis, tissue growth, organ size regulation, and cancer development(61–63) whereby the increased presence of actin, upregulated under high stiffness substrates, binds to AMOT, a known sequester of YAP, freeing YAP and allowing the YAP/TAZ complex to enter the nucleus. Once inside they bind to transcription factors such as TEAD to drive up cell proliferation(61).

1.1.4 Substrate Stiffness-Mediated Stem Cell Differentiation:

Stem cells (SCs) can similarly *sense* their microenvironment's mechanical properties and respond by not only proliferating and migrating, but also by differentiating(7,64). Engler et. al, was the first to robustly study this differentiation potential by culturing human mesenchymal stem cell (hMSCs) on poly(acrylamide) (PAA) hydrogels of various elastic properties. Their properties were consistent with *in vivo* microenvironment stiffnesses, as measured by the materials Young's Modulus (E), and encompassed specific stiffnesses such as brain (0.1 – 1 kPa), muscle (8 – 17 kPa), and bone (25 – 40 kPa)(7,8,65). They found that hMSC would preferentially differentiate into cell types that shared a similar *in vivo* elastic environment. Here, for the first time, it was shown that cultures of hMSCs would differentiate into neurons, myoblast, and osteoblast solely based on substrate stiffness, despite identical serum conditions.

Further studies of substrate driven SCs differentiation via integrin-ECM binding, reviled the mechanism by which SCs are able to sense their microenvironment. This is first initiated by integrin-ECM binding which starts the formation of the focal adhesion complex, in the presence of Rho, leading to morphological changes. These primary morphological changes, driven by actin production and remodeling, were later shown to be sufficient in predicting the differentiation potential of hMSCs. Here, it has was shown that hMSC could effectively be guided towards an adipogenic fate, under soft/compliant (0.7 kPa) substrates, or osteogenic fate, under stiffener substrates(56,66,67). Furthermore, researchers later shown that compliant substrates made from PDMS, with a Young's Modulus (E) of 5 kPa, could drive neuronal fate decisions in hPSC by inhibiting SMAD phosphorylation, a transcription factor, and activation of LATS, an actin binding protein. Taken together, this leads to the phosphorylation of YAP, sequestering it in the cytosol where it further inhibits the nuclear translocation of SMAD proteins(66,68). This inhibition of SMAD proteins, either through endogenous or exogenous means, alongside the use of compliant/soft substrates proved to be an effective method for generating high yields of $Pax6^{+}$, a neuroectodermal differentiation maker, neural-like cells from hPSCs.

In a study by Smith et. al.(69), they showed that mesoderm and EC differentiation could be enhanced by culturing/differentiating hiPSCs on compliant PDMS substrates with a Young's Modulus (E) of ~ 3 kPa compared to those differentiated on E ~ 1.7 MPa or E ~ 3 GPa. Interestingly, they observed that YAP played an important role and would localize in the nucleus in a stiffness-dependent manor, with higher stiffnesses leading to higher YAP nuclear localization and vice-versa. Conversely, it was observed that under the absence of WNT signaling, YAP would instead be cytoplasmically localized and aid in the destruction of β-catenin, effectively inhibiting mesoderm differentiation. Under WNT activation, YAP and β-catenin both become transcriptionally active leading to a mechanically induced response that drove mesodermal differentiation and EC commitment without the need for sorting or additional purity steps. It was reported that up to 75% VE-Cad+ cells could be generated under this differentiation protocol(69).

Furthermore, hMSCs are able to discriminate between relative low stiffnesses of 3kPa and 8kPa when differentiating into vascular cells, specifically endothelial cells (ECs) and smooth muscle cells (SMCs)(9,45). Despite the developmental commonality in the vascular co-emergence of EC and SMC, it is impressive that slight differences in substrate stiffness could lead to such differential fate commitment(9,70,71), and further highlights the need for the incorporation of stiffness controlled matrix/substrate architectures in tissue cultures.

1.1.5 Modeling Stem Cell Differentiation, Cell Behavior, and Micropatterning:

Computational models are often used as a means of revealing unmeasurable or obscure cellular mechanisms that are experimentally unfeasible or grossly expensive. While there exists many types of models that have explored cell differentiation(72,73), motility(74), proliferation(75), and combinations of these parameters(76–82), none of them have really looked at the interplay between all of these variables. Additionally, models that explore vessel formation tend to focus on branching(83) rather than the interplay between cells, biochemical gradients, and matrix remodeling. Similarly, models that explore stem cell differentiation tend to focus on pathway specifics and use Boolean logic as a way of understanding the biochemical changes happening within individual cells(84). However, Boolean logic alone cannot take into consideration mechanical signaling nor the processes that cells undergo as they attach, migrate, and proliferate on a substrate with a defined stiffness. Additionally, no model so far has been able to take into consideration the dynamic interplay between the cellular forces that deform the substrate and lead to the formation of a new localized stiffness.

There is hope that with computational power increasing steadily, researchers will now be able to run simulations of fantastically complex behaviors. For example, recently a multi-scale model was developed to study the role of internal cellular pressure/tension on cell division(85). Another model used a multi-scale finite element model to explore how neurulation happens in amphibians(86). Their 3D model, composed of individual cells, calculates the intracellular forces individual cells produced, the resulting tissue dynamics, and resulting tissue motion as it leads to the formation/development of the neural plate in amphibians. An area of research that has not been explored is the emergence of micropattern formation from differentiating stem cells. Micropatterning as a whole has been explored in depth, but not in stem cell differentiation. In a recent article by Osborne et. al, five modeling frameworks were compared in their effectiveness in simulating the self-organization of multicellular tissues(87). Their results showed the strengths and weaknesses of on-lattice and off-lattice modeling, as well as model effectiveness in accounting for cell adhesion, proliferation, and short or long range signaling. Depending on the specific question at hand, some models exhibit distinct advantages. For example, vertex models are excellent for exploring adhesion, proliferation, cellular forces, and cellular geometries, however they become computationally expensive with more agents(87). Likewise, finite element models (FIE) have been used in modeling

environments where cell geometries and cellular forces are important(88,89). Examples like these highlight the growing interest in understanding the interplay between cells and their surrounding microenvironment.

1.1.6 Organ-on-a-Chip Technologies:

Cells-on-a-chip technologies, which spatially segregate specialized cells within different compartments of a polydimethylsiloxane (PDMS) device, have emerged as promising methods for studying and directing cell assembly and communication across distances. Furthermore, these devices have become a promising methods for exploring the effects that new drugs have on targeted cell types as well as any potential downstream effects on different cell types, and has aided in drug discovery by closely mimicking whole organ systems; further offering an increasingly holistic view of a drug's potential side effects(90). However, these applications lack the ability to fully recapitulate the whole cellular microenvironment by often forgoing complex mechanical and spatial-temporal signals (reviewed in (91)). In contrast, organ-on-a-chip technologies, which enable the development of microengineered tissues, have become great solutions for the study of 3D tissues, and have shown promise in recapitulating key functional properties of human organs. These technologies are frequently facilitated by the use of PDMS microfluidic devices where cultures of cells are suspended within 3D hydrogels that closely mimic the physiologically relevant properties, lengths, and time-scales of tissues/organs(92). They have also gained popularity within the pharmaceutical industry where whole organ systems can be readily developed for the targeted testing of new drugs, offering higher predictive potential for *in vivo* studies(90,93). Human organs such as bone(94), brain(95), heart(96), intestine(97), liver(98), lung(99), and kidney(100) have all been explored with various levels of success. Non-surprisingly greater levels of success were consistently observed when environmental conditions more closely matched the physiological microenvironment's properties, such as matching ECM composition, paracrine signaling, and mechanical stimuli.

The use of microfluid devices, specifically, allow for the incorporation of height into cell and tissue cultures by suspending cells within a 3D ECM(101) like collagen(102), Matrigel(103), fibrin(14), and alginate(104) as well as the use of biocompatible synthetic polymers that do not induce cytotoxic affects, such polymers include poly(lactide-co-glycolide) (PLG)(105) and poly(ethylene) glycol (PEG)(106). In a study by Arslan et. al they showed that 3D vascularized cardiac tissues could be engineering within a PDMS microfluidic device(107) by coculturing hiPSC-ECs with human brain vascular pericytes (HBV-PCs) within a fibrin matrix that would then self-organize into perfusable vascular networks that would colocalize/surround embedded cardiac sphere. Here, it was shown that cardiac beating was also associated with an enhancement in vessel density and improved lumen formation. Specifically, batch-to-batch differences would often lead to under vascularized tissues, but these could be reversed by NOS driven cardiac beating, suggesting that mechanical inputs may be necessary for the full recapitulation of vessel formation. In a different study, Chen et. al developed a microfluidic circulatory device that

could mimic the four-chambered heart(108). While no cardiac cells were used, their PDMS microfluidic design proved to be great at simulating internal cardiac pressers and flow rates. They further showed that by adjust their microfluidics' internal chamber's pressure and flow rates, so that it closely matching *in vivo* conditions, would lead to morphological changes and changes in receptor expression from their human umbilical vein endothelial cell (HUVEC) monolayers. This recapitulation of the blood vessel's endothelium microenvironment resulted in changes on the EC alignment and an increased in the expression of ZO-1, an EC marker. Furthermore, it was shown that this device was ideal for studying a ECs response to physiologically relevant shear stress and showed promise in drug screening and disease modeling.

1.1.7 Vessel Formation in Microfluidic Devices:

There are now many labs that utilize microfluidic devices as a means to study and recapitulate native vessel emergence, known as vasculogenesis(15,109,110), and/or new EC sprouting vessels, by a process known as angiogenesis(111). These studies have led to a growing understanding of the complex cellular mechanisms that facilitate vessel emergence and have been shown to have greater advantages in studying complex behaviors which have been previously limited to 2D Matrigel platforms(105). In some studies, researchers have utilized microfluidic platforms to further explore unique vascular systems by seeding ECs, such as human umbilical vein endothelial cell (HUVEC), colony forming ECs(112), and iPSC-ECs(113), with various supplementary cell types, such as normal human lung fibroblasts (NHLFs)(114,115), pericytes (PCs)(107), mesenchymal stem cells (MSCs)(116,117), astrocytes(113), etc. For example, Chen et. al. (15) created microvascular networks from HUVECs and PCs which were allowed to self-assemble over 5 days prior to the addition of MDA-MB-231 breast cancer cells. Their system was then used to study the interactions between tumor cells and the endothelium to further study cancer cell metastasis. In another study by Campisi et. al., they showed that a functional blood brain barrier (BBB) could be recapitulated within a microfluidic device from seeded hiPSC-EC, PCs, and astrocytes (ACs) within a fibrin matrix(113). They observed that full self-assembly of their microvascular networks could be achieved within 7 days, and that these vascular networks were both functionally and morphologically similar to human BBB with low network permeability and high transport selectivity. Lastly, despite only being seeded within a fibrin matrix the resulting vascular networks were shown to be surrounded by a basement membrane, at day 7, consisting of high levels of laminin and collagen IV compared to networks composed from cultures missing pericytes, astrocytes, or both.

In a study by Whisler et. al., the impact of exogenous VEGF, fibrin concentration, and seeding densities, on the development of 3D perfusable microvasculature(14), was examined. Their PDMS microfluidic device consisting of HUVECs with or without normal human lung fibroblasts (NHLFs), was found to be ideal for the development of perfusable network that were stable for up to 10 days. Furthermore, they found that by increasing VEGF and fibrin concentrations, independently, would lead to an increase in network

branching while simultaneously decreasing the overall vessel's diameter. Interestingly, upon increasing the seeding density, there was no observable impact on network branching but rather an increase in the overall vessel diameter(14). Examples like these show the depth and potential that microfluidic platforms have to advance our understanding in the formation and regulation of the vascular system.

1.1.8 Goals and Objectives

In this dissertation, I studied the differentiation of mouse embryonic stem cells (mESCs) into clusters of vascular cells composed of endothelial (ECs) and smooth muscle cells (SMCs) and vascular assembly within microfluidic devices. I explored the vascular fate commitment of these mESCs as a model system to develop a population based in-lattice computational model that explores the emergence of unique 2D vascular patterns (**Chapter 2**). I then used poly(acrylamide) (PAA) hydrogels to explore the impact that substrate stiffness and cellular density has on the emergence of cord-linked primitive 2D vascular networks (**Chapter 3**). Lastly, I used a three-channel microfluidic device to seed cultures of vascular cells within a fibrin matrix to study the emergence of perfusable 3D vascular networks, under fixed biochemical and mechanical stimuli (**Chapter 4**).

Chapter 2: Motility and Proliferation Drive the Emergence of Patterns in Co-cultures of Differentiating Vascular Progenitor Cells

Abstract

Developing vascular cells have been shown to self-organize into unique structures in both two and three dimensions. Depending on the conditions, these cells may develop into perfusable vessels in 3D, or develop micropatterns with spatial segregation of different cell types in 2D. The self-organization arises from an interplay of motility, proliferation, differentiation, and signaling with the relative importance of these factors remaining unclear. The objective of this study was to develop and use a computational model to explore how these different factors affect the emergence of micropatterning from developing vascular cells in a 2D *in silico* environment. We developed a stochastic on-lattice population-based model to study this emergence from a starting distribution of stem cell progenitor cells capable of differentiating into both endothelial cells and smooth muscle cells that are motile and proliferative. Our model yielded patterns that were qualitatively and quantitatively consistent with our experimental observations, for physiologically reasonable parameter values. Our results suggest that, for such parameter values, it is the post differentiation motility and proliferation rates that drive the formation of vascular patterns more than differentiation alone. This was shown to be true even when higher order effects like density dependent adhesions and paracrine signaling were considered. These findings hint at methods that can be employed for directing specific micropatterns or 3D structures that focus on controlling the motility and proliferation rates of differentiating stem cells.

2.1. Introduction

A major obstacle in the development of tissue engineered products for clinical applications is the challenge of generating perfusable vasculature throughout the engineered tissue. While some approaches have relied on the generation of perfusable vasculature by providing the ECM components from specific organ structures, such as using decellularized organs(118), others focus on engineering vasculature from the top-down by seeding mature cells within a 3D hydrogel and allowing for the natural self-assembly of the complex tissues within microfluidic housing devices(14). However, a third, more promising, approach utilizes stem cells for directed differentiation and autologous treatment. In this approach, the aim is to direct the differentiation of endothelial cells (ECs)(26,119) and smooth muscle cells (SMCs)(120–122) through a combination of growth factors, specialized mediums, mechanical signaling, etc. (123). In this approach, undifferentiated cells known as stem cells, could be harvested, and used for the autologous development of vascular networks arising from co-cultures of ECs and SMCs. Moreover, the differentiation of vascular cells, including ECs and SMCs, have been shown to self-organize into unique structures in both two and three dimensions. Depending on the conditions, these cells may develop into perfusable vessels in 3D, or develop micropatterns with spatial segregation of different cell types in 2D.

The McCloskey laboratory has developed chemically-defined differentiation protocols that have been proven to be highly effective in deriving mouse embryonic stem cells (ESCs) and human ESCs (37,38,124) into vascular progenitor cells (VPC), as well as purified ECs and SMCs (**Fig. 1A**). While obtaining purified differentiated cells, of different types that make up the vasculature, is an important first step, the ultimate goal would be to direct the simultaneous emergence of vascular structures from differentiating cells as is observed during normal development. Indeed, upon closer inspection of some of the 2D VPC outgrowths we observed that the cells would, when conditions favored a balanced EC and SMC differentiation and proliferation rate, self-organize into micropatterns (**Fig. 1B**) with EC clusters loosely surrounded by SMCs, indicating a recapitulation of normal vascular development in 2D. However, directing the patterning to produce perfusable networks in 3D requires an understanding and control of the interplay of various processes involved in cell self-organization which include motility, proliferation, differentiation, and signaling. While the details of such strategies would be highly system-dependent given the complexity and inter-connectedness of the processes, and thereby challenging to uncover, the answers to even basic questions concerning the relative importance of processes in regulating patterning are elusive. For example, it is not clear whether directed differentiation alone can lead to vascular patterning or whether motility is a necessary ingredient or whether it is the motility and proliferation of post-differentiated cells that is the dominant process leading to morphogenesis (**Fig. 1C**). Here, we attempt to shed some light on such questions over a physiologically relevant range of

parameters governing these processes, using a computational model motivated and calibrated by our experimental cultures of mouse ESCs.

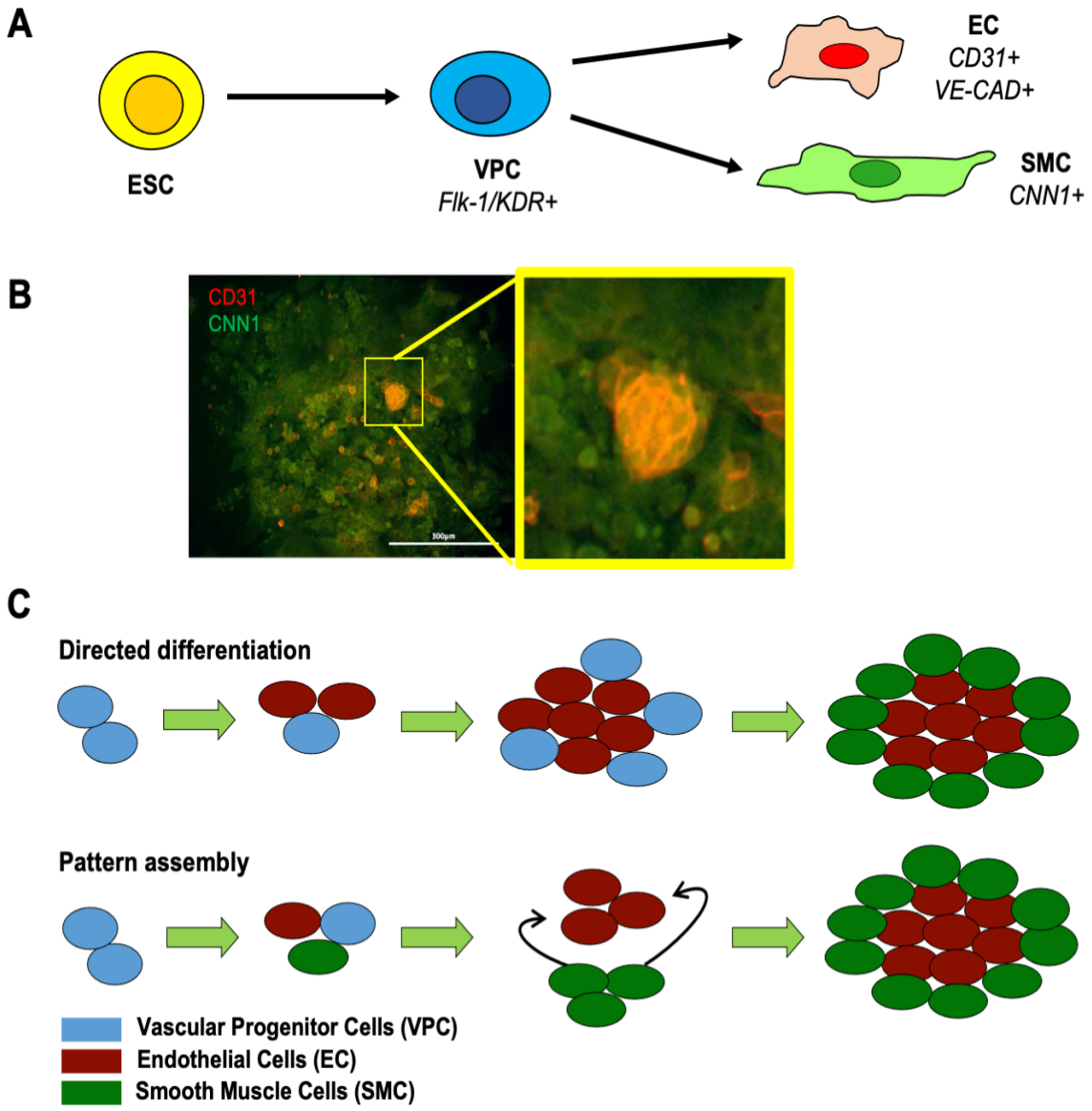

Figure 1. Experimental observations

A) Schematic of the differentiation process. Briefly, ESCs are differentiated into VPCs via stage specific induction medium. VPCs are then further differentiated into co-cultures of ECs and SMCs via stage 2 specific induction medium. **B)** Immunofluorescent images of VPC outgrowths, at day 4 post-secondary induction, stained here are CD31+ (red) cells indicating EC fate commitment, while CNN1+ cells (green) indicate SMC fate. Magnified is an EC cluster (red) surrounded by SMCs (green). Scale bar is 300μm. **C)** Schematic of possible mechanisms explaining emergence of micropatterns, either through directed differentiation where differentiation is spatially varying or via pattern assembly where post differentiation mechanisms, specifically motility and proliferation, are driving pattern formation.

Several computational models exist for simulating the self-organization of multicellular tissues(87), including on-lattice and off-lattice models that account for cell adhesion, proliferation, and short or long range signaling. Depending on the specific question at hand, some models exhibit distinct advantages. For example, vertex models are excellent for exploring adhesion, proliferation, cellular forces, and cellular geometries, however they become computationally expensive with more cells(87). Likewise, finite element models (FIE) have been used in modeling environments where cell geometries and cellular forces are important(88,89). Many other models have explored cell differentiation(72,73), motility(125), proliferation(75), and combinations of these parameters(76–82). Here, we chose an on-lattice, stochastic, population-based model that uses ordinary differential equations (ODE) to represent the spatial-temporal dynamics of cell densities (# of cells per lattice sites) evolving through cell proliferation, migration, death, differentiation, and cell-to-cell signaling. Such an approach allows us to effectively parametrize all the important processes, based on experimental observations and literature values, while also allowing us to monitor spatial structuring of the cellular population over time. Since it is a coarse-grained approach, it also allows us to avoid trying to replicate dynamics at the single cell level, about which less is known, and thereby also increases computational efficiency in simulating large cell numbers (10^4-10^5).

We simulated the time evolution of the system for a wide range of physiologically plausible parameters and focused on the fractions and spatial distributions of emerging vascular cell (EC or SMC). By analyzing our simulations within physiologically relevant domains we were able to calibrate our model with experimental data and thereby extract practical information from parameter sweeps. The results suggest that the vascular-like spatial pattern (defined as EC clusters surrounded by SMCs) emerges when the fraction of differentiated ECs lies within a “zone of co-emergence” with well-balanced numbers of both cell types. Moreover, for physiologically relevant ranges of proliferation and migration, the distribution of simulated EC cluster diameters was consistent with experimental observations. For the parameter ranges relevant to our system, we found that the spatial distributions of different cells are more sensitive to differences in proliferation and migration rates between cell types compared with differences in intrinsic or induced differentiation rates. Consequently, it is the proliferation and migration rates that appear to be most responsible for the establishment of the observed micropatterns within our differentiating co-cultures. These results support the current self-assembly vasculogenesis observed in mature post-differentiation cell co-cultures when seeded withing hydrogels(112,126,127) and may aid the rational design of co-developing vasculature within 3D tissues.

2.2. Methods

2.2.1. Embryonic Stem Cell Culture

The mouse embryonic stem cell (mESC) lines used for these studies included mESC-R1 (ATCC) and. The mESC-R1 were cultured on 0.5% gelatin in serum-free medium containing

Knockout Dulbecco's Modified Eagle Medium (KO-DMEM; Invitrogen), 15% Knockout Serum Replacer (KSR; Invitrogen), 1X Penicillin-Streptomycin (Invitrogen), 1X Nonessential Amino Acids (Invitrogen), 2mM L-glutamine (Invitrogen), 0.1mM 2-mercaptoethanol (Calbiochem), 2000 Units/ml of leukemia inhibitory factor (LIF-ESGRO; Chemicon), and 10 ng/ml of bone morphogenetic protein-4 (BMP-4; R&D Systems). Full media changes occurred every other day and cells were passaged every four to five days.

2.2.2. Embryonic Stem Cell Differentiation

R1-mESC (ATCC) were differentiated into EC and SMC using our laboratories two staged serum-free induction protocols(37). The mESC were induced on 50µg/mL fibronectin (Corning) coated plates (BD Biosciences) under our stage 1 induction medium containing alpha-MEM (Cellgro), 20% knockout serum replacement (ThermoFisher), 1X penicillin-streptomycin (ThermoFisher), 1X nonessential amino acids (ThermoFisher), 2mM L-glutamine (ThermoFisher), 0.05mM 2-mercaptoethanol (Calbiochem), 5 ng/mL BMP-4 (Peprotech), and 30 ng/mL of VEGF (Peprotech). After 2 days, Flk-1+ (Biolegend) vascular progenitor cells (VPCs) were purified (BD FACS Aria III) and replated on 50µg/mL fibronectin for an additional 4 days under stage 2 specific differentiation medium consisting of 70% alpha-MEM (Mediatech), 30% DMEM (Invitrogen), 2X Nutridoma CS (Roche), 1X penicillin-streptomycin (Invitrogen), 1X nonessential amino acids (Invitrogen), 2mM L-glutamine (Invitrogen), 0.05mM 2-mercaptoethanol (Calbiochem), and supplemented with 50 ng/mL of basic fibroblast growth factor (bFGF) as previously optimized for R1-mESC induction into ECs (37).

2.2.3. Immunofluorescent Staining

Visualization of the cell micropatterning was conducted by immunofluorescent staining of VPCs outgrowths on day 4 post purification (**Fig. 2B**). Briefly, cells were fixed with 4% paraformaldehyde (Tousimis) and permeabilized with 0.7% Triton X-100 (MP Biomedicals). Nonspecific binding was prevented using 1% bovine serum albumin (Sigma). Conjugated CD31 PE, EC stain (BD Biosciences) and primary antibody CNN1 (SMC stain, Sigma) were added and allowed to stain overnight at 4˚C. Cells were rinsed before addition of secondary antibody, Alexa Fluor 488 (Thermofisher), and DAPI. Cells were incubated for an additional hour before final rinse and imaging via fluorescence microscopy (Nikon TE2000-E). For phalloidin stains (cytoskeletal stain), a conjugated antibody was used (Invitrogen).

2.2.4. EC Cluster Diameter Distribution

The diameters of EC clusters were calculated by a custom MATLAB script. Briefly, imported images, DAPI stained and simulated, were smoothed via *medfilt2* function, and then turned into binary (*imbinarize*) images via Otsu (*graythresh*) thresholding. An outline of the clusters was then reconstructed via subtraction of the *dilated* and *eroded* binary images. The *regionprops* function was then used to record the *Filled Area* of the clusters

(**Appendix Fig. S1**). Comparison between experimental and simulated clusters, was done by calculating an effective cluster diameter, D=2*(*Filled Area* /π)$^{0.5}$, for both conditions.

2.2.5. Modeling Stem Cell Dynamics

Our computational model considers the spatial and temporal distributions of three different cell types within a simulated square lattice. We denote by X_A, X_B, and X_C the normalized cell density (e.g. $X_A = N_A/N_{max}$, where N_A is the number of *A* cells and N_{max} is the maximum number of cells allowed at each lattice site leading to an interval between [0, 1]) of VPCs, ECs and SMCs, respectively. Their dynamics are governed by the cell's migration, their rates of proliferation, differentiation, and cell death (**Fig. 2A-C**). In our model, each cell can migrate between neighboring lattice sites at a preset migration value, J_θ (here θ represents either A, B or C corresponding to cell identities of VPC, EC, and SMC, accordingly). Each cell type can also proliferate (double), and die at a specific rate, δ_θ and μ_θ, respectively. Additionally, VPCs can differentiate into either ECs or SMCs at rates of α_B and α_C, respectively. The cellular dynamics are then a combination of a cell's migration, these rates, and stochastic noise, S_θ, leading to a set of three ordinary differential equations (ODEs), equations (1-3), one for each of the three changing cell populations (X_A, X_B, and X_C).

$$\dot{X_A} = (\delta_A + S - \mu_A)X_A - (\alpha_B + \alpha_C)X_A + F_A \quad \textbf{(1)}$$

$$\dot{X_B} = (\delta_B + S - \mu_B)X_B + \alpha_B X_A + F_B \quad \textbf{(2)}$$

$$\dot{X_C} = (\delta_C + S - \mu_C)X_C + \alpha_C X_A + F_C \quad \textbf{(3)}$$

Here, noise is captured by a stochastic addition to the combined rates of proliferation and death. The stochastic noise, S_θ, is drawn from a normal distribution and is assumed, for simplicity, to be the same for all cell types. The last term in each equation accounts for the flux of cells, F_θ, into a lattice site which depends on the cell's motility rate, J_θ. In the absence of any biases, these fluxes are proportional to the cell density gradient for a specific cell type, summed over all nearest neighbor sites, with a constant of proportionality reflecting the motility of the cell type (Equation 4).

$$F_\theta^{Net\ i} = \sum_{j \in n.n\ of\ i} J_\theta\left(X_\theta^j - X_\theta^i\right) \quad \textbf{(4)}$$

The range of physiologically relevant migration, proliferation, and differentiation rates we used were derived from various literature sources. For example, it has been reported that ECs and SMCs can have a maximum displacement distance of 18μm and 44μm over the course of an hour, respectively (125,128). Additionally, proliferation rates for mouse ECs have been reported to have a maximum doubling time of 19 hours (129) while 22 hours has been reported for rat vascular SMCs (130). Lastly, the rate of differentiation can be considered as the length of time for specific EC or SMC maker expression. Some studies

have reported initial EC marker expression at as early as 24hrs post induction(131) and 36hrs for SMC marker expression(43). Using these physiologically relevant values for our parameters (**Table 1**), our simulations were evolved in time using the Euler (first order Runge-Kutta) method implemented in Python(132). Each cell's population density, at each lattice site, is tracked over time (recorded every 1hr in time) and can be reconstructed to create a 2D spatial representation of the evolving cell populations using MATLAB(133) (**Appendix Fig. S2A-C**).

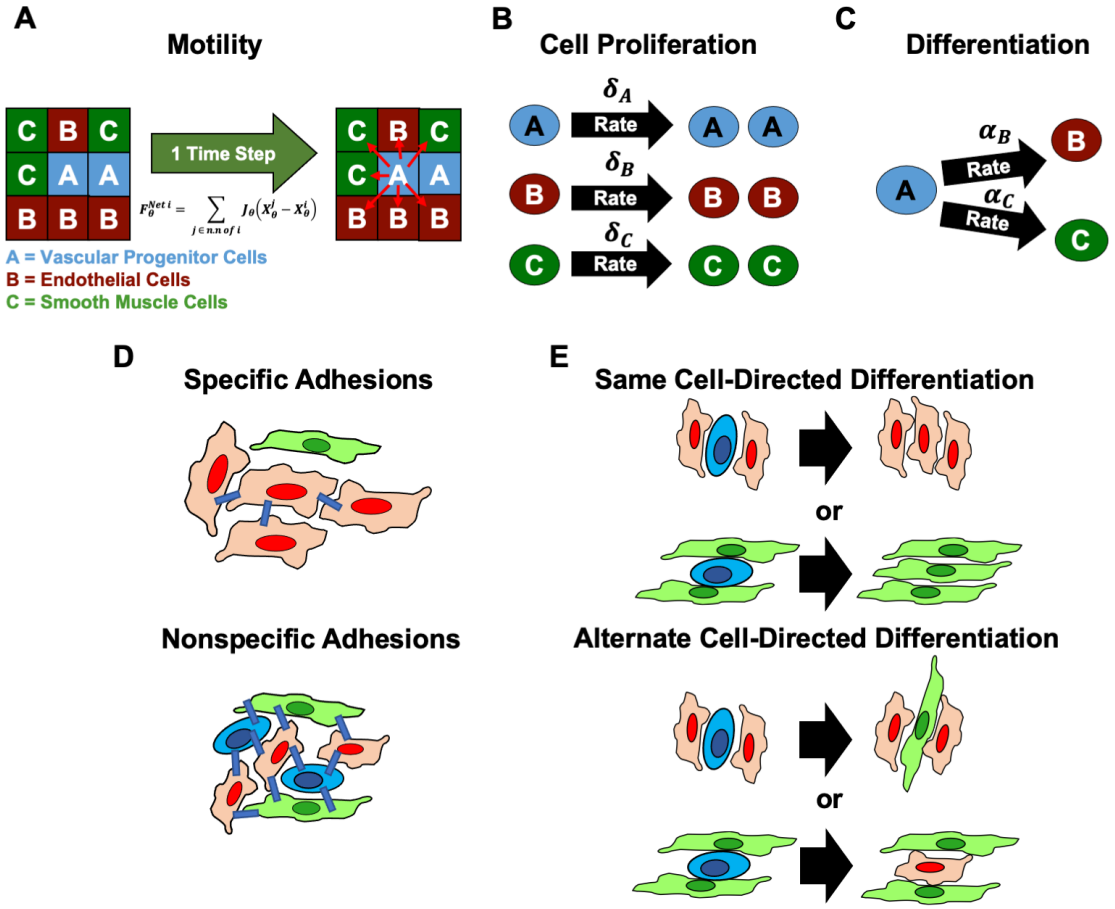

Figure 2. Modeling process

A) In the absence of any sensing directed motility, J_θ, cell migration is governed by the flux, F_θ, of cells moving between lattice sites due to cell density gradients. The schematic illustrates how there is a net movement of VPCs into lattice sites that contain fewer VPCs. In the case where concentrations are equal no net movement occurs. **B)** Cell proliferation, δ_θ, is assumed to be symmetric where one cell type will always produce more of the same cell type at a specified rate. **C)** Cell differentiation, α_θ, is assumed to be a nonreversible fate decision made by VPCs (A cells) being driven towards one of two possible mature cell types: ECs (B cells) and SMCs (C cells) at rates α_B and α_C, respectably. **D)** We assume contact inhibition to regulate the proliferation and motility of the cells. One such mechanism would be mediated by specific adhesions, where cells only sense cells of the same identity. Alternatively, they can be mediated by nonspecific adhesions, where cells indiscriminately sense other cells. **E)** Paracrine signaling is similarly dependent on the local cellular microenvironment via biochemical cues that nudge VPCs towards a specific fate identity, EC or SMC, respectively. Here two possible mechanisms arise, same cell-directed differentiation where committed cells, ECs or SMCs, direct the differentiation of VPCs into the same cell identity, or alternate cell-directed differentiation where committed cells influence the differentiation of VPCs into the opposite cell type.

2.2.6. Contact Inhibition and Paracrine Signaling

Under the simplest assumption, the various rates are constants that depend only on the specific cell type. However, these rates can also be modulated by different types of external cell interactions, such as contact inhibition and paracrine signaling(37,134). To explore how these external processes affect patterning, we accounted for their promotion or suppression of the corresponding rate constants for motility, proliferation, and differentiation.

To model the effects of contact inhibition, we assumed that a cell's motility rate would simply decrease linearly with the number of cells in its immediate neighborhood (summed over the site and all nearest neighbor sites)(135). Within this scheme, we examined two distinct possibilities, specific and nonspecific cell adhesions, as possible regulators (**Fig. 3D**). For specific, homotypic, cell adhesions we assumed that cells can only sense and interact with other cells of the same cell identity, leading to a modified motility rate,

$$J_\theta = J_\theta^o \left(1 - \left(\frac{X_\theta^i + \sum_{j \in \dot{n.n\ of\ i}} X_\theta^j}{\mathrm{z}} \right) \right) \quad \textbf{(5)}$$

where *i,j* are site indices and z is the coordination number of nearest neighbor lattice sites plus the current site (z = 9). The migration rate thus decreases from a maximum for isolated cells to zero when the cell density of the same type is maximal. For nonspecific cell adhesions, we assume cells can sense all other cells in their local neighborhood (leading to equation 6).

$$J_\theta = J_\theta^o \left(1 - \left(\frac{\sum_{\theta \in \dot{A,B,C}} [X_\theta^i + \sum_{j \in \dot{n.n\ of\ i}} X_\theta^j]}{z} \right) \right) \quad \textbf{(6)}$$

Here, the motility rate decreases from a maximum for isolated cells to zero when the overall cell density for all cells is maximal. Combinations with different cell types employing different sensing mechanisms were also explored. For example, ECs nonspecifically sensing its neighboring cells, leading to greater contact inhibition, while SMCs were assigned to specifically sense other SMCs (homotypic sensing). It is to be noted that patterning arising from variations in adhesion is consistent with the differential adhesion hypothesis(136), which states that cells with strong attractions will cluster closely together while those with weaker attractions will surround them. Here we account for the motility of cells being differentially affected by differences in cell adhesion dynamics such as specific vs nonspecific sensing. An example of a strong (homotypic) cell-cell adhesion would be vascular endothelial cadherins (VE-cadherin) that hold ECs

together(137), while E-cadherin which binds ECs to SMCs is an example of a nonspecific cell adhesion(138).

A similar approach was implemented for modifying the proliferation rates based on homotypic and nonspecific cell adhesion. We assumed that proliferation would linearly decrease as the number of neighboring cells increased, in accordance with evidence demonstrating that the mitotic rate may be arrested when a critical cell confluency is achieved. This type of contact inhibition emerges from an increase in mechanical interactions resulting from the loss of available space, thus constraining cellular dynamics including cell division(82). It is also possible for arrest to occur in a specific manner such as being mediated by the EC specific Notch signaling pathway that inhibits tip-EC proliferation during angiogenesis (139). Therefore, we modified the proliferation rates appropriately to account for two different sensing mechanisms: 1) specific, homotypic, cell sensing:

$$\delta_\theta = \delta_\theta^o \left(1 - \left(\frac{X_\theta^i + \sum_{j \in n.n\ of\ i} X_\theta^j}{z} \right) \right) \quad \textbf{(7)}$$

and 2) nonspecific cell sensing:

$$\delta_\theta = \delta_\theta^o \left(1 - \left(\frac{\sum_{\theta \in A,B,C} [X_\theta^i + \sum_{j \in n.n\ of\ i} X_\theta^j]}{\mathrm{z}} \right) \right) \quad \textbf{(8)}$$

These proliferation rate dependencies are analogous to equations 5 and 6 for the migration rates, with a coordination number (z) equal to 9.

For differentiation, we examined how chemical signals and growth factors produced by the cells influence VPC fate decisions, modeling vascular paracrine signaling(140). Such signaling is observed in EC and SMC recruitment during early vascular development, with ECs secreting platelet-derived growth factor-b when recruiting SMCs(137). We explored two possible mechanisms for guiding VPC differentiation into ECs and SMCs. The first mechanism, designated same cell-directed differentiation, involves a committed cell, EC or SMC, inducing a neighboring uncommitted VPC to differentiate into a cell of the same identity. The second mechanism, designated alternate cell-directed differentiation, assumes a committed cell, such as an EC, influencing a neighboring VPC to instead differentiate into the alternative cell type, in this example inducing it into a SMC (**Fig. 2E**). For simplicity we assumed an isotropic distribution of paracrine signals for both cell types, where the diffusion range is equivalent to one lattice unit. Given that our lattice size is 79μm (see next section), this is a reasonable upper bound for diffusive signal propagation. The modified differentiation rate is then given by

$$\alpha_\theta = \alpha_\theta^o \left(1 \pm \beta \left(\frac{X_{\theta'}^i + \sum_{j \in n.n\ of\ i} X_{\theta'}^j}{z} \right) \right) \quad \textbf{(9)}$$

where the choice of EC or SMC, for q and q', determines the type of cell-directed differentiation mechanism (**Supplemental Fig. S3**) and β represents the strength of the signaling from cells in neighboring lattice sites.

2.2.7. Simulations

At time 0 (t=0), a fraction of our 50x50 lattice is randomly seeded with VPC population densities, $X_{A,}$ with values taken from a normal distribution between [0, 1]. Here each unique lattice site supports up to 10 cells and has a lattice length of 79μm (**Appendix Fig. S2A**). This choice of lattice size was motivated by the average cell size of our VPCs, measured to be 25μm ± 7μm across (**Appendix Fig. S2D-E**), whereby each lattice site is significantly larger than 1 cell diameter, so that our population-based approach remains valid, and yet small enough to visualize the population driven micropattern features consisting of mature cell clusters with effective diameters of 340μm ± 110μm (**Appendix Fig. S1G**). The fraction of sites seeded was chosen such that the seeded density for the array was consistent with experimental cell seeding densities of VPCs, at 10^4 cells/cm^2(37). A motility constant value was derived from the distance traveled by human umbilical vein ECs, of about 14μm over an hour (125). Taking it to be a random walk process, we can compute an effective diffusion constant, D, from mean-squared displacement ($\langle r^2 \rangle \sim (14\mu m)^2$) and the time taken (t), as $\langle \mathbf{r}^2 \rangle / 4t = \mathbf{D}$. Non-dimensionalizing D using the lattice site dimensions (79μm) as the unit of length and 1hr as the unit of time, we calculated a corresponding dimensionless motility constant of J_θ = 0.0079. Additionally, we chose to fix the rate values for proliferation and differentiation within physiological ranges (**Table 1**). These rates were calculated from the typical times associated with the given processes. When proliferation or differentiation rates were not being varied, we set the combined rate of proliferation for all cells to 40hrs (129,130,141), corresponding to a dimensionless simulation value of δ_θ = 0.025. The differentiation rate was set to 62.5hrs (45) thus falling between days 2-3 of post stage 2 differentiation, corresponding to a simulation value of α_θ = 0.016. Once the simulation is initialized, the three first order ODEs, equations (1-3), are evolved in time using the Runge-Kutta method, and X_θ values are recorded at every lattice site at 1-hr intervals for the duration of the simulation (**Appendix Fig. S2B-C**).

After every timestep, the cellular densities, $X_{A,B,C}$, for any lattice site that exceed a total of 10 cells, or where the $\sum X_{A,B,C}$ is greater than 1, are rescaled such that the relative ratios of the different cell types are kept constant while maintaining the total cell number, per lattice site, at its maximum cell value of 10 corresponding to a maximum cellular density of 1. At t=96 hours, corresponding to experimental data at day 4, this information is quantified and analyzed. Supplemental video V2, shows a simulation evolving in time, for

a particular set of parameter values. We conducted parameter sweeps over regions of parameter space that include experimentally relevant and physiologically plausible (**Table 1**) values for each set of parameters. Simulations were run a total of 10 times for each set of parameters for statistical analysis.

2.3. Results

2.3.1. Role of Cell Motility

We first explored the role that motility for EC (B cells) and SMC (C cells) has on the emerging micropattern. Our parameter sweep explored physiologically relevant motility values, such as displacement lengths between 0 – 18μm for ECs and 0 – 44μm for SMCs over the course of an hour (125,128) these correspond to *in silico* values equal to $J_B = 0 – 0.013$ and $J_C = 0 – 0.078$, respectively. We varied the ECs' (J_B) and SMCs' (J_C) motility rates while holding the VPC's (A cell's) motility (0.0079) constant and setting all other parameters, such as differentiation (0.016), proliferation (0.025), and noise (0.01) to be the same for all three cell types (**see Table 1**). The fractions of ECs at t=96 hours were then plotted over this parameter space (**Fig. 3A**). We verified that roughly equal motility values for J_B and J_C, generated relatively equal population densities of ECs and SMCs (EC fraction ~0.5). The spatial distribution of cells in this regime also revealed micropatterning, defined as spatially separated regions dominated by one cell type or the other (**Fig. 3B *i-iv***). We observed that the micropatterning persists but becomes less distinct as the overall motility rates increased (**compare Fig. 3B *i* to *iv***). Moreover, we observed micropatterning over a broad range of EC fractions, roughly between 0.3 to 0.7, demarcating a region termed "*zone of co-emergence*" (**Fig. 3A**). This zone of co-emergence was further explored in cell asymmetry plots (**Appendix Fig. S4A**), where asymmetry is calculated as $(B_T-C_T)^2/(B_T+C_T)^2$ where B_T and C_T are the total number of ECs and SMCs in the simulated space at t=96 hrs. Here values of asymmetry close to 0 indicate similar population densities of ECs to SMC enabling pattern formation, while values closer to 1 denote the dominance of one cell type and no micropatterning. The corresponding zone of co-emergence can be distinctly observed at asymmetry values up to 0.3 (**Appendix Fig. S4A**). The standard deviations from the stochastic effects introduced are averaged over 10 simulations and were observed to be insensitive to repeated run with any variance localized withing the zone of co-emergence (**Appendix Fig. S4B**). Next, we looked at the cases where one cell type migrated an order of magnitude faster than the other cell type. Not surprisingly, we saw that the faster cell type physically dominates and outcompetes the space taken up by the slower cell type (**Fig. 3B, *v* and *vi***). However, even a more modest difference of about 50% in the motility rates allowed the faster cell type to dominate (**Fig. 3B *vii* and *viii***). In fact, upon further investigation, the zone of co-emergence, is highly sensitive to differences in motility rates and with differences as small as roughly half a cell size per hour (~4.5μm/hr), we observe a significant dominance of the faster cells (**Appendix Fig. S5**).

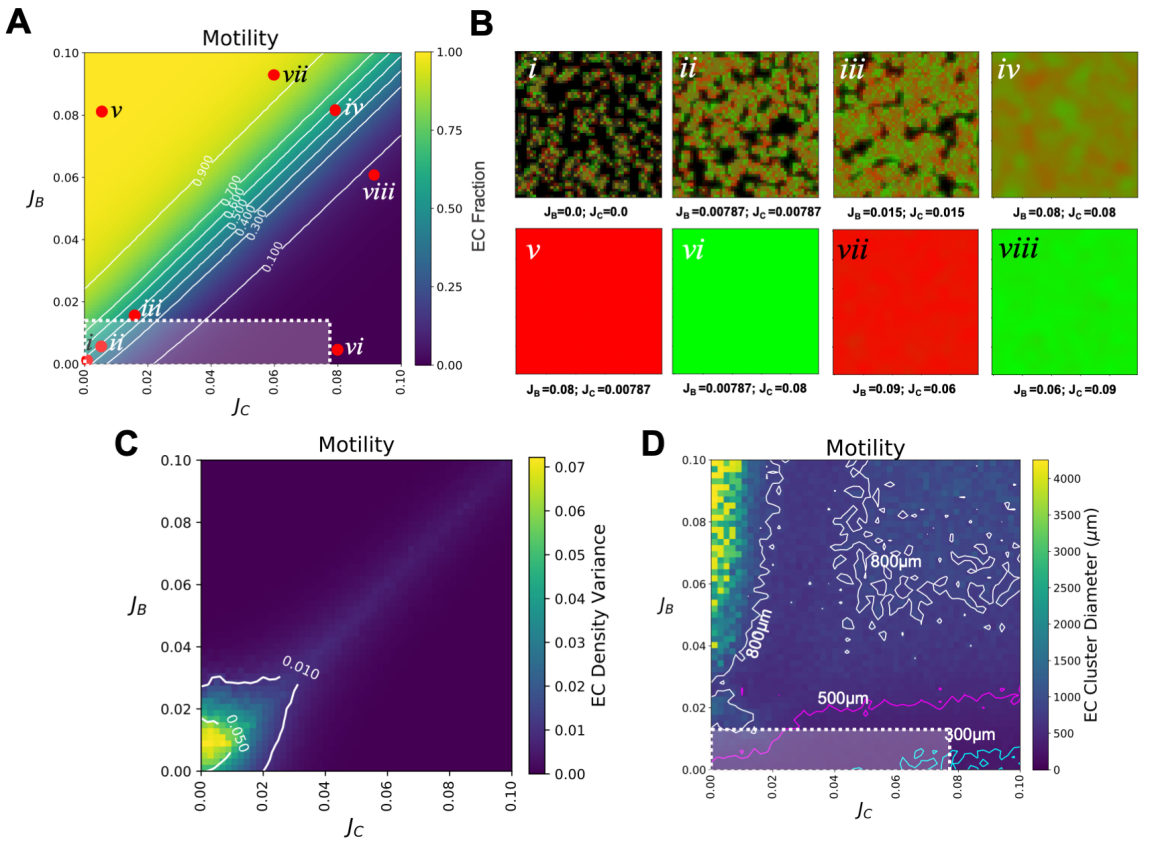

Figure 3. Effect motility has on micropatterning.

A) Parameter sweep for motility (in the absence of sensing) was explored by varying J_B and J_C values while holding differentiation and proliferation rates constant. Shown here are the EC (B cell) fraction. Note: the presence of the zone of co-emergence, a region of parameter space where micropatterning is observed (defined by the area between 0.3~0.7 of EC fraction). **B)** Examining different combinations of J_B and J_C reveals the type of micropattern that develops after 96 hrs. Shown here, are the resulting pattern from within the zone of co-emergence (*i, ii, iii,* and *iv*), and from outside the zone of co-emergence where the faster cell type dominates (*v, vi, vii,* and *viii*). **C)** EC density variance plots show where distinct EC clusters emerge as motility is varied. **D)** Parameter sweeps of mean effective EC cluster diameter distributions: with contours 300μm-cyan, 500μm-magenta, and 800μm-white. White squares in **A)** and **D)** denote the physiologically relevant region of the parameter space. Defined, for motility, as being the maximum speed that a single EC and SMC can migrate/move over a given amount of time. For motility those bound are between 0 – 0.013 for J_B and 0 - 0.078 for J_C corresponding to an upper limit representing the maximum reported single cell velocity, 18μm/hr for ECs and 44μm/hr for SMCs.

The region of parameter space within the zone of co-emergence where micropatterning occurs was next explored. To do this, we quantified the spatial separation between the cell types, by measuring EC density variance, $Avg[(X_B-X_{Avg(B)})^2]$, where X_B is the density of ECs at a given lattice site and $X_{Avg(B)}$ is the average density of ECs taken over the entire simulated space at t = 96hr (**Fig. 3C**). Here, values close to 0 suggest no distinct phase separation/clustering of the ECs. While positive values indicate varying degrees of phase separation between individual lattice sites. As expected, we see a faint positive streak whose position mirrors the zone of co-emergence from the EC fraction plots (**Fig. 3A**). This positive streak approaches 0 with increasing motility values for both ECs and SMCs and aligns with the simulated micropattern mixing observed under high motility values (**Fig.**

3B.*iv*). Interestingly, micropatterns at lower motility values, and where lattice site mixing is lessened, were observed to have greater phase separation and therefore were more distinct (**Fig. 3C**).

Finally, to quantitatively compare the simulated micropattern predictions with experimentally observed micropatterns, we measured the distributions of EC cluster diameters, based on their effective cluster diameters. We found that the majority of the simulated EC cluster diameters, within the physiological range of motility, would generate EC clusters with effective diameters between 300-800μm (**Fig. 3D**) and with a similar standard deviation (**Appendix Fig. S4D**). The boundary for the physiological range, $J_B = 0 – 0.013$ and $J_C = 0 – 0.078$, is outlined by white dashed lines and is representative of the maximum reported motility values for ECs (125) and SMCs (128) (**Fig. 3D**). Again, the experimentally observed EC cluster diameters were found to be between 340μm ± 110μm (**Appendix Fig. S1**). This indicates that our simulations do account for the experimentally observed patterning within the explored physiological range. Lastly, the EC cluster distribution diameters within the corresponding zone of co-emergence increased as motility increased for both cell types. At very high motility rates, well outside the experimental range, clusters with effective diameters exceeding 800μm emerged (**Appendix Fig. S4A**), though patterning became less distinct (**as seen in Fig. 3B *iv***).

2.3.2. Role of Cell Proliferation

Next, we performed a parameter sweep of proliferation rates in the absence of any sensing mechanisms (**Fig. 4A**). Proliferation rates were varied for ECs (B cells, δ_B) and SMC (C cells, δ_C), while the proliferation rate for VPCs (A cells, δ_A) and differentiation and motility rates for all cells were fixed at their experimentally relevant values (**Table 1**). The parameter sweep explored physiologically reasonable proliferation rates ranging from no cell division ($\delta_\theta=0$) to divisions occurring as fast as every 10 hours ($\delta_\theta=0.1$). With regard to ECs and SMCs, it has been reported that they exhibit a maximum doubling time of 19 hours for mouse ECs (129) and 22 hours for rat vascular SMCs (130). This physiological region is encased by white dashed lines in **Fig. 4A**. Similar to cell motility, the parameter sweeps here revealed that roughly equal rates of proliferation for ECs, δ_B, and SMCs, δ_C, lead to the formation of a zone of co-emergence along which micropatterning develops (**Fig. 4B *i-iii***). At the center of the proliferation parameter sweep, where δ_B and δ_C are both 0.05, we found highly distinct micropatterning emerge (**Fig. 4B *ii***). As expected, co-culture patterning largely developed within the confines of the zone of co-emergence with any outside conditions leading to the faster growing cell dominating (**Fig. 4B *iv-vi* and Appendix Fig. S4E**).

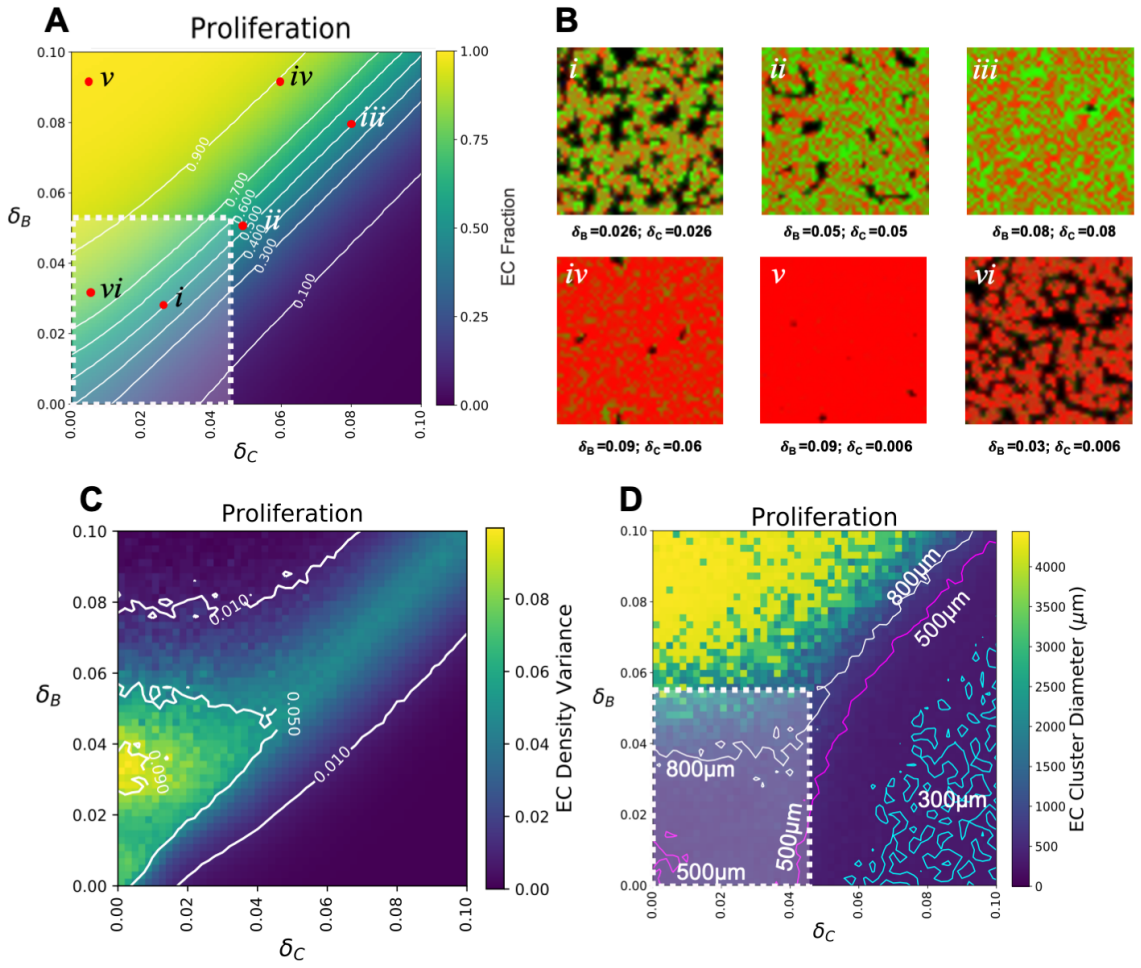

Figure 4. Effect proliferation has on micropatterning

A) EC (B cell) fraction parameter sweep for varying proliferation rates, in the absence of sensing, while holding differentiation and motility constant. **B)** Different combinations of δ_B and δ_C reveal the types of micropattern that develops after a 96hr simulation. Shown here are micropatterns that emerge along the zone of co-emergence *i-iii*) and those outside the zone *iv-vi*). **C)** EC Density variance plots for distinct EC clusters as a function of varying proliferation rates. Positive values indicate varying degrees of EC cluster separation as defined by a greater EC density than the total averaged EC density per condition. **D)** Parameter sweeps of mean effective EC cluster diameter distributions. Contours here denote the relative cluster diameters that result as the rates are varied: counters denote 300μm-cyan, 500μm-magenta, and 800μm-white. Outlined in white in **A)** and **D)** is the physiological region defined, for proliferation, as the area bound between 0 - 0.055 for δ_B and 0 – 0.045 for δ_C. The upper limit of which correspond to a cell's maximum doubling time, here 18 hours for ECs and 22 hours for SMCs.

We then looked at the EC density variance plots which show regions where distinct micropatterns of ECs emerged as a function of proliferation rates (**Fig. 4C**). It was observed that varying proliferation rates allowed for a larger span of conditions where phase separation, defined as having an EC cluster density greater than zero, and thus micropatterning emerge. Similar to motility, we observe enhanced phase separation along the zone of co-emergence (**Fig. 4B *i-iii***). Interestingly, we observed that some phase separation persisted beyond the zone of co-emergence, where conditions favoring EC

proliferation rates over SMC rates (**Fig. 4C**). In these instances, it was observed that the emerging EC clusters were predominately islands of various sizes, and while SMCs were present, they did not in fact surround EC clusters. Additionally, a region of high phase separation, where the EC density variance value was greater than 0.08, was observed at a low SMC proliferation rate, δ_C, and an EC proliferation rate of 33hr, $\delta_B = 0.03$. This region, which again is outside the zone of co-emergence, consisted largely of only ECs clusters (**Fig. 4B *vi*, Fig. 4C** yellow region).

Lastly, we measured the distribution of EC cluster diameters and found that they consisted of clusters whose effective diameters were roughly between 500-800µm, within the physiological range (white dotted lines, **Fig. 4D**), and with a similarly broad standard deviation distribution at 300-800µm (**Appendix Fig. S4H**). Finally, as proliferation rates linearly increased for both ECs and SMCs a narrowed and persistent region of EC clusters, between 500µm and 800µm, emerged and mirrored the position of the zone of co-emergence (**Fig. 4D**).

2.3.3. Role of Differentiation

Next, we explored the role that differentiation plays in the emergence of micropatterns in the absence of any sensing or signaling. The parameter sweeps were conducted by varying the differentiation rates for both ECs (B cells, α_B) and SMCs (C cells, α_C) accounting for no differentiation, $\alpha_\theta=0$, and a differentiation rate of 10hrs, $\alpha_\theta=0.1$, while holding the motility and proliferation rates constant and at experimentally relevant values (**Table 1, Fig. 5A**). Narrowing down the physiologically relevant parameter space for differentiation proved to be a difficult task given the variable nature of influencing effects (e.g., chemical, mechanical, and/or contact mediated). Therefore, we defined the physiologically relevant differentiation rate range as that between the first/early marker expression to the time point where the given marker expression peaks, indicating a mature phenotype. For mouse ECs it has been reported that VE-cadherin, a known EC marker, expression can be observed as early as 24hrs post induction(131), corresponding an upper limit of $\alpha_B=0.042$. Additionally in one of our previous study, we showed that VE-Cadherin peaks in differentiating mouse cells around day 14 post induction (37), corresponding a lower limit of $\alpha_B=0.003$. For mouse smooth muscle cells, early marker expression of α-smooth muscle actin (α-SMA) has been reported at 36hrs post induction(43), thus establishing an upper limit of $\alpha_C=0.028$. Furthermore, peak α-SMA expression is reported to arise on day 15 (142), corresponding a lower limit of $\alpha_C=0.0028$. Upon analysis of the EC fraction parameter sweep, we noticed the absence of a sharply defined zone of co-emergence (**Fig. 5A**), defined as EC fractions roughly between 0.3 to 0.7, and instead saw a large fanned out area of parameter space exhibiting micropattern formation (**Fig. 5B *i-iii*).** As expected, when both differentiation rates, α_B and α_C, are zero only VPC (A cells) are present (**Fig. 5B *iv***). Additionally, a loss of patterning only occurred when the differentiation rate of one cell type exceeded the other cell type by more than 2-3 times (**Fig. 5B *v-vi***). This is reiterated in the asymmetry plots (**Appendix Fig. S4I**) and in the EC

density variance plots (**Fig. 5C**), where an increasing gradient of EC density variance values is observed rather than the localized pockets of phase separation observed in the motility and proliferation EC density plots. This gradient highlights the lack of impact that differentiation rates ultimately have on pattern formation as long as the relative differentiation rates of either cell type do not exceed the other by 2-3 times. Lastly, the EC cluster diameter distribution was also observed to be fairly consistent with cluster diameters ranging from 350µm to 800µm for the total explored parameter space (**Fig. 5D**). A similarly broad range was recorded for the standard deviation, 100µm to 500µm (**Appendix Fig. S4L**). To further explore the lower limits of the differentiation rates we repeated our simulations focusing on these longer differentiation periods. Here the range of interest was between 0.001 to 0.01, corresponding to differentiation rates of 1,000hrs to 100hrs. Unsurprisingly, we did not see any defining differences at these lower bounds (**Fig. 5E-G**).

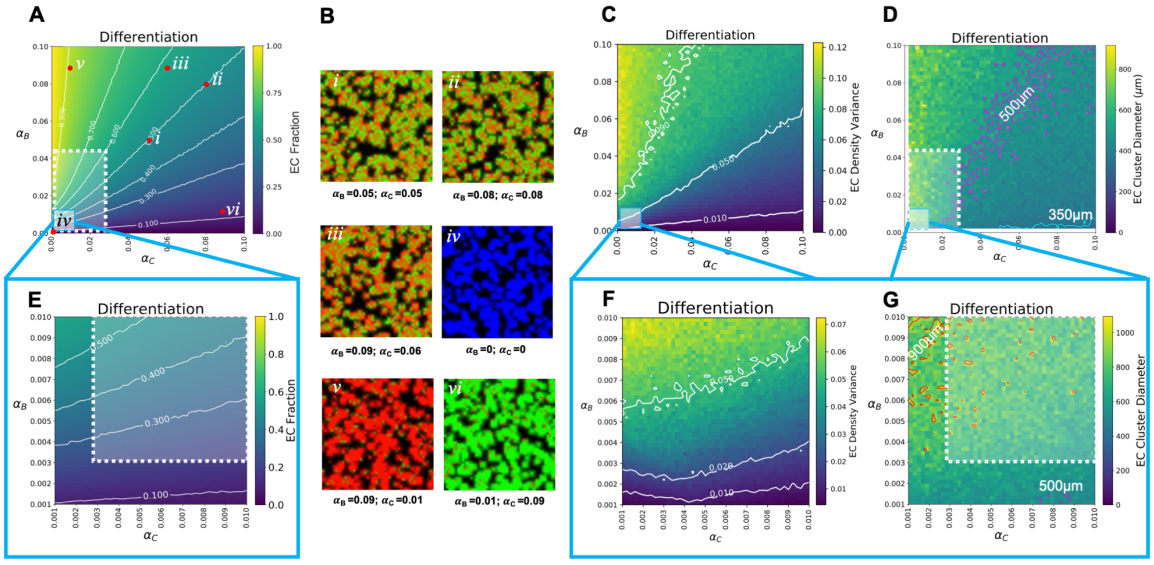

Figure 5. Effect differentiation has on micropatterning

A) EC (B cell) fraction parameter sweep for varying differentiation rates, in the absence of cell signaling, while holding proliferation and motility rates constant. **B)** Different combinations of α_B and α_C reveal the types of micropattern that develops after a 96hr simulation. Shown here are micropatterns that emerge within what we consider the region of co-emergence *i-iv*) and those outside the region *v-vi*). **C)** EC Density variance plots for distinct EC clusters as a function of varying differentiation rates. **D)** Parameter sweeps of mean effective EC cluster diameter distributions. Contours here denote the relative cluster diameters that result as the rates are varied: counters denote 350µm-cyan, 500µm-magenta. Further exploration of the lower bounds for differentiation are shown in **E-G)** corresponding to **E)** EC Fraction, **F)** EC density variance, and **G)** EC cluster diameter distribution. Here the white boundaries indicate the physiologically relevant domain for differentiation. The bounds are between 0.003 – 0.042 for ECs and 0.0028 – 0.028 for SMC corresponding to a differentiation rate of 24hrs to 14 days for ECs and 36hrs to 15 days for SMCs.

Table 1 Parameter values used in model.

Variables are fixed at these experimentally obtained values for motility, proliferation, and/or differentiation while explicitly varying others. *In silico* unit time step corresponds to 1 hour and unit length corresponds to 79µm (the lattice size).

Variable	Denotation	Experimentally obtained values	Corresponding simulation value(s)	Parameter sweep	References
Diffusion constant	J_θ	14 μm^2/hr	0.0079	0 – 0.1; 0.001 step size	(78-79)
Proliferation rate	δ_θ	~40 hr	0.025	0 – 0.1; 0.001 step size	(80-82)
Differentiation rate	α_θ	~62.5 hr	0.016	0 – 0.1; 0.001 step size	(121-122)
Stochastic noise	S_θ	A loss or gain of up to 1 cell per lattice site is incorporated every 10 hrs	± 0.01	N/A	NA
Paracrine signal strength	β	amplification of differentiation rates by 0.5-1.5	± 0.5, ±0.016, 0	N/A	NA

2.3.4. Dynamics of single cluster growth: linear vs ballistic diffusion

So far, the results suggest that it is the post-differentiation migration and well-balanced proliferation of the cells that lead to cell patterning. A defining feature of this micropatterning that emerges within the zone of co-emergence is the size of the EC clusters. To understand the effect that migration and proliferation have on a cluster's growth and size, we focused on the growth dynamics of a single EC cluster. We initialized the simulation with 10 cells at the center of the simulation site. As the ECs migrate and proliferate into neighboring lattice sites, the extent of their spreading can be calculated and visualized over time. To do this, we constructed a one-dimensional visualization of the EC spread over time by plotting the EC population along the x-axis as a function of time (**Fig. 6A**). For physiological rates, i.e., when $J_B = 0.0079$ and $d_B = 0.025$, we observed a rapid exodus from the center lattice site into the vacant neighboring lattice sites over time. Additionally, we observed two different regions emerge in the growing EC cluster. First, a leading diffusive front consisting of fractional EC densities, defined as densities between 0.1 and 1 cells per lattice site. Second, a growing/expanding inner core, defined as the center region of the cluster where at least 2 ECs are present, here the inner core consisted of more than 2 ECs with a max of 4 ECs at its center (**Fig. 6B** inset).

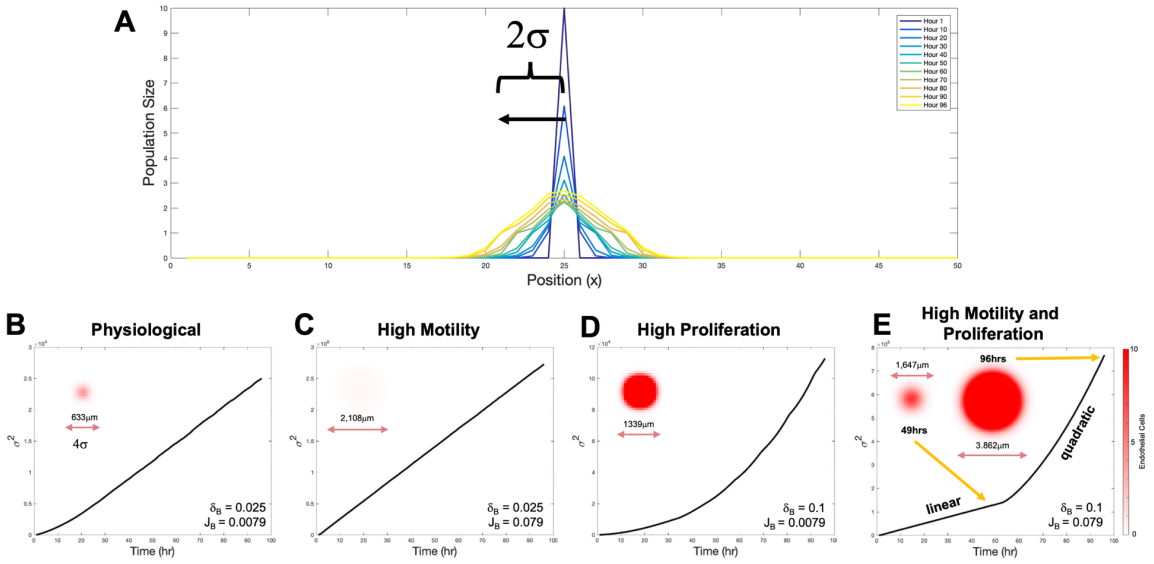

Figure 6. Single EC cluster growth dynamics

A) Plot of EC cluster growth over time along the x axis. Here the spread is defined as 2s where s is the directional growth and diffusion along one of the x axis directions viewed from the center of the growing EC cluster. MSD plots over time for **B)** physiological conditions, **C)** under high motility rates, **D)** under high proliferation rates, and **E)** under both high motility and high proliferation rates. Inset here are the different EC cluster morphologies that emerge as a result from these rates.

To quantify the size of the cluster, we then calculated the radius of gyration of the cluster in the x-direction, defined as $\sigma^2 = \sum(x_i^2 * P_{EC}(x_i))$ where x_i is the lattice position and $P_{EC}(x_i)$ is the normalized EC population density along the x-axis such that $P_{EC}(x_i)$ is equal to $X_B(x_i) / \sum(X_B(x_i))$. The radius o gyration was then plotted over time (**Fig. 6B-E**) followed by a linear and/or quadratic fit with corresponding R^2 values (**Appendix Tables 1-4**). Here, we considered four different cases (i) physiological migration and proliferation rates (where $J_B = 0.0079$ and $d_B = 0.025$), (ii) high migration (J_B=0.079) with a physiological proliferation rate (d_B=0.025), (iii) physiological migration (J_B=0.0079) with a high proliferation rate (d_B=0.1), and finally (iv) high migration (J_B=0.1) with a high proliferation rate (d_B=0.1).

For case (i), with both physiological rates, a linear fit was sufficient to describe the time dependence of the radius of gyration (**Fig. 6B**), R^2 value of 0.997 (**Appendix Tables 1& 2**). Using the slope of the linear fit, we were able to determine the diffusive rate of the spreading EC cluster to be 281mm^2/hr. Taking the diameter of the cluster to be approximated by 4 s (which contains 95% of the cells for a Gaussian distribution) allows for direct comparisons with cluster diameters from simulations and experiments that were obtained by binarizing and thresholding images. In this case, we obtain a cluster with diameter 633μm after 96hrs. It is to be noted that this diameter is for a single cluster, in the absence of other competing cell types, is much larger than the measured values from experiments and simulations of about 350 mm. This suggests that the leading

diffusive front region of the cluster with low cell densities is potentially outcompeted by the surrounding cell type with only the inner core region surviving as a cluster in the competitive environment. Indeed, the inner core region for these physiological parameter values is roughly half the diameter of the full cluster (**Fig. 6B**) yielding a radius of about 320 mm, consistent with measured cluster diameters in the experiment.

For high (10 times greater) migration rates and physiological proliferation rates, we find that a linear fit can still explain the radius of gyration time dependence (R^2=1). As expected, the diffusive constant is roughly 10 times greater than the physiological conditions' at 2,931mm^2/hr. The measured cluster diameter at 96hrs is also much larger at 2,108μm (**Fig. 6C**). Moreover, we observed that the growing cluster does not retain its dense EC inner core, but rather the whole cluster is completely composed of fractional cell densities (lattice sites containing less than one EC). Consequently, while the increase in migration does ultimately produces a larger cluster, the lack of the core as visualized in the cluster by the absence of a bright red area (**Fig 6C inset**) indicates there may not be any distinct clusters in the competitive environment with multiple cell types. This is consistent with the lack of distinct patterning reported at high migration rates in our simulations (**Fig 3B**).

Next, we explored physiologically typical migration rates with high (4 times greater) proliferation rates. Here we noticed that the radius of gyration time dependence (**Fig. 6D**) could not be fit by linear function and was better fit by a quadradic (R^2=0.999) (**Appendix Tables 3 & 4**). From this quadratic fit we could extract the ballistic growth speed of the cluster, which we found to be 15.3mm/hr. The ballistically growing cluster was observed to display both a smaller leading edge composed of fractional ECs and a larger growing inner core composed of saturated EC lattice sites (bright red area within the cluster consisting of 10 ECs per lattice site **Fig. 6D inset**). This cluster was calculated to have a diameter of 1339μm (compare to diameter of 633μm in the physiological case) demonstrating that proliferation alone can drive the growth of the cluster significantly. The presence of a dominant inner core region suggests that high proliferation can also lead to clusters that are distinct in situations where both cell types are present.

Lastly, for both high migration and high proliferation rates, both linear and quadradic regimes (**Fig. 6E**) were observed, indicating that a transition occurs in the growth dynamics of the cluster, specifically from linear diffusive spread to ballistic growth. We estimated the transition time point as the time at which the R^2 value of the linear fit falls below 0.99, which in this case was at 49hrs (**Appendix Table 5**). A quadratic fit on the remainder of the radius of gyration curve resulted in an R^2 value of 0.9996 (**Appendix Table 3 & 4).** This suggests that high proliferation rates can act as an additional driving force leading to an increasing in cluster size, while migration can synergistically enhance the ballistic growth phase. This is apparent when comparing the cluster size at various

time points. At 49hrs, just after the diffusive growth state, the cluster size is 1,647mm, while at 96hrs the cluster is at 3,862mm.

2.3.5. Contact Inhibition of Cell Motility

In typical cell culture systems, cells sense and often adhere to their neighboring cells via integrin and cadherin binding proteins. These types of cellular interactions have been shown to regulate the cell's migration through contact-mediated inhibition(134). We, therefore, incorporated these effects into our model by appropriately modifying the motility rates to allow for specific (Sp) and nonspecific (Nsp) cell adhesions, equations (5) and (6). We examined the three possible distinct combinations of these dependencies: B_{Sp}-C_{Sp}, B_{Nsp}-C_{Sp} (same as its inverse), and B_{Nsp}-C_{Nsp} (**Fig. 2D**). The results show that when both cell types display specific adhesions (B_{Sp}-C_{Sp}), the zone of co-emergence, EC fractions between 0.3 and 0.7, is blurred and broadened (**Fig. 7A**) compared to the control case with no contact-inhibition (**Fig. 3A**). At higher motility, the contour lines exhibit a slight concave curve due to these cells' motility being slowed down more significantly as a result of their adhesions (**Fig. 7A**). Indeed, when one cell type displays specific adhesions and the other displays nonspecific adhesions (B_{Nsp}-C_{Sp}), the line of co-emergence curves towards the nonspecific adhering cell type (**Fig. 7B**), indicating that the non-specifically adhering cells are more constrained. Lastly, when both cell types display nonspecific cell adhesions (B_{Nsp}-C_{Nsp}) they are similarly slowed indicated by the resulting linear contour lines (**Fig. 7C**). These trends are similarly visualized in the corresponding asymmetry plots (**Appendix Fig. S6A-C**). The EC density variance (**Appendix Fig. S6G-I)** shows fairly distinct micropatterning is present within the zone of co-emergence in all cases except when both cell types have high migration values. The patterning is dramatically more distinct in the zone of co-emergence when one cell type displays specific adhesions and the other displays nonspecific adhesions (**Appendix Fig. S6H**). Thus, certain combinations of sensing mechanisms can actually increase the robustness of the patterning.

2.3.6. Cell Density Dependent Proliferation

It is well-known that highly confluent monolayers of many cell types will eventually cease to proliferate due to contact inhibition, a loss of surface area, as well as, a corresponding increase in mechanical constraints(82). We implement this in our model by modifying the cell proliferation rates based on the local cell density with either specific or nonspecific sensing, equations (7) and (8). The behavior of the EC (B cell) fraction over the explored proliferation rate parameter space was examined for three distinct combinations of specific and nonspecific conditions, B_{Sp}-C_{Sp}, B_{Nsp}-C_{Sp}, and B_{Nsp}-C_{Nsp} (**Fig. 7D-F**), just as explored in cell motility. Adding specific and non-specific adhesions to varying proliferation rates was qualitatively similar to those obtained from varying motility, although with stronger affects. When both cells display specific sensing, the zone of co-emergence, defined as the area between 0.3 to 0.7 EC fraction, is again blurred and broadened (**Fig. 7D**) compared to the unconstrained control (**Fig. 4A**). Additionally, when one cell type displays nonspecific sensing and the other displays specific sensing, the line

of co-emergence curves towards the nonspecific sensing cell type (**Fig. 7E**). Lastly, when both cell types display nonspecific sensing and proliferation is similarly slowed down, the contour lines straighten (**Fig. 7F**). These trends can also be seen in the cell asymmetry plots (**Appendix Fig. S6D-F**).

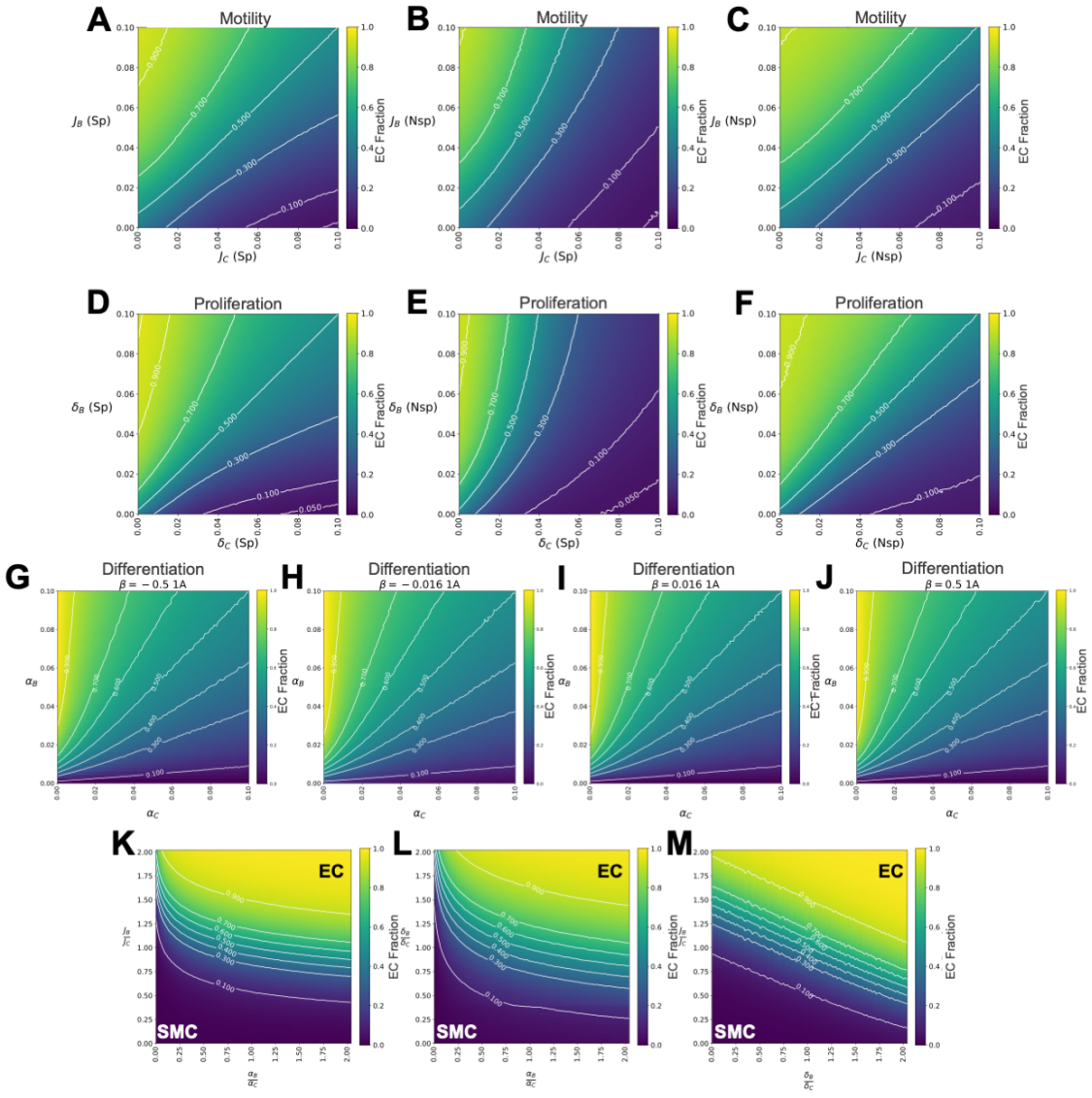

Figure 7. Cell motility, proliferation, and differentiation modified by cell-cell interactions

A-C) Parameter sweeps of motility rates modified under different types of interactions, e.g. specific adhesions (Sp), which applies to cells who can only sense other cells of the same identity, and nonspecific adhesions (Nsp), which describes cells who indiscriminately sense all other cells. Here motility rates are varied while proliferation and differentiation rates are held constant under three EC and SMC sensing combinations: **A)** Specific-Specific **B)** Nonspecific-Specific and **C)** Nonspecific-Nonspecific, respectfully. **D-F)** Similar parameter sweeps were explored for proliferation rates under the same three sensing combinations: **D)** Specific-Specific, **E)** Nonpecific-Specific, and **F)** Nonspecific-Nonspecific. **G-J)** Parameter sweeps of differentiation rates modified by different paracrine signaling (see Appendix Fig. S3), while motility and proliferation rates were held constant. A total of 16 combinations were explored under four different β values (β = -0.05, -0.016, 0.016, and 0.05). Displayed here is the 1A combination (corresponding

to the differentiation of ECs and SMCs influenced by the presence of the surrounding ECs) for all four β values **G)** β = -0.05, **H)** β = -0.016, **I)** β = 0.016, and **J)** β = 0.05. **K)** EC fractions for relative ratios of motility (J_B/J_C) and differentiation (α_B/α_C). Here the motility of SMCs (J_C) is set to displacements of 14 μm over a hr, while EC motility (J_B) is varied between no motion and twice the SMC motility. For differentiation, SMC differentiation (α_C) is set at one cell differentiating every 62.5 hrs and EC differentiation (α_B) is varied between cells differentiating at twice the rate to cells that never differentiate. **L)** Phase diagram for relative ratios of proliferation (δ_B/δ_C) and differentiation (α_B/α_C). Here SMC proliferation (δ_C) is set equal a cell dividing every 40 hrs, and ECs proliferation is varied between no cell divisions to twice the rate of SMCs. **M)** Phase diagram for ratios of motility and proliferation. Motility and proliferation ratios are the same as mentioned prior.

2.3.7. Cell Differentiation with Adjacent Cell Signaling

Lastly, we looked at how the patterning depends on cell differentiation rates, α_θ, that are affected by the signaling from neighboring cells, i.e., paracrine signaling. Our model incorporates both same cell-directed differentiation and alternate cell-directed differentiation (see equation (9) and **Fig. 2E**). This was implemented by the sensing combination and the degree of amplification or suppression, from the magnitude and sign of the β variable constant (**Appendix Fig. S3**). We explored different combinations of paracrine signaling dependence and found that, regardless of the sign and magnitude of β, the EC fraction, over the explored differentiation rate parameter space, was largely unaffected with no significant difference in the formation of micropatterning (**Fig. 7G-J**). For full results see **Appendix Fig. S7** and corresponding asymmetry plots (**Appendix Fig. S8**)

2.3.8. Relative Sensitivity to Different Parameters

To compare the relative influence of motility, proliferation, and differentiation on micropattern formation, we explored the EC (B cell) fraction as a function of physiologically relevant ratios of these rates between the different cell types (**Fig. 7K-M**). First, we explored the EC fraction of the relative motility, J_B/J_C, as a function of relative differentiation rates, α_B/α_C (**Fig. 7K**). Here we see that for physiologically relevant and comparable scenarios, ratios between 0.5 to 2, the range for favorable motility-driven micropatterning, EC fractions between 0.3 to 0.7, was comparatively narrower compared to the relative differentiation ratios. As visualized by the EC fraction contours which run approximately horizontal to the ratios of differentiation rates, x-axis, thus indicating that is the emergence of micropatterns is much more sensitive to the ratios of motility rates. Similar results are obtained when examining proliferation, δ_B/δ_C, versus differentiation (**Fig. 7L**), with the EC fractions dependent on the proliferation more significantly than differentiation. Lastly, looking at the relative effects of ratios of motility and ratios of proliferation rates for ECs and SMCs (**Fig. 7M**) reveals equivalent sensitivity to relative changes in both motility and proliferation rates (**Appendix Fig. S9**). The slopes of the EC fraction contour lines are just around ~0.5 indicating a slightly higher sensitivity to the migration rates as compared to the proliferation rates.

2.4. Discussion

Here, we presented an on-lattice stochastic population-based model that qualitatively reproduces the observed 2D micropatterns that emerge during the co-differentiation of ECs and SMCs from VPCs. Our model enables the spatial visualization of this dynamic system over time, and the examination of effects that various biological processes have on cellular micropattern development. Specifically, our computational model explored the roles that cell motility, proliferation, and differentiation, as well as contact inhibition and adjacent cell paracrine signaling have on pattern formation.

Our main finding is that cell motility and proliferation are the key factors driving 2D micropattern formation. While VPC differentiation into ECs and SMCs is required, it does not appear to drive the pattern formation. Furthermore, this finding supports a pattern assembly mechanism for the emergence of micropatterns. This finding is consistent with literature demonstrating that motility(143) and proliferation(79) can similarly drive pattern formation. Of interest here, is that these two biological processes are also the two main driving forces behind wound healing(76,144), during which, proper organization and patterning of multi-cellular tissues must be executed flawlessly. Furthermore, while some stem cell populations are present in this system, within the skin's stem cell niche (1), their role is mainly to supply differentiated cells that will migrate into the wound and proliferate.

The emergence of distinct micropatterns is also achieved over a broad region of parameter space with EC fractions between 0.30 - 0.70, termed the "*zone co-emergence*". Coupled with our finding that the inclusion of neighbor cell sensing mechanisms impacts the shape of the zone of co-emerges, this proved to be a strong predictor for the development of micropatterns that may be application to other biological systems with implications in directing in-vitro 3D organ morphogenesis.

While cell proliferation and migration rates are the primary driving forces that enable micropatterning, the specific rates and the presence of contact inhibition predict the degree of micropattern development and the length scales of the patterns. Our work on single cluster growth dynamics suggests that the cluster sizes are set by how far the inner core regions, containing high cell densities, can expand and occupy space before being outcompeted by the other cell type. While contact inhibition mitigation of migration and proliferation rates can become important, fewer differences are observed between homotypic and nonspecific sensing mechanisms at low migration and proliferation rates. As rates increase, we see a broad and symmetrical expansion of conditions enabling micropattern development. This is true when ECs and SMCs are both sensing homotypically and nonspecifically. However, when one cell type is sensing homotypically and the other is sensing nonspecifically, there is a reduction in the range of conditions that enable micropattern development accompanied by a significant increase in the

distinctness of patterning. This suggests that sensing can help increase the robustness of patterning.

A limitation of our model is the lack of single cell details, such as cell shape and polarity, which are important when modeling directional propulsion and cell-to-cell adhesions (145,146). This level of single cell modeling, at high resolutions, would be excessive for our population-based questions. However, our modeling framework does allow for the modification of our lattice site dimensions, which serves to increase or decrease the overall resolution of our system, within reason, by directly affecting the number of cells that can inhabit a single lattice site. Our modeling framework could also be applicable to study the development of other cells or tissues like the emergence of keratinocytes during differentiation, wound healing, or normal skin repair (147) or the precise staggered patterning of R8 photoreceptor precursors with accessory cells in the neural epithelium of the eyes(148).

2.5. Conclusion

We have explored a range of motility, proliferation, and differentiation values to assess the impact each has on the emergence of multicellular micropatterns within developing vascular tissue. Our work strongly suggests that, even in the absence of any specific mechanisms that drive segregation, like chemotaxis, micropatterning can emerge as long as cellular factions are maintained within 0.30 – 0.70. These results suggest that even though micropatterning can occur in the absence of sensing, the presence of such mechanisms greatly increases the robustness of patterning, which could be critical to fidelity in tissue development in the naturally noisy and heterogeneous *in vivo* setting.

Chapter 3: Ideal Stiffness Modules Facilitates Vascular-like Networks Emergence from HUVEC Cultures

Abstract

Within the *in vivo* microenvironment, cells are not only interacting with other cells, but also with their surrounding microenvironment by directly sensing the materials mechanical proprieties. This *sensing* of the material's mechanical properties grants cells the ability to adapt to and regulate their behavior in order to promote and/or maintain homeostasis. Additionally, It has been shown that a material's mechanical properties play a crucial role in a cell's function and behavior, but little is known about how the material will impact populations of cells during the emergence of endothelial cell led vascular networks. Here we shed light on this question by using a 2D poly(acrylamide) hydrogel, to explore a wide range of stiffnesses, and two different seeding densities of HUVECs to assess their relative importance during vascular network emergence. We found the initial seeding density of HUVEC had big impact on the timescale by which ECs would self-organized into networks. Additionally, we found that HUVECs do indeed have a preferred stiffness, where they exhibited the greatest degree of network self-assembly, here found to be 4.5kPa. This work suggesting the existence of a delicate balance between stiffness and cell density, whereby the stiffness has to be just right to allow cell spreading and cell migration but where the presence of excess cells will lead to clustered groups of HUVECs instead of chain-like networks.

3.1. Introduction

Single cells and populations of cells are constantly sensing and responding to changes in their local microenvironment as a way of promoting homeostasis. This can take many forms such as sensing chemical signals(149,150) or gradients(151), interacting with other cells via direct cell-cell communication(152), and/or by physically sensing their surrounding material's mechanical properties, such as the substrate's stiffness, porosity, and/or external sheer stress forces(153). Here, the process by which cells can *sense* a material's mechanical properties and convert them into biological signals for a targeted response (such as migrating, proliferating, undergoing apoptosis, and/or differentiating(47–50)) is known as mechanotransduction. One of the most well researched mechanotransduction *systems* is the ECM-integrin interaction, which is initiated by the adhesion of the integrin to the underlying substrate.

Integrin mediated mechanotransduction, is initiated by the activation of integrin surface binding proteins which, once bound, can lead to changes in a cell's morphology, migration, and function(52,58). Integrins are uniquely specialized surface proteins that are able to bind to specific ECM proteins initiating the formation of local cell-matrix adhesions, known as focal contacts, that are unique to the adhering cell types(52). Furthermore, by direct manipulation of the substrate's matrix composition and concentration, researchers are able to directly change the materials stiffness (measured by the materials Young's Modulus), porosity, and topology leading to specific mechano-driven responses(7,45). Many natural and synthetic materials have been used to recreate specific 2D niche conditions, these ECM/hydrogels include agarose(154), alginate(155), chitosan(156,157), chondroitin sulfate(158), collagen(159), fibrin(14,160), fibronectin(161), hyaluronic acid(162), Matrigel(163), and silk(164). Additionally, one of the most common and arguably popular hydrogels used to date is poly(acrylamide) (PAA), consisting of crosslinked acrylamide and bis-acrylamide monomers, and whereby the manipulation of its relative concentrations changes the hydrogels elastic properties. Additionally, PAA's popularity also arises from its broad range of achievable stiffnesses (0.1kPa – 200kPa) which encompasses most of the native *in vivo* tissue stiffnesses(65,165). Lastly, PAA's accurate control of its stiffness profile is critical when developing substrates that will induce a desired responses(6), such as driving specific cell linage commitment in stem cells(7) or vascular network development in ECs(163).

Here, we set out to explore and understand the impact that substrate stiffness and cellular densities have on the self-assembly of 2D endothelial cell driven vascular-like network formation. This was explored by seeding different densities of HUVECs ($8x10^3$ cells/cm^2 and $2x10^4$ cells/cm^2) on PAA hydrogels of various Young's Modulus (200Pa, 1.1kPa, 4.5kPa, 10kPa, and 100kPa). We found that 2D vascular-like networks, defined here as chains of connected ECs, would readily form on 4.5kPa PAA hydrogels. Unsurprisingly, this stiffness also happens to fall within the stiffness range of *in vivo* vessel walls, with a Young's modulus between 1.4kPa – 12kPa(166). Furthermore, we found that

in addition to stiffness, the emergence of networks was also dependent on the initial cell seeding density, suggesting a delicate balance between stiffness and cell-to-cell interactions during the self-arrangement of developing vascular networks.

3.2. Methods

3.2.1. Cell Culture

Green florescent protein (GFP) expressing-human umbilical vein endothelial cells (HUVECs) (Angio-Proteomie) were expanded on 10μg/mL fibronectin-coated plates and supplemented with Endothelial Cell Growth Medium-2 with BulletKit (EGM-2, Lonza). Cells used were between passages 3-12. Medium changes were performed every other day, and cells cultures were split upon reaching ~80% confluency.

3.2.2. Polyacrylamide (PAA) Fabrication:

PAA hydrogels were fabricated similarly to previously published protocols(65). Breifly, hydrogels with a relative stiffnesses (Young's Modulus or Elastic Modulus, E) of 200Pa, 1.1kPa, 4.5kPa, 10kPa, and 100kPa were fabricated by mixing acrylamide from 40% stock solution (Sigma, A4058) with bis-acrylamide from 2% stock solution (Sigma, M1533) in phosphate buffer saline (PBS), see **Table 1**. Air bubbles introduced during mixing were removed by vacuum gas-purge desiccation for 30min. The mixture was then mixed with 10% ammonium persulfate (APS) (Sigma, A3426) and tetramethylethylenediamine (TEMED) (Sigma, T7024) at a 1:100 and 1:1000 ratios, respectfully, initiating PAA polymerization. The PAA mixture was then sandwiched between an 18mm glass coverslip (Fisher) and a hydrophobically-treated, dichlorodimethylsilane (Sigma, 440272)-coated glass slide. After 30min of polymerization, the 18mm glass slide, containing the bound PAA hydrogel, was carefully removed from the hydrophobic slide. Lastly, PAA hydrogels were functionalized by two consecutive treatments of 0.2mg/mL sufosuccinimidyl-6-(4'-azido-2'-nitrophenylamino)-hexanoate (Pierce Biotechnology) for 6 minutes each, and thoroughly washed thrice with HEPES buffer and once with PBS. The ECM protein, fibronectin (at 10μg/mL), was then used to coat the hydrogels prior to cell seeding (**Fig. 8**).

Table 2. Poly(acrylamide) hydrogels for various stiffnesses.

Here 200μL of each stiffness of PAA mixture was made for the fabrication of 4 hydrogels. Values were calculated from a previously optimized protocol(65).

Stiffness	40% (w/v) acrylamide	2% (w/v) bis-acrylamide	PBS	APS	TEMED
200 Pa	15 μL	3 μL	170 μL	2 μL	0.2 μL
1.1 kPa	15 μL	10 μL	173 μL	2 μL	0.2 μL
4.5 kPa	25 μL	15 μL	158 μL	2 μL	0.2 μL
10 kPa	50 μL	10 μL	138 μL	2 μL	0.2 μL
100 kPa	40 μL	96 μL	62 μL	2 μL	0.2 μL

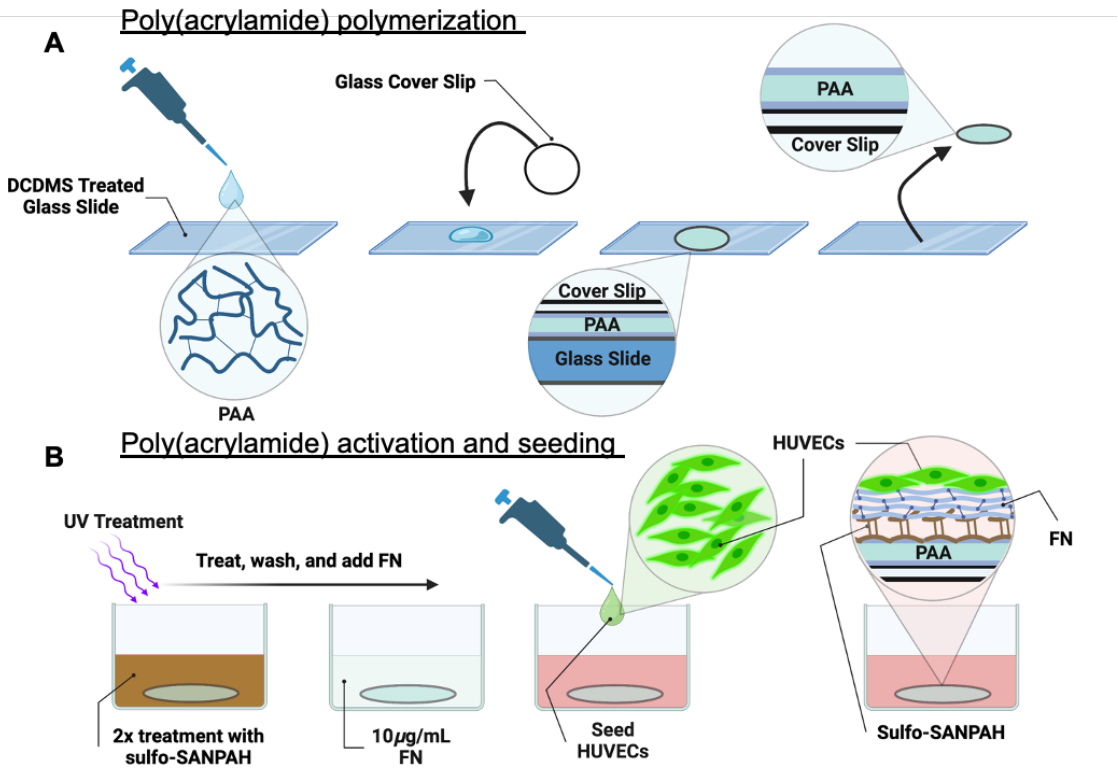

Figure 8. Fabrication of PAA hydrogels
A) Schematic of PAA polymerization and bonding to glass cover slip by sandwiching PAA hydrogel between a hydrophobic (DCDMS treated) glass slide and an etched glass cover slip. **B)** Schematic of PAA activation by sulfo-SANPAH treatment, followed by fibronectin coating and seeding.

3.2.3. Vascular Patterning and Cellular Growth

GFP-HUVECs were seeded on fibronectin-coated PAA hydrogels at a density of $8x10^3$ cells/cm^2 or $2x10^4$ cells/cm^2 and imaged at 1hr, 5hrs, 9hrs and 19hrs with a Nikon Eclipse TE2000-U widefield fluorescent microscope (**Fig. 9A-D**). This time series was used to determine an ideal timescale for network formation and to gauge cellular proliferation. Collected images were all processed using a custom-built image processing macro within FIJI(167). Briefly, images were smoothed using the "Gaussian Blur" function with a sigma value of 4 pixels and followed by the removal of the image's background fluorescence with the "subtract background" function with a rolling ball radius of 300 pixels. The GFP-HUVECs were then isolated using the "Triangle" thresholding function, which returned a binary image displaying the HUVEC driven vascular morphology. Single cells were then isolated using the "Watershed" function and counted with the "Analyze Particles" function.

3.2.4. Image Analysis: Percolation

All images were analyzed in FIJI(167). Briefly, raw (.tif) low magnification (2x) images of GFP-HUVECs were first imported into FIJI and corrected for high fluorescent noise by use

of the "Despeckle" function. Images were then further processed by running "Subtract Background" with a rolling ball radius of 50 pixels, followed by a "Gaussian Blur" with sigma value of 10 pixels (**Fig. 11A-C**). Images were then thresholded as to keep the fluorescent intensity values above 20 and converted into a mask. The mask was then skeletonized and dilated four times preserving the filling fraction (**Fig. 11D-F**). We then calculated a percolation probability by dividing the skeletonized experimental images into 312 smaller non-overlapping images. These smaller images were then processed by a custom Python(132) program that labels all pixels according to their cluster location. Here, if any two pixels have a separation distance, Euclidian distance, greater than the width or height dimensions of the divide image and both pixels belong to the same cluster, then they are considered percolated. The percolation probability is then taken as the average probability taken over all 312 images.

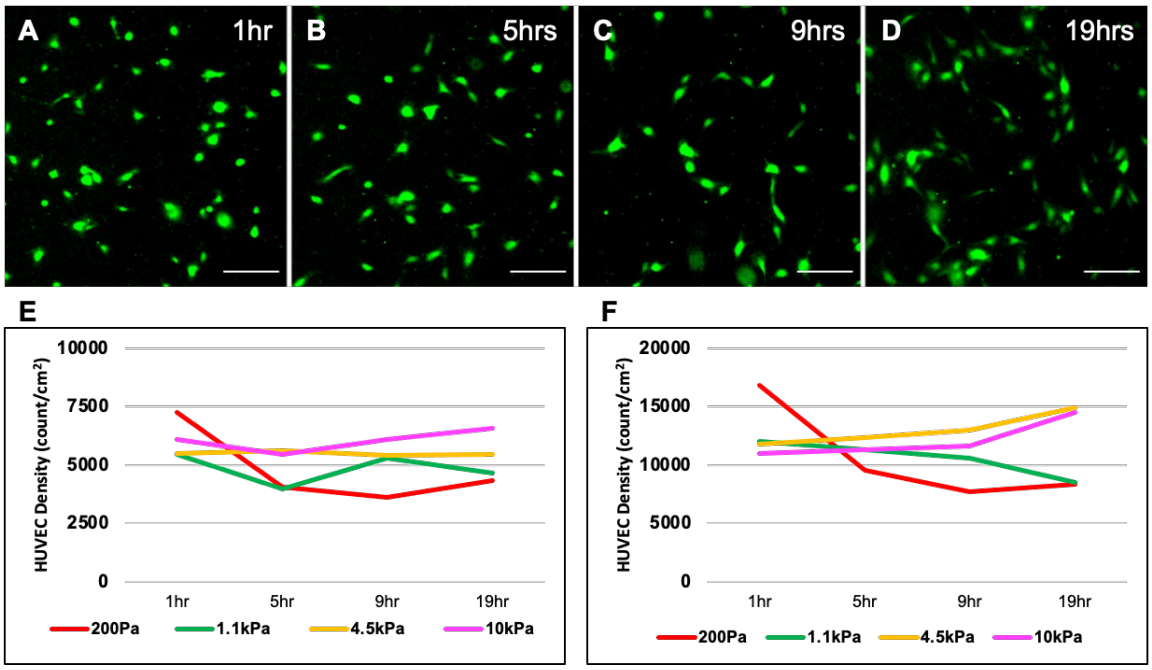

Figure 9 HUVEC densities over time

Shown here are GFP-HUVECs seeded at 8x10^3 cells/cm^2 and imaged at **A)** 1hr, **B)** 5hrs, **C)** 9hrs and **D)** 19hrs. These HUVECs were seeded on 4.5kPa hydrogels coated with 10μg/mL fibronectin. Scale bar is 200μm. Additionally, GFP-HUVECs were also seeded at **E)** 8x10^3 cells/cm^2 and **F)** 2x10^4 cells/cm^2 on hydrogels of various stiffnesses. Specifically, 200Pa, 1.1kPa, 4.5kPa, and 10kPa. Plotted here is their corresponding HUVEC density over time (n=1).

3.2.5. Traction Force Microscopy

GFP-HUVECs were seeded on 10μg/mL fibronectin-coated 1.1kPa PAA hydrogels containing embedded 1μm fluorescent beads (Fisher) at a density of 8k cells/cm^2. At 20 hours post seeding the cells were detached by adding 1X Trypsin (Corning) to the HUVEC cultures, effectively cleaving, and removing the cells from the PAA hydrogel. Simultaneously, a time-lapse of the cell culture was collected at 15s intervals of targeted areas. Reference images were collected before and after the addition of Trypsin and were stacked and corrected for drift with the "Linear Stack Alignment with SIFT" function(168)

in FIJI. Once aligned the images were uploaded into MATLAB(133) where the bead displacements and traction forces were calculated using a previously published Fourier transform traction cytometry algorithm(169).

3.2.6. Statistical Analysis:

Statistical significance was calculated by performing a two tailed Student's T-test with unequal variance. Significance was determined as any p-value < 0.05. Plotted bar graphs are mean values ± standard deviation unless otherwise stated.

3.3. Results

3.3.1. Vascular Network-like Formations are Driven by Stiffness

GFP-HUVECs were seeded onto PAA hydrogels with various Young's modulus (E) that encompass the native stiffness range of the EC basement membrane, between 8 - 35kPa(170), and the aortic wall, between 1.4kPa – 12kPa(166). Specifically, we explored three stiffnesses that fall below the measured basement membrane stiffness range, one within, and one stiffness in the higher range to explore the formation of EC networks. The five stiffness values explored consisted of soft/compliant PAA hydrogels with a stiffness modulus of 200Pa, 1.1kPa, and 4.5kPa; a medium stiffness of 10kPa, and a high stiffness of 100kPa (**Table 2**). HUVECs were additionally seeded at two different seedings densities $8x10^3$ cells/cm^2 and $2x10^4$ cells/cm^2 and were tracked and imaged over the course of 19hrs (**Fig. 9 A-D**). We observed the HUVECs seeded at $8x10^3$ cells/cm^2 to have a relatively unchanging cellular density over the given 19hrs compared to the higher density, of $2x10^4$ cells/cm^2, which showed an increase in its density at increasing stiffnesses (> 4.5kPa) after only 9hrs (**Fig. 9E & F**).

As expected for the lower seeding density ($8x10^3$ cells/cm^2), vascular like networks, defined as chains of connected ECs, were observed to be limited on the softer more compliant stiffnesses at 19hrs post seeding. Specifically, on the lowest stiffness, 200Pa, we observed the HUVECs to mostly be idle and/or exhibit very limited cell spreading and motility. They also tended to remain as single cells (**Fig. 10A**). Increasing the hydrogel stiffness to 1.1kPa resulted in HUVECs that display some signs of cellular spreading, as observed by their increase in cell area and the presence of sharp cellular protrusions, and some cell-to-cell linking (**Fig. 10B**). On the 4.5kPa hydrogels, the HUVECs exhibit the greatest degree of cell spreading and cell-to-cell adhesions, which resemble interconnected 2D EC cords-like networks (**Fig. 10C**). However, HUVECs seeded on a medium stiffness of 10kPa, displayed more colony-like adhesions and fewer cords/networks of cells (**Fig. 10D**). Lastly on the 100kPa hydrogels, the HUVECs displayed the same degree of spreading, colony formation, and cellular protrusions, but very limited cord linking (**Fig. 10E**). Additionally, here we observed the HUVEC density to increase, suggesting an increase in their cellular proliferation rate, with increasing hydrogel stiffness. For example, on the 100kPa hydrogels there was a near 2-fold increase in the

HUVEC cellular density, of 1.6x10^4 cells/cm^2 ± 7.8 x10^3 cells/cm^2, compared to their initial seeding density of 8x10^3 cells/cm^2 (**Fig. 10K**).

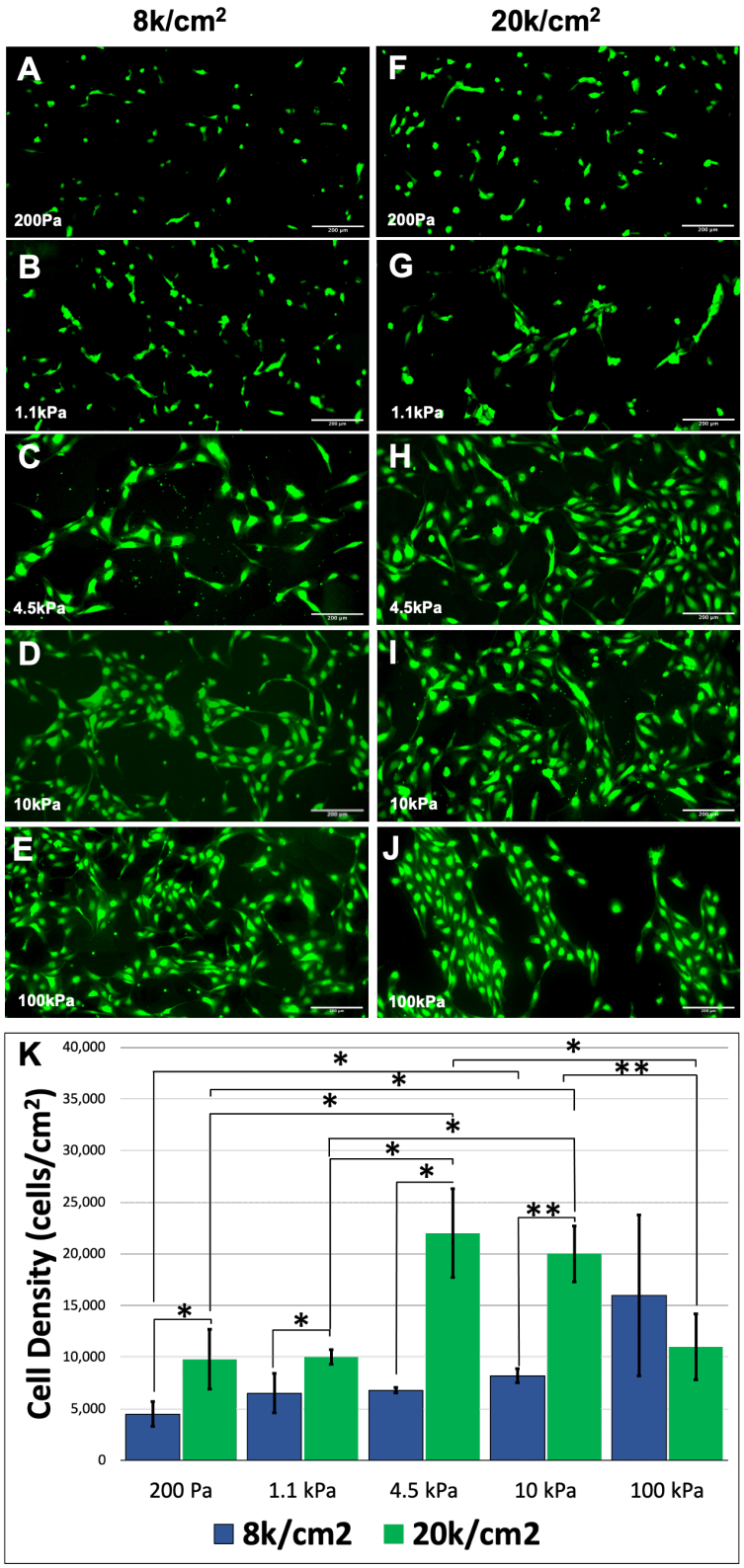

Figure 10. Vascular-like network development on PAA hydrogels. GFP-HUVECs were seeded at two densities **A-E)** 8k/cm^2 and **F-J)** 20k/cm^2 on top of chemically treated poly(acrylamide) hydrogels coated with 10µg/mL of fibronectin of various stiffnesses. Here vascular-like networks were assessed by seeding HUVECs on very soft/compliant hydrogels of **A & F)** 200 Pascals (Pa), **B & G)** soft/compliant hydrogels of 1.1 kPa and **C & H)** 4.5kPa, **D & I)** medium stiffness hydrogels of 10 kPa, and **E & J)** high stiffness hydrogels of 100 kPa. **K)** Cellular densities were then quantified and plotted at 19hrs post seeding. Here error bars represent the standard deviation and significance is denoted by * for p-value less than 0.05 and ** for p-values < 0.01. data represent an n = 3.

Similar results were observed with HUVEC seeded at $2x10^4$ cells/cm^2 compared to those seeded at $8x10^3$ cells/cm^2. Including the lack of cell spreading or cord/network formations on the most compliant stiffness, of 200Pa (**Fig. 10F**), and minimal cord linking on the 1.1kPa hydrogels (**Fig. 10G**). On the 4.5kPa and 10kPa hydrogels the cellular HUVEC density was measured to be nearly doubled that of the softer hydrogels, with a density of $2.2x10^4 \pm 4.3x10^3$ cell/cm^2 and $2x10^4 \pm 2.7x10^3$ cells/cm^2 for 4.5kPa and 10kPa hydrogels, respectfully, compared to $9.8\ x10^3 \pm 2.9x10^3$ cell/cm^2 and $10^4 \pm 700$ cell/cm^2 for the more compliant hydrogels of 200Pa and 1.1kPa, accordingly. This coupled with an apparent increase in cell spread led to the formation of HUVEC colonies and not cord-like network development (**Fig. 10H & I**). Lastly, HUVECs seeded on 100kPa PAA hydrogels displayed high degrees of cellular spreading, but very limited cord-like structures (**Fig. 10J**). Interestingly, the cellular density of HUVECs was observed to decrease to $1.1x10^4 \pm 3.2\ x10^3$ cell/cm^2 on the stiffest, 100kPa, PAA hydrogels (**Fig. 10K**).

3.3.2. Percolation Probability Suggests the Ideal Stiffness for Development of 2D Network-like Formation

We then set out to quantify the degree of connectedness for HUVECs cultured on various stiffnesses. For this we calculated a percolation probability, defined here as an order parameter which quantifies the ability of a continuous connected network to span the given available space. A mean percolation probability was calculated for all our experimental images by first processing the images as to only emphasize the cellular connections **(Fig. 11A-C)**, and then by skeletonizing these connected cells as to focus on only the connected networks (**Fig. 11D-F**). The skeletonized Images were then divided into 312 smaller non-overlapping images, as to extract meaningful statistics. Next, we computed the mean percolation probability by taking the mean probability over all 312 images. Here an image is *percolating* or has a 100% percolation probability, $P_{\%}=1$, if there exist a continues network whose length is larger than the image dimensions, or not percolated with a percolation probability of 0%, $P_{\%}=0$, if there are no networks or if the network's length is less than the image dimensions. We found that for both the lowest seeding density ($8x10^3$ cells/cm^2), sampled at long times (**Fig. 11G**), and for the highest seeding density, sampled at short times (9hrs) (**Fig. 11H**), since there is a noticeable increase in cellular densities at later times (**Fig. 9F**), show a peak in their percolation probability at the 4.5kPa stiffness (**Fig. 11G-H**). These experiments suggests that network formation is driven by substrate-mediated elastic interactions and that these interactions are stronger on stiffnesses that fall within the stiffness range of the native tissue, between 1.4kPa – 12kPa(166).

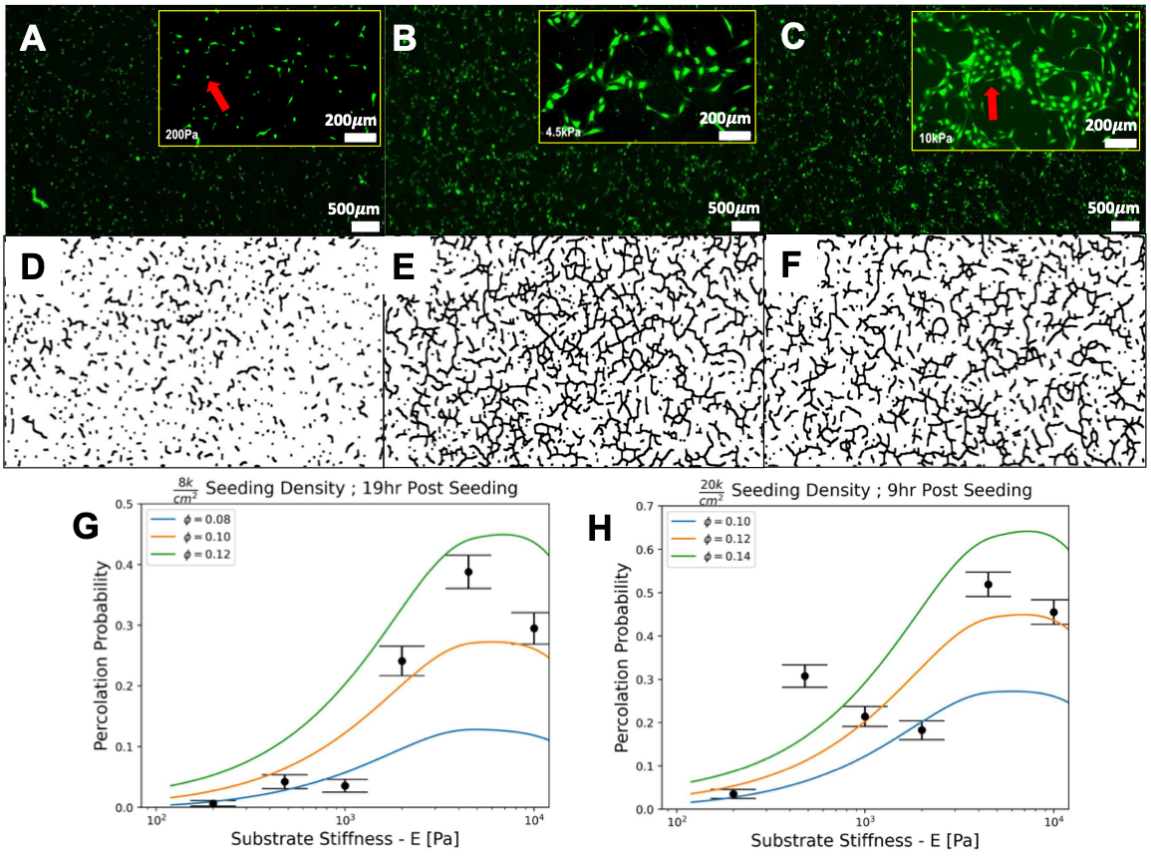

Figure 11 Analysis of connected clusters of endothelial cells cultured on various elastic substrates reveals optimal stiffness for cell network formation

Experimental images of HUVECs at 8×10³/cm² seeding density 19 hours post seeding on polyacrylamide substrates of varying stiffness: **A)** 200Pa, **B)** 4.5kPa, and **C)** 10kPa. Insets show 10× magnified images of the full field of view. Cells on substrates of lower stiffness tend to remain as isolated single cells (shown by red arrow in **A**), and do not form inter-cellular connections. Cells on substrates of higher stiffness tend to spread out and aggregate into dense clusters (shown by the red arrow in **C)**. Processed binary skeletonized images for HUVECs seeded on **D)** 200Pa, **E)** 4.5kPa, and **F)** 10kPa. **G-H)** Quantitative measurement of the percolation probability from experimental images at two different initial cell seeding densities **G)** 8×10³/cm² and **H)** 2×10⁴/cm². Experimental data is shown as black points with error bars representing the standard error from the mean. The continuous curves represent computational model predictions for percolation as a function of substrate stiffness at three different representative values of the simulated density (ϕ). model not reported here, please see Noerr et al., PNAS, 2023 (171).

3.3.3. Cell-generated Forces: Traction Force Microscopy

We then set out to quanitfy the traction forces that ECs produce as single cells (**Fig. 12A** white box), pairs of cells (**Fig. 12A** Yellow box), and as connected cord-like networks (**Fig. 12A** red box). For this, we seeded HUVECs on a 1.1kPa hydrogel at 8x10^3 cells/cm^2 and selected a target location for analysis that would contain regains where single HUVECs were present (**Fig. 12B & C**) and clustered groups of HUVECs (**Fig. 12D & E**). Moreover, within the cluster of HUVECs, we analyzed a pair of adherent cells (**Fig. 12F**) and a group of cord-like linked HUVECs composed of six cells (**Fig. 12A** red box, **Fig. 12G**).

We then performed traction force microscopy measurements, at 20hrs post seeding, by capturing the displacement of embedded 1μm red-fluorescent beads as the PAA hydrogel is relaxed by the release of tension from adhered HUVECs upon the addition of 1x-trypsin. We then input our constrained (prior to addition of trypsin) and relaxed PAA (post addition of trypsin) images into a publish MATLAB TFM algorithm (169) to calculate our exact bead displacements and traction fields. We found that single HUVECs tended to display a dipolar adhesion on the hydrogel/ECM, as shown by the adhesion locations and directionality of the bead displacement (**Fig. 12B**). Here we measured the greatest bead displacement to be ~0.6μm corresponding to a maximum traction force of ~40Pa (at the core of their adhesive center) (**Fig. 12C**). For the pair of cells, we noticed a similar dipolar bead displacement and traction fields (**Fig. 12D & E** yellow box), again indicated by the opposite directionality of the displacement and traction fields. Here, the traction fields were measured to peaked at values close to ~20Pa (**Fig. 12E**). Interestingly, despite being two connected cells, they only exerted traction forces along their direction of alignment (**Fig. 12F**). Lastly, for the cord-like linked HUVECs (**Fig. 12A** red box), we again see a dipolar adhesion across the chain of HUVECs, but with various adhesion points, one major and two minor (**Fig. 11G**). Here, we measured the greatest bead displacement to be 2.2μm and generating the greatest traction forces, maxing out at 61Pa.

3.4. Discussion

In vivo, cells are in constant contact with their surrounding microenvironment, including other cells and the surrounding extracellular matrix proteins, resulting in a dynamic state where cells are able to readily *sense* and respond to changes in their microenvironment as a way to actively promote homeostasis. Moreover, while it is well established that cells can sense other nearby cells by cell-cell adhesion molecules (such as cadherins(51), integrins(52), selectins(53), claudins(54), and connexins(55)), it has only been recently that the importance of stiffness has become a relevant parameter. Specifically, cell integrin-matrix binding which allows cells to directly *sense* their environmental conditions (52,56). In recent years, this growing body of research has advocated for the use of hydrogels with specific stiffnesses, as an additional parameter, for inducing targeted responses from cells, such as driving cell migration, proliferation, morphogenesis, apoptosis, and/or differentiation(47–50).

In some stem cell (SC) studies, it has been shown that SC will readily differentiate into cells/tissues that closely match the underlying substrate's stiffness(7,9). For example, when driving vascular cell differentiation, stiffness was found to regulate the fate commitment of ECs or SMCs. Specifically, vascular progenitor cells were shown to be sensitive to small changes in stiffnesses, and were able to discriminate between relative low (3kPa) and high (8kPa) stiffnesses when differentiating into ECs or SMCs, respectfully(9,45). In another study, Wong et. al, showed that an inverse differential potential emerged when culturing vascular progenitor cells on similarly compliant (10kPa)

vs stiff (40kPa) polyacrylamide hydrogels(45). With ECs preferentially differentiated on the softer more compliant hydrogels compared to the stiffer substrate(45).

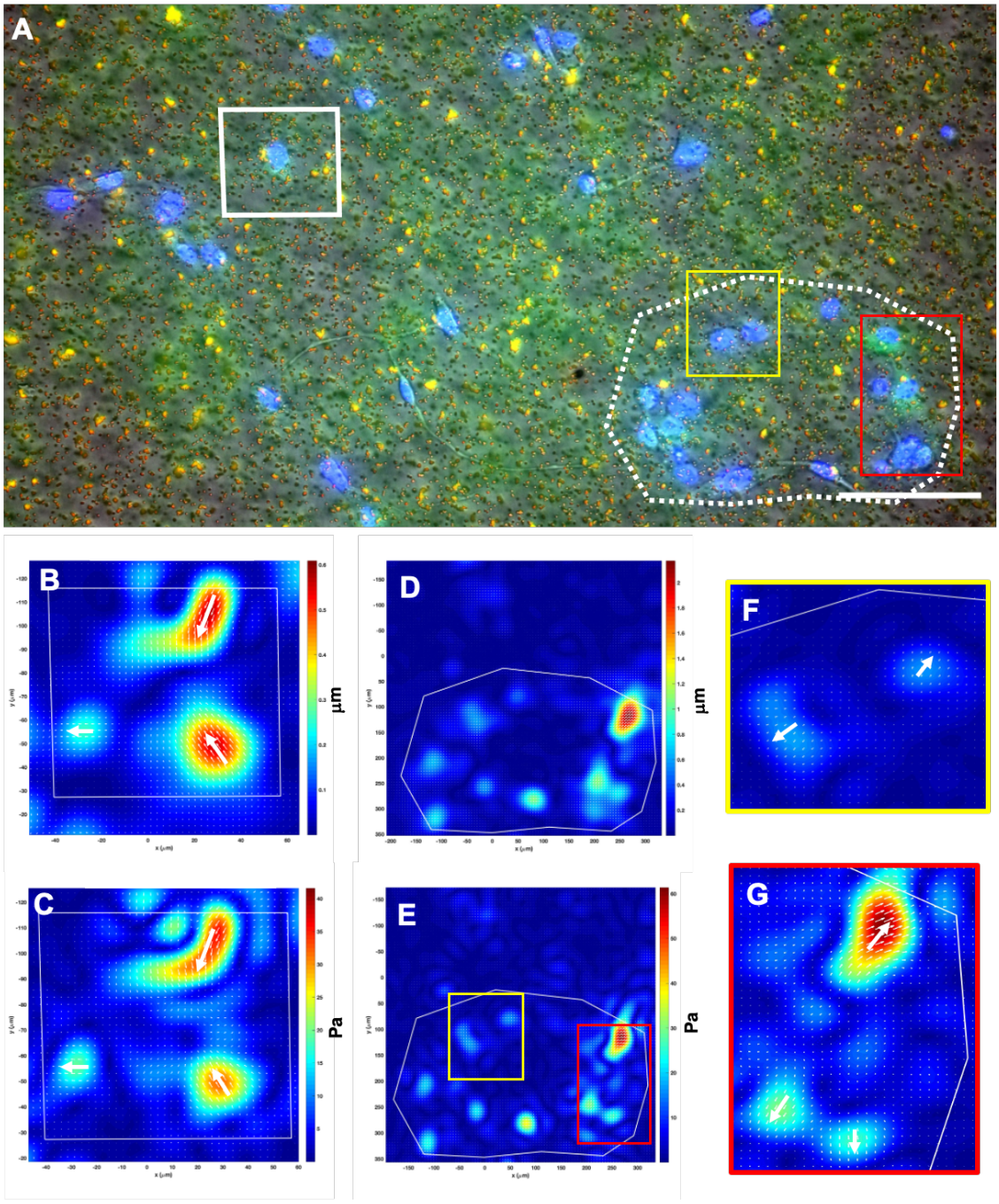

Figure 12. Traction forces of vascular-like networks formed on a 1.1kPa PAA hydrogel

Merged image of HUVECs (brightfield) seeded on a 1.1kPa stiffness PAA hydrogel containing embedded 1µm diameter red-fluorescent beads, and counterstained with DAPI (blue). **B)** Displacement field produced by the embedded red beads upon cellular release of a single cell, outlined in the white box, after addition of 1x trypsin, and **C)** its corresponding traction field; units are in Pa (N/area). **D)** The displacement field for a vascular-like network, outlined by the dotted white line, and **E)** its corresponding traction field. **F)** Zoomed in traction fields for a pair of cells, and **G)** zoomed in traction field for a multi-cell vascular-like network.

Furthermore, it was found that inhibition of the $\alpha v\beta 1$ integrin would reverse these mechano-responsive results, supporting the argument of a stiffness-mediated potential for vascular cell differentiation and other cellular behaviors. Likewise, in a study by Rüdiger et. al., it was showed that EC driven vascular network formation was highly dependent on the ECM composition and the substrate's stiffness modulus, with ECs constantly modifying their surrounding ECM leading to the development of unique strain fields that function as durotactic tracks which other ECs could utilize for the self-assemble into vascular networks(163). Interestingly, it was also shown that networks would fail to emerge on stiffer substrates. This seems to suggest a limit to the strain force ECs can generate, while simultaneously implying the existence of an ideal, or *Goldilocks,* stiffness range where vascular networks would readily emerge. However, the exact stiffness range has been illusive since the exact stiffness of native blood vessels is not well-characterized as it is highly dependent on the type/location of the vessel and the method of measurement(163,171). This further highlights the need for understanding the matrix/substrate stiffness in *in vitro* cell cultures for exact recapitulation of specific cell niches.

Here we shed some light on what drives the emergence of 2D vascular-like networks and explored the relative importance of cell-cell adhesion and cell-substrate adhesions by varying both the seeding density of HUVECs and the underlying PAA hydrogel's stiffnesses. We found that HUVECs do indeed have a preferred stiffness where they exhibited the greatest degree of network self-assembly, found here to be at 4.5kPa (**Fig. 11G**). While minimal network emergence was observed on both lower (200Pa and 1.1kPa) and higher stiffnesses (>10kPa) (**Fig. 10A-E**). While we were able to collect some traction force data (on 1.1kPa hydrogels), the picture is still incomplete, and more time should be dedicated to measuring the traction forces being generated across the explored stiffness range. We hypothesis the existence of peak traction forces on cells seeded on 4.5kPa PAA hydrogels compared to both lower and higher stiffnesses. Furthermore, we found the seeding density to also play an important role in facilitating the formation of networks. Interestingly, we found that a lower seeding density of $8x10^3$ cells/cm^2 of HUVECs would not exhibit any significant change to their density over the measured 19hrs, unlike the higher density cultures, $2x10^4$ cells/cm^2, which would start to show signs of proliferation after only 9hrs in culture (**Fig. 9E-F**). Given this we decided to analyze these HUVEC cultures at 9hrs, which was prior to the observed cellular proliferation, and again saw a higher degree of network development on the 4.5kPa PAA hydrogels (**Fig. 11H**). This was surprising and seems to suggest that cellular densities do indeed play a critical role in ECs self-assemble by directly regulating the timescale of ECs self-assemble into lines, cords, or clusters. To validate this, one could simply observe the lower density cultures at a much later time point and see how proliferation has impacted the structure of these vascular-like networks. A direct comparison of these two cultures at different time points could more closely explore the delicate balance between stiffness and cell density.

3.5. Conclusions

We have explored two different seeding densities and a wide range of PAA stiffnesses in order to assess the relative importance of vascular cord-like network emergence from HUVECs cultures. We found that the initial HUVEC density cannot be too high, or the network driving forces will be outperformed by the HUVEC's proliferation rates, leading to cluster formation rather than networks. Additionally, we found that HUVECs do indeed have a preferred stiffness, where they exhibited the greatest degree of network self-assembly, here found to be 4.5kPa. This suggests the presence of a delicate balance between stiffness and cell density, whereby the stiffness and cell density must be precise to allow cell spreading and motility. The presence of excess cells will lead to greater EC driven strains, resulting in clustered groups of HUVECs instead of chain-like networks.

Chapter 4: Mural Cells Aid in Microvasculature Assembly and Stabilization

Abstract

Microfluidic devices and organ-on-a-chip models are becoming increasingly attractive platforms for studying three-dimensional human tissues that more closely mimic physiological dimensions and timescale. These devices, which allow for the incorporation of height, enable the 3D spatial organization of multicellular cultures as well as real-time visualization. These platforms have already greatly benefited the field of vascular biology, which aims to direct vessel network assembly *in vitro*, by showing the potential in generating vascular networks, however issues with long-term stability and perfusability still remained a challenge. Here, we hypothesize that the use of mural cells, specifically smooth muscle cells and pericytes, may play a significant role in increasing the stability of emerging microvascular networks by more closely mimicking the arterial phenotype. Here we set out to examine the role that mural cells play in vascular assembly, vascular morphology, and long-term stability of *in vitro* microvascular networks. For this we collected images of developing vascular networks from human umbilical vein endothelial cells co-cultured with either normal human lung fibroblasts, human aortic smooth muscle cells, and pericytes alone or with both mural cells, and found that the inclusion of both mural cell types led to the formation of smaller vessel diameters (<30μm), less total area coverage, greater vascular branching, and lower network tortuosity by day 7, compared to the other conditions. Additionally, this tri-culture condition remained intact and functional for more than two months, while the other conditions would disassemble by days 10-14. These findings contribute to the growing advancements in tissue and organ development by providing a reliable method for developing fully vascularized tissues that are stable for extended timescales.

4.1. Introduction

Cardiovascular diseases (CVDs) are the number one cause of death worldwide. In the United States alone, it is estimated that an astonishing 950,000 people died from CVDs complications in the year 2020(172). Such complications include coronary heart disease, stroke, atherosclerosis, deep vein thrombosis, aneurysms, etc. This total accounts for twice the number of deaths associated with cancer and twenty-five times the amount due to AIDS-related complications. While it is important to study CVDs a more sensible approach would be to investigate preventative solutions to these diseases before they become too severe. For this we must first have a robust understanding of blood vessel development, known as vasculogenesis, and new vessel development from preexisting networks, known as angiogenesis.

Generally speaking, blood vessels are highly branched multi-scale dynamic structures that form during development and continue to grow and remodel throughout adulthood (**Fig. 13**). Vascular formation and remodeling may occur by distinct mechanisms including vasculogenesis, angiogenesis, arteriogenesis, or pruning. Specifically, vasculogenesis is the process by which individual endothelial cells (ECs) self-assemble and organize into branched networks of interconnected tubules. Angiogenesis is initiated by a signal, like vascular endothelial growth factors (VEGFs), angiopoietins (ANGs), platelet-derived growth factors (PDGFs), ,(173–175), and involves ECs sprouting from preexisting blood vessels to form new luminized branches. Arteriogenesis is defined as an increase in the diameter of an existing vessels often occurring after two independent vessels have merged, anastomosis, and lastly vascular pruning is the regression of selected vascular branches. Together, these mechanisms contribute to blood vessel dynamics and remodeling within tissues. The tight regulation of blood vessel density, arguably, makes blood vessel networks among the most actively regulated tissues within our bodies with any abnormalities, such as blockages or leakages, often leading to improper flow and cellular death(176).

In order to study these highly complex behaviors we must first move away from two-dimensional (2D) tissue cultures and explore vessel formation in three-dimensions (3D) that recapitulate the physiological microenvironment. Fortunately, microfluidic devices and organ-on-a-chip models, have become good solutions for studying cell organization by closely mimicking physiologically relevant lengths and time-scales(92) with multicellular systems matching the dimensions, stiffness, and elastic properties of tissue, and are proving to be extremely useful for new drug discovery(90,91). These devices have been explored by several groups to generate perfusable microvasculature (177), with some of the earliest perfusable vasculature being generated from cultures containing human umbilical vein endothelial cells (HUVECs) with normal human lung fibroblasts (NHLFs) (14) or mesenchymal stem cells (MSCs) (178). More recent systems utilize pericytes(117) to generate smaller diameter vasculature that resemble capillary networks, with diameters less than 10μm. However, no one group has yet directly

compared the distinct roles that fibroblasts, and mural cells, including pericytes (PCs) and smooth muscle cells (SMCs), have on the emergence of vascular networks, their stability, perfusability, and overall health of these engineered micro-vessels.

Here, we set out to explore the distinct role that mural cells play in vascular assembly and long-term stability by using a simple three-channel microfluidic device. We found that ECs, specifically HUVECs, cultured within a 3mg/mL fibrin gel with both human aortic smooth muscle cells (HuAoSMCs) and human brain microvascular pericytes (HBM-PCs), as accessory cells, will produce smaller-diameter vascular networks (~30μm) that remain stable for over 2 months, compared to conditions where ECs are seeded alone with either SMCs, PCs, or fibroblasts. Furthermore, we observed that after 21 days of continuous stable vasculature, the vessels began exhibiting new angiogenic activity. To our knowledge, this is the first example of perfusable microvasculature assembled *in vitro* that 1) remained viable over 1 month and 2) exhibited new growth following 21 days of continuous culture.

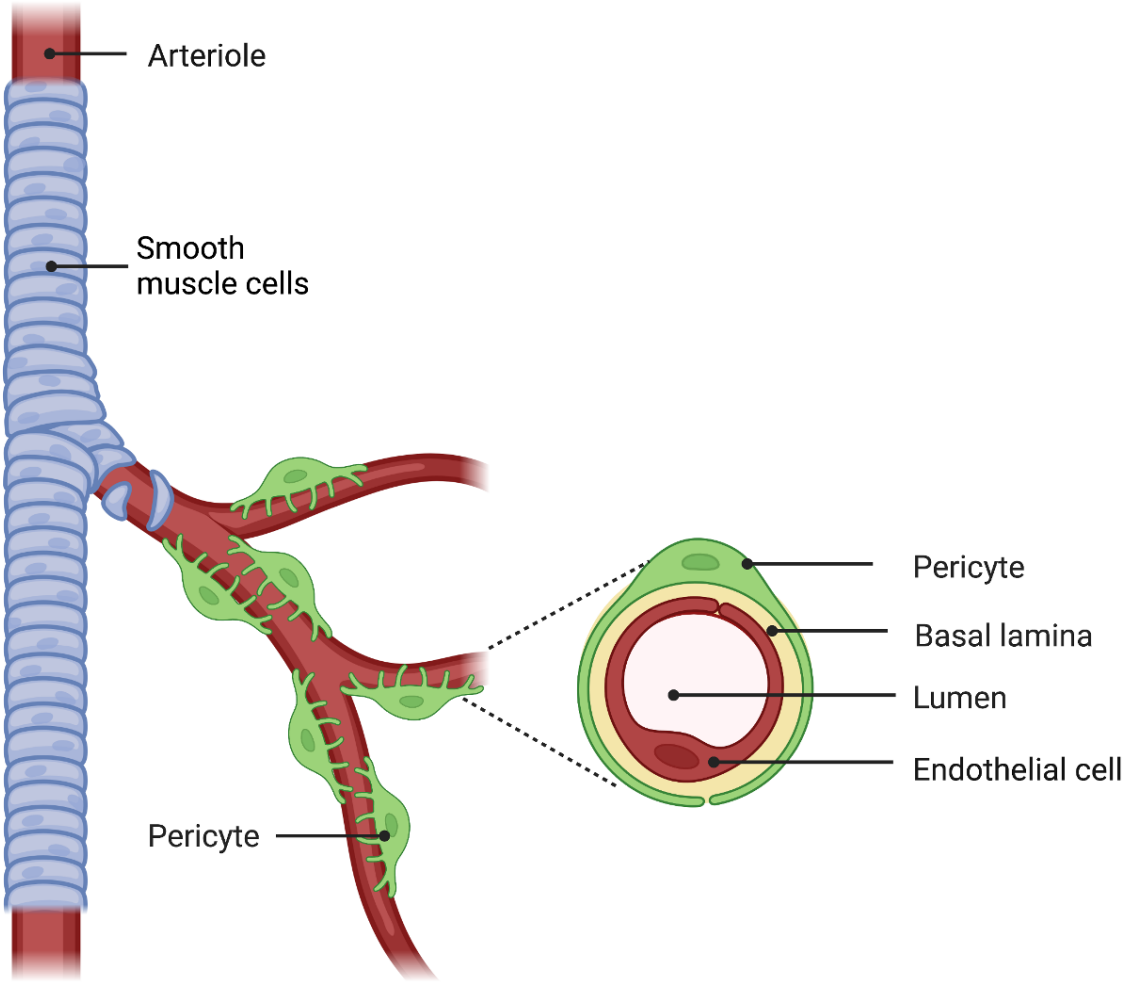

Figure 13 Schematic of branching luminized blood vessels.
Shown here are smooth muscle cells wrapped around a thicker arteriole vessel that branches into smaller capillary sized vessel wrapped by pericytes. Luminal cross-section of native vessel is also shown.

4.2. Methods

4.2.1. Cell Culture

Green fluorescent protein (GFP) expressing HUVECs (GFP-HUVECs, Angio-Proteomie) and human aortic SMCs (HuAoSMCs, Lonza) were cultured on 10μg/mL fibronectin-coated tissue culture-treated plates in either Endothelial Cell Growth Medium (EGM-2™ supplemented with EGM-2™ BullletKit™, Lonza) or Smooth Muscle Cell Growth Medium (SmGM-2™ supplemented with SmGM-2™ BulletKit™, Lonza), respectively. Red fluorescent protein (RFP) expressing human brain microvascular pericytes (RFP-HBMVPCs, Angio-Proteomie) were cultured on tissue culture-treated plates precoated with Quick Coating Solution (Angio-Proteomie) and supplemented with Pericyte Growth Medium (PGM, Angio-Proteomie). NHLFs were cultured on tissue culture-treated dishes with Fibroblast Growth Medium (FBM™ Basal Medium and FGM™-2 SingleQuots™ supplements, Lonza). Cells were used between passages 5-12. Media changes were performed every other day, and all cell types were split upon reaching ~80% confluency. All cells were housed in incubators under in 37˚C, with 5% CO2 and, 98% humidity.

4.2.2. Fibrinogen preparation

Fibrinogen from bovine plasma (Sigma) powder was dissolved in phosphate-buffered saline (PBS) at room temperature for 2-3hrs. The mixture was then filtered using a 0.2μm pore syringe filter (Fisher).

4.2.3. Microvascular Droplets

Optimization of medium components needed for supporting vascular assembly was achieved by collecting cells, counting, and resuspending them in various cell culture medium. Specifically, these cultures were mixed within a fibrin matrix consisting of 3mg/mL fibrinogen and 2U/mL thrombin, the cells were then seeded at 10μL aliquots per well within a 48-well tissue culture-treated plate (Fisher). HUVECs were co-cultured with either HuAoSMCs or NHLF, at a 1:1 ratio, at a seeding density of 4 million cells/mL each, leading to a total density of 8 million cells/mL, while RFP-HBMVPCs were loaded at 400,000 cells/mL. These perivascular cellular densities were selected for their robustness in generating highly branched networks (14). After seeding, the cell-fibrin mixtures were placed in a humidity chamber for 30 minutes allowing for fibrin polymerization. Cell culture media or media combinations were then added to each well. The media and media combinations included: EGM-2, SmGM-2, FGM-2, and PGM, as well as, 1:1 combinations of EGM-2:SmGM-2, EGM-2:FGM-2, and EGM-2:PGM.

4.2.4. Microfluidic Device Fabrication

Molds were generously proved by Dr. Roger Kamm, MIT. Single-channel polydimethylsiloxane (PDMS) microfluidic devices were made by mixing silicone base with its curing agent (Sylgard 184, Dow Corning) at a 10:1 ratio for 3-4 minutes. Air impurities were then purged by vacuum desiccation for 15 minutes. The PDMS mixture was then poured onto a negative epoxy mold of our microfluidic device and placed within an oven

at 70˚C for a minimum of 2 hours. Once polymerized, devices were cut out and media ports were biopsy punched (1.5mm, Miltex). The devices were then cleaned, and plasma bonded onto a square glass cover slide (#1 slides, Fisher). Bonded devices were then placed within an oven overnight for sterilization and storage for later use (**Fig. 14 A-B**).

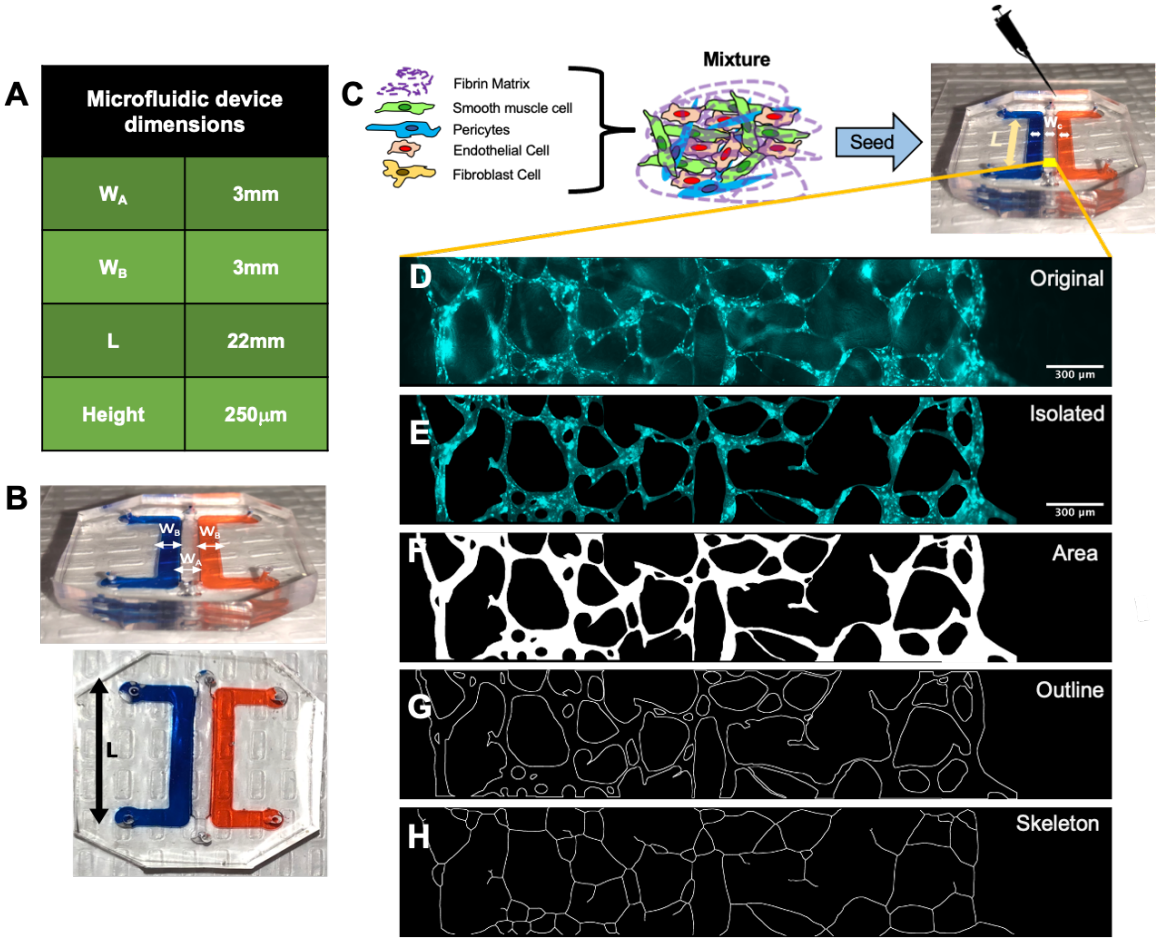

Figure 14 Microfluidic device ideal for vascular development.
A) *Dimensions of microfluidic device.* ***B)*** *Image of microfluidic device with side channels labeled by blue and orange dye.* ***C)*** *HUVECs are mixed within a 3mg/mL fibrin matrix in co- or tri- cultures of accessory cell types (pericytes, smooth muscle cells, or fibroblasts). This mixture, once homogeneous, is seeded into the center channel of our three-channel microfluidic device. The cell mixture is then provided cell specific mediums in the two adjacent channels, colored here in blue and orange. Over time the cells mixture will self-arrange into vascular networks.* ***D)*** *Vascular networks are imaged via our widefield epifluorescent microscope (TE-U2000). Using image processing techniques,* ***E)*** *we isolate the forefront vascular network.* ***F)*** *Networks then undergo "percentile" thresholding producing a binary image of the network. The binary image is then used to extract the* ***G)*** *outline of the network and the* ***H)*** *skeleton outline.*

4.2.5. Seeding Microfluidic Devices

Cells were collected and resuspended in cell culture medium volumes corresponding to the final desired densities and concentrations for each cell type. Cells were then mixed within a 3mg/mL fibrin matrix prepared by diluting 20mg/mL stock fibrinogen solution with 200U/mL stock thrombin solution (**Fig. 14C**) after which the mixture was injected into the center channel of the microfluidic device. HUVECs co-cultured with either

HuAoSMCs or NHLF were seeded at 4 million cells/mL, for a total of 8 million cells/mL, while HBM-PC were seeded at 400,000 cells/mL. Seeded devices were allowed to polymerize within a humidity chamber for 30 minutes, followed by the addition of 200μL of culture medium in the adjacent channels (**Fig. 14B**).

4.2.6. Feeding Microfluidic Devices

Microfluidic devices were supplemented with 200μL/channel of their corresponding medium every day. Each media channel received a different media depending on the cellular combination. I.e., one channel would receive EGM-2, while the other would receive media corresponding to the supplemental cell type, either SMGM-2 or FMG-2. For our tri-culture condition of HUVECs with both mural cells (HuAoSMCs and RFP-HBMVPCs) the media combination consisted of EGM-2 and SMGM-2.

4.2.7. Imaging microfluidic devices

Fluorescent images of the GFP-HUVECs and RFP-HBMVPCs were collected on an inverted widefield florescent microscope (Nikon Eclipse TE2000-U) over time. The collected fluorescent images were taken in such a way as to capture the entire cross-section of the center channel (**Fig. 14D**).

4.2.8. Quantification of lumen development and perfusion

Lumen formation was checked by collecting z-stacks of the vascular networks at 5μm z-steps (supplemental video 1). We checked for perfusion by first blocking trans located media pores on the microfluidic device, and then applying an asymmetric pressure difference across the vascular tissue via syringe pump and captured any cellular movement within the vascular network (supplemental video 2).

4.2.9. Image processing

Using custom-built image processing Macros in FIJI(167), we quantified the metrics of the developing vascular networks over time. Briefly, images were *cleaned up* by first eliminating background noise using the "*subtract background*" function in FIJI (**Fig. 14E**). The vascular networks were then isolated with the threshold function "Otsu" (**Fig. 14F**). Binary images were verified for accuracy by comparing them to their original fluorescent image. If binary images contained artifacts, they were manually removed. The isolated vascular networks were then *outlined* (**Fig. 14G**) and *skeletonized* (**Fig. 14H**). Fiji's "Analyze Particles…" function was used on the isolated *Area* image to quantify the networks area, and the outlined image was used to quantify vascular loop structures. The skeletonized image was further analyzed by the "Analyze Skeleton (2D/3D)" function leading to a quantification of the number of branches and branch lengths.

4.2.10. Quantification of vascular networks

Quantified data was saved as .txt files and further analyzed and plotted in Python(132). Specifically, we quantified and plotted the vascular network's effective diameter, mean

vessel length, vessel branch density, vessel area coverage, effective loop diameters, and tortuosity. The effective vessel diameter was calculated by dividing the total network area by the total length of the network. Here effective vessel diameters of <10μm are consistent with a capillary morphology, while those between 6μm-30μm are consistent with arterioles(179). The vessel branch density was calculated by dividing the total number of branches by the area of the image, in units of mm^2. The percent area coverage was calculated by dividing the area of the network by the total area of the image. Vascular loop diameters, also known as the interstitial space between vascular networks, was calculated only for those regions whose circularity was calculated to be greater than 0.6. Here circularity is calculated by FIJI(167) and is defined as $4*\pi(A_{loop}/P_{loop}^2)$ where A_{loop} is the area of the intestinal space and P_{loop} is the perimeter length. The area for loop's whose circularity was greater than 0.6 was then treated as the area of a circle and was used to solve for an effective diameter by solving for its diameter ($D_{loop} = (4*A_{loop}/\pi)^{0.5}$). Lastly, tortuosity, which is calculated by dividing the length of each branch by their Euclidian distance, is a measurement of how twisted or bent a vessel is. Additionally, while mild tortuosity is common, severe tortuosity has been shown to be the cause of ageing, diabetes, hypertension, etc. and has been shown to further lead to serious symptoms and diseases, such as myocardial infarction and/or stroke(180).

4.2.11. Statistical Analysis

Statistical significance was calculated by performing a Student's T-test. Significance was determined by a p-value of < 0.05. Plotted bar graphs are mean values ± standard deviation while plots relating to branch lengths are mean values ± standard error. All data shown represents an N=3 unless otherwise indicated.

4.3. Results

4.3.1. Role of Cell Culture Nutrients in Vascular Assembly

We preoptimize the medium components needed for supporting multicellular perivascular assembly and stability, by generating small microvascular droplets (10μL volumes) consisting of perivascular cells HUVECs, HuAoSMCs, and HBM-PC (at a 10:10:1 ratio) within 3mg/mL fibrin gels. The cultures were then treated with various combinations of cell culture mediums and their network development was tracked and quantified over 14 days (**Fig. 15**). We found that under the EGM-2 medium condition the vascular networks that emerged were highly interconnected at early time-points, with a mean number of 325 ± 43 branches, but lost this relatively high connectivity by day 14^{th}, decreasing to 113 ± 23 mean branches (**Fig. 15A-C**). Interestingly, while this network density decreased the vascular network diameters did not change over the same give time-period, vessel diameters remained between 23μm ± 1μm - 26μm ± 1μm over the 14 days. For cultures fed with only SmGM-2 or FGM-2, we found the networks to be unstable with visible network degradation as early as day 7 with a mean number of branches of 140 ± 9 and 46 ± 20 for SmGM-2 and FGM-2, respectfully (**Fig. 15D-I**). Additionally, cultures supplemented with FGM2 completely lost their interconnectivity by day 14 (**Fig.**

15 I). Cell cultures supplemented with pericyte growth medium (PGM) only, were found to have very similar vascular networks compared to the EGM-2 only condition with 348 ± 51 mean number of branches at day 7 and notably less branches by day 14, with 79 ± 22 branches. However, there was a notable lengthening of the mean branch lengths by day 14, increasing from 54μm ± 1 μm at day 7 to 73μm ± 6μm by day 14 (**Fig. 15J-L**). Cultures supplemented with a 1:1 ratio of EGM-2 to SmGM-2 cell culture mediums generated vasculature networks that were again comparable to the EGM-2 only condition but containing significantly narrower vessel diameters, between 22μm ± 1μm and 20μm ± 0μm over the 14 days. Additionally, this condition also contained significantly shorter branch lengths by day 14 at a mean length of 69μm ± 4 μm (**Fig. 15M-O**) compared to 91μm ± 4 μm for the EGM-2 only condition (**Fig. 15C**). Cultures supplemented with a 1:1 ratio of EGM-2 to FGM-2 (**Fig. 15P-R**) and EGM-2 to PGM (**Fig. 15S-U**) mediums lead to vascular networks that were statistically indistinguishable to the EGM-2 only media condition in terms of diameter, branch length, and number of branches by day 14 (**Fig. 15V-X**). Given these results, moving forward we will be supplementing perivascular culture with a 1:1 ratio of EGM-2 to SmGM-2 medium.

4.3.2. Vascular Assembly from HUVECs and NHLFs

To assess the long-term potential for vascular network assembly within our three-channel microfluidic device, designed by the Kamm group, we first set out to reproduce the network formation from previously successful mixtures of HUVECs and NHLFs(14). Here, we observed network assembly within the first 24 hours (not shown), and large network formations visible by day 2 with continuous remodeling up to day 7 (**Fig. 16A-C**). However, these cultures were unstable at longer time periods and showed signs of compaction by day 8 (**Appendix Fig. S10**) and were non-viable by day 14. Over the 7 days, the network's effective vascular network diameters and mean branch lengths per area almost doubled from 34 ± 5μm to 66 ± 4μm (**Fig. 16D**) and 56 ± 40μm to 106 ± 70μm (**Fig. 16E**), respectively, while the number of branches per area (count/mm^2) decreased from 274 ± 60 to 110 ± 9 (**Fig. 16F**), indicating at a continuous remodeling of the vascular network. The mean percent area covered by vascular networks was shown to be less informative, with the vascular networks area coverage peaking around day 4 with 90 ± 6% coverage (**Fig. 16G**). A significant increase in the diameter of the vascular loops, the interstitial space between vessels, was observed increasing from 16 ± 1μm to 28 ± 1μm (**Fig. 16H**). This supports the claim that the vascular networks are maturing over this remodeling period while the tortuosity, or change in vessel bendiness, did not change over the measured period (**Fig. 16I**).

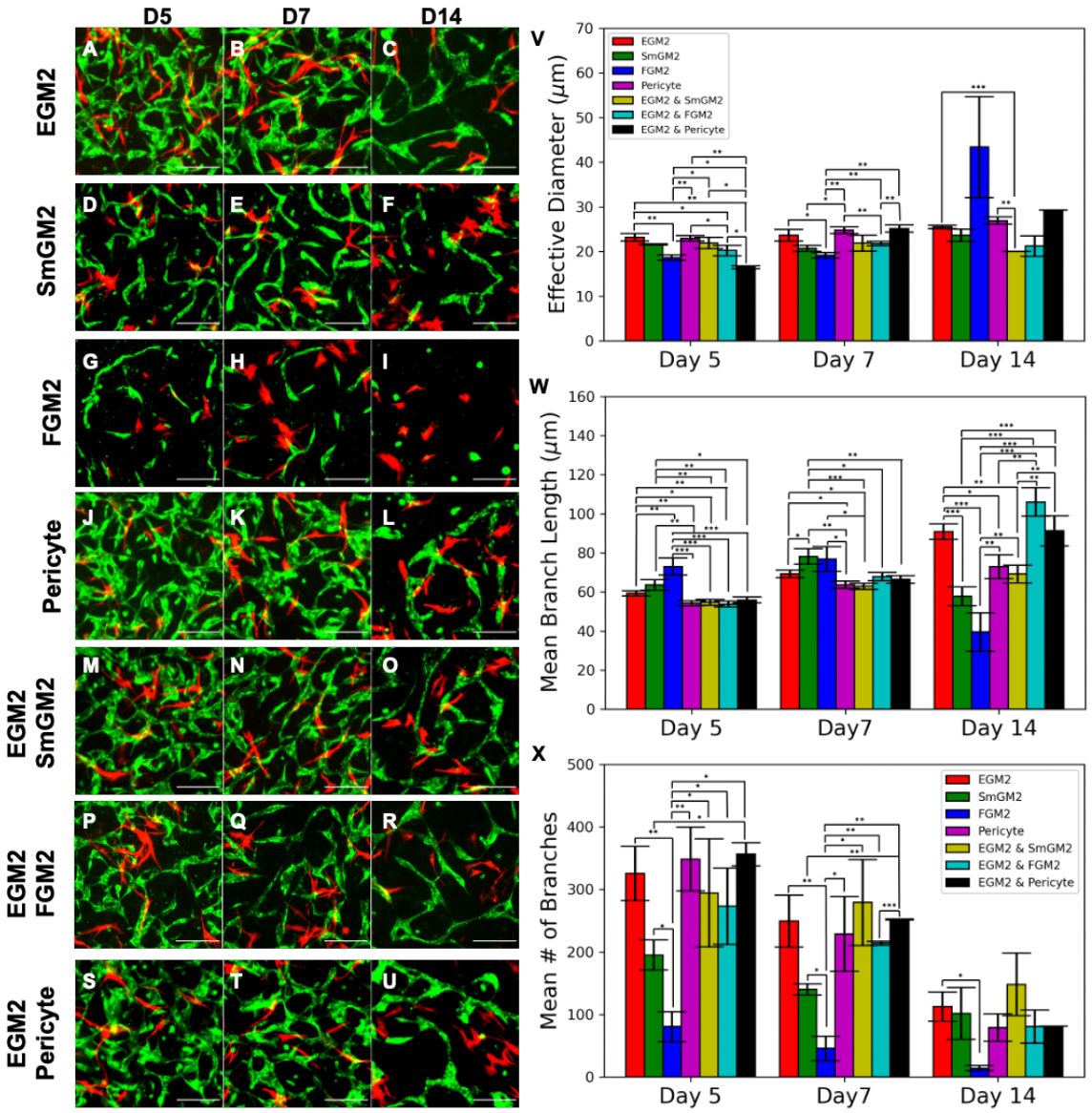

Figure 15: Impact of media on developing microvascular networks droplets from HUVECs : HuAoSMC : HBM-PC. Developing vasculature from GFP-tagged HUVECs (green), RFP-tagged HBM-PC (red), and HuAoSMC (not labeled) were imaged on days 5, 7, and 14 and were fed everyday one of the following media conditions. **A-C)** Vascular networks emerging from the EGM-2 medium only conditions imaged on days 5, 7, and 14. **D-F)** Vascular networks emerging from SmGM-2 media only. **G-I)** Vascular networks emerging from FGM-2 media only. **J-L)** Vascular networks emerging from pericyte media only. **M-O)** Vascular networks emerging from a 1:1 mixture of EGM-2 and SmGM-2. **P-R)** Vascular networks emerging from 1:1 EGM-2 and FGM-2 media mixture. **S-U)** Vascular networks emerging from 1:1 mixture of EGM-2 and Pericyte media. **V)** Quantification of the effective diameter of vascular networks on days 5, 7, and 14. Error bars are standard deviation. **W)** Quantification of the mean branch length. Error bars here are standard error from the mean (SEM). **X)** Quantification of the mean number of branches. Error bars are SEM. Image scale bars is 200μm. significance of * is determined by p-values less than 0.05, ** p-value < 0.01, and *** is for p-values less than 0.001.

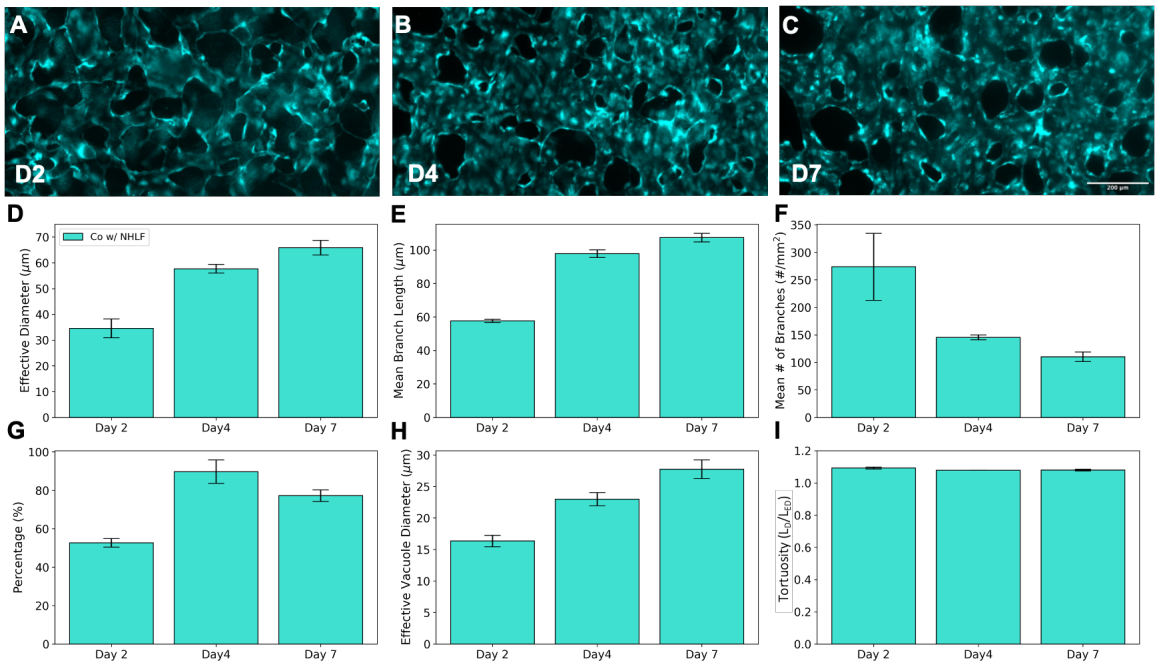

Figure 16: Vascular networks from HUVECs and NHLFs.
*Cultures of HUVECs and HHLFs were imaged on days **A)** 2, **B)** 4, and **C)** 7. HUVECs were pseudo-colored cyan. Image scale bar is 200μm. Quantification of images include **D)** effective vessel diameter, **E)** mean branch length, **F)** mean number of branches per mm², **G)** percent area coverage of networks, **H)** effective loop diameter, and **I)** vessel tortuosity over time. Error bars represent the standard deviation for D, G, and H, while the error bars for E, F, and I represent the SEM.*

4.3.3. Vascular Assembly from HUVECs and HBM-PC Degrade Within Two Weeks

ECs and pericytes were seeded at a previously determined ratios of 10:1 HUVECs to HBM-PC (preoptimized data not shown) and examined over time (**Fig. 17A-C**). Here, vascular networks that formed had an effective diameter of 41 ± 20μm by day 4 which increased to 60 ± 10μm by day 7 (**Fig. 17D**). Additionally, we observed these networks to display an inverse relationship between the mean branch length and the mean number of branches per area. Specifically, the mean branch length increased from 80 ± 3μm to 135 ± 10μm, whereas the mean number of branches decreased from 105 ± 20 to 42 ± 4 between days 4 and 7, we then observed a reversal of this trend between day 7 and 14 (**Fig. 17E-F**), although the vascular networks were observed to be regressing by day 14 (**Fig. 17C**). There were no statistically significant differences in the percent area coverage of the networks, vascular loop diameters, or in the network tortuosity (**Fig. 17G-I**). Lastly, we checked vessels for the formation of 3D structures on day 8 and observed branched networks that had sprouted perpendicular to the base network (**supplemental video 3**).

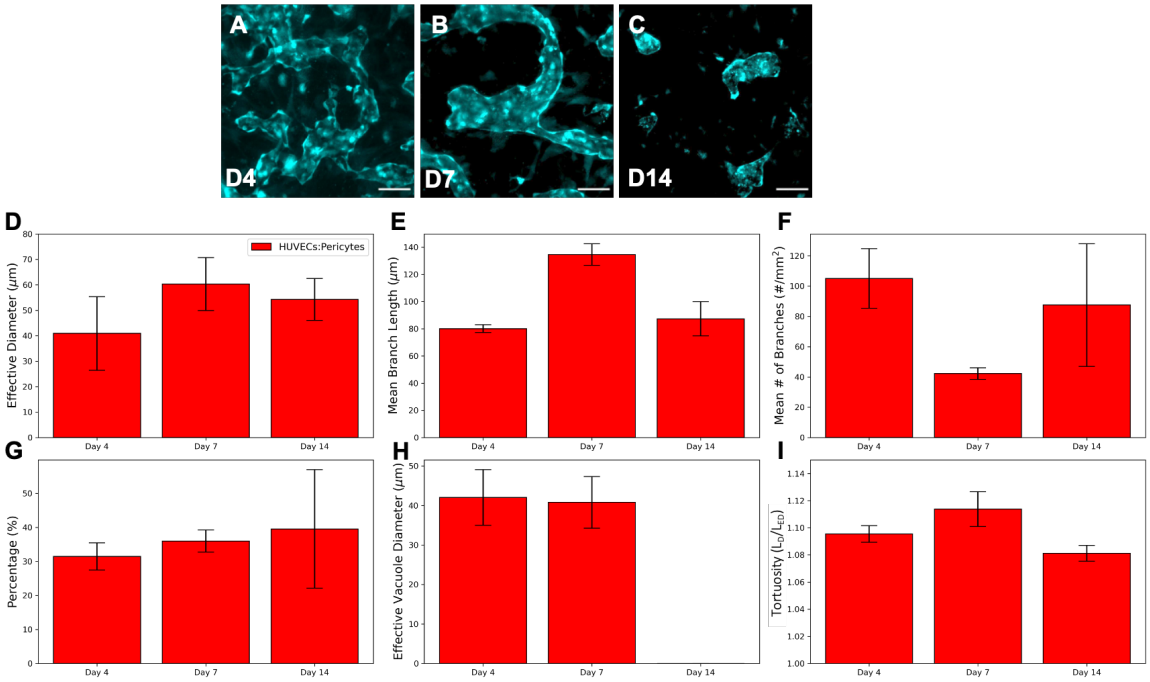

Figure 17 Vascular networks from HUVECs and HBM-PC.
*Cultures of HUVECs and HBM-PC were imaged on days **A)** 4, **B)** 7, and **C)** 14. HUVECs have been pseudo-colored cyan. Image scale bar is 100μm. Quantification of images include **D)** effective vessel diameter, **E)** mean branch length, **F)** mean number of branches per mm², **G)** percent area coverage of networks, **H)** effective loop diameter, and **I)** vessel tortuosity over time. Error bars represent the standard deviation for D, G, and H, while the error bars for E, F, and I represent the SEM.*

4.3.4. Vascular Assembly from HUVECs and HuAoSMCs Degrade by 7 Weeks

Although SMCs are not thought to play a significant role in normal microvasculature, we chose to assess their potential in stabilizing microvascular networks for longer timepoints due to their role in regulating the remodeling process of the vascular wall(181,182), a critical component in vasculature. HUVECs co-cultured with HuAoSMCs within a fibrin matrix generated microvascular networks exhibiting stability for up to 7 weeks (**Fig. 18 A-G**). Effective vessel diameters increased from 38 ± 5μm to 72 ± 3μm from day 4 to day 7, and then decreased to 39 ± 1μm by day 14, but then significantly increased again peaking at 73 ± 16μm by day 20. Effective vessel diameters for days 30, 40, and 50 remained relatively stable, ~40μm (**Fig. 18H**), with only 2 out of 3 of the cultures exhibit networks by day 40 and only 1 exhibiting networks by day 50. The mean branch length also increased, reaching its mean max length on day 20 at 165 ± 5μm, then decreasing to ~90μm from days 30 to 50 (**Fig. 18I**). The number of branches per given mm² also displayed a general decrease over the 50 days of continuous culture (**Fig. 18J**). The microvasculature was observed to cover the greatest percent area on day 7, with networks covering 72 ± 1% of the field of view and stabilizing after day 14 (**Fig. 18K**). The loop diameter was observed to peaked on day 20 with a mean loop diameter of 57 ± 8μm (**Fig. 18L**), while the tortuosity of the networks remained unchanging throughout the measured time period (**Fig. 18M**). The networks were checked for perfusability by flowing

1μm size fluorescent beads on day 9 (**supplemental video 4**). Video confirms that beads are flowing through vasculature and following distinct paths through the network (**Appendix Fig. S11A**).

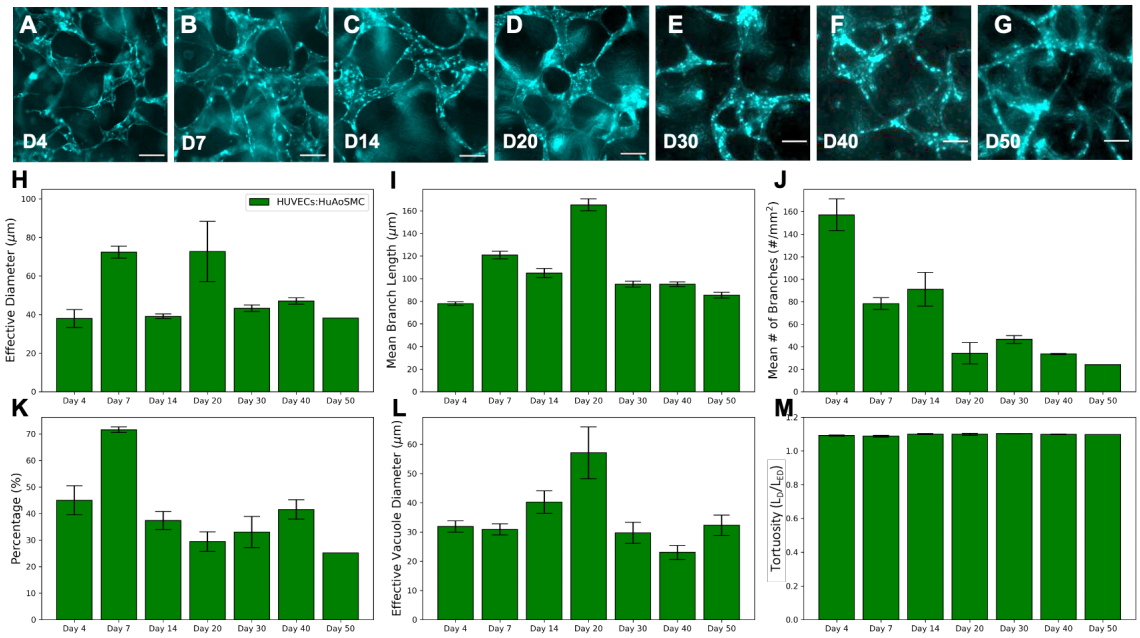

Figure 18 Vascular networks from HUVECs and HuAoSMCs.
*Cultures of HUVECs and HuAoSMCs were imaged on days **A)** 4, **B)** 7, **C)** 14, **D)** 20, **E)** 30, **F)** 40, and **G)** day 50. HUVECs have been pseudo-colored cyan. Image scale bar is 100μm. Quantification of images include **H)** effective vessel diameter, **I)** mean branch length, **J)** mean number of branches per mm², **K)** percent area coverage of networks, **L)** effective loop diameter, and **M)** vessel tortuosity over time. Error bars represent the standard deviation for H, K, and L, while the error bars for I, J, and M represent the SEM.*

4.3.5. Vascular Networks Emerging from Cultures of HUVECs, HuAoSMC, and HBM-PCs Exhibit Long-term Stability

Lastly, we seeded microfluidic devices with a tri-culture of HUVECs and perivascular mural cells (HuAoSMCs and HBM-PCs) at a 10:10:1 ratio within a 3mg/mL fibrin gel. The emerging vascular networks consisted of effective diameters that steadily increased between day 4 to day 14 (**Fig. 19A-C**), increasing from 21μm ± 1μm to 39μm ± 1μm, the vessel diameter then remained relatively stable for the next 36 days hovering between 31μm – 34μm (**Fig. 19D-G**), until the experiment was terminated at day 64 with intact vessels (**Fig. 19H**) with a mean effective diameter of 44μm ± 4μm (**Fig. 19I**). Furthermore, these vascular networks were shown to be perfusable by day 9 (**supplemental video 5**) where trapped cell debris is observed to follow distinct paths under flow. Additionally, fluorescent beads were also used on day 10 to check for perfusion (**supplemental video 6, Appendix Fig. S11B**). Lastly, these networks were also shown to be stable and luminized on day 53 as shown by Z-stack acquisition, which shows these microvascular networks to still be fully assembled (**supplemental video 7**) and containing pericytes wrapped around the vessels (**supplemental video 8**). Interestingly, we observed an

inverse relationship between the mean branch length and the mean number of branches per given area (mm^2). Specifically, we saw the mean branch length peak on day 20, with a mean branch length of 118 ± 4μm (**Fig. 19J**), while the mean number of branches bottoms out on day 20, with only 55 ± 3 branches per mm^2 (**Fig. 19K**). This trend holds as the mean number of branches decrease and the mean number of branches increases after day 20. Furthermore, we observed the percent area coverage also start to increase after day 20 (**Fig. 19L**). We observed the effective loop diameter display a similar behavior to that of the mean branch length, with a peak in the effective loop diameter of 48 ± 6μm at day 20 followed by a decrease (**Fig. 19M**). Again, we observed the vascular network tortuosity to be unaffected by changing vessel diameters and mean branch lengths (**Fig. 19N**).

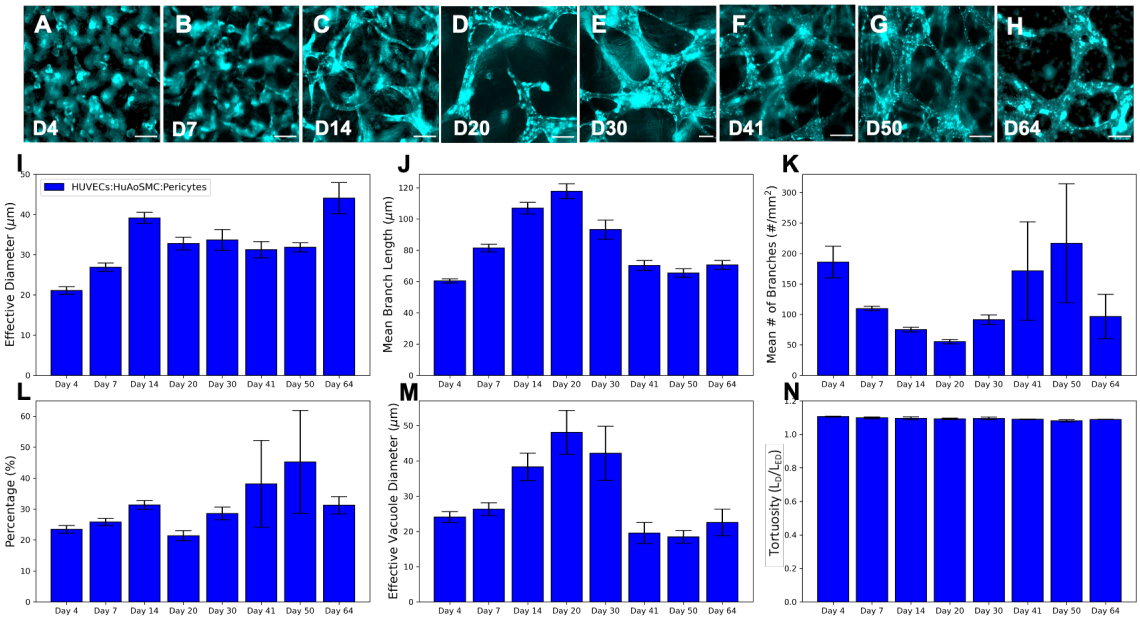

Figure 19 Vascular networks from HUVECs, HuAoSMCs, and HBM-PC.
*Cultures of HUVECs, HuAoSMCs, and HBM-PC were imaged on days **A)** 4, **B)** 7, **C)** 14, **D)** 20, **E)** 30, **F)** 41, **G)** 50 and **H)** day 64. HUVECs have been pseudo-colored cyan. Image scale bar is 100μm. Quantification of images include **I)** effective vessel diameter, **J)** mean branch length, **K)** mean number of branches per mm^2, **L)** percent area coverage of networks, **M)** effective loop diameter, and **N)** vessel tortuosity over time. Error bars represent the standard deviation for I, L, and M, while the error bars for J, K, and N represent the SEM.*

4.4. Discussion

Blood vessels exhibit structural and dimensional differences that align with their primary functions, specifically, arteries, veins, and capillaries all exhibit different functions with different types and amounts of perivascular cells (183). Additionally, the specialization of the cells within blood vessels directly aligns with the specific needs of the tissue in which they reside (15,90–92). For example, arteries contain a thicker layer of SMCs circumferentially aligned to control vasodilation and vasoconstriction while veins contain fewer SMCs. Arteries also contain internal and external elastic lamina composed of elastin and collagen fibers to support the highest blood pressures from the blood ejecting out of the heart while veins contain thinner walls. Within various blood vessel niches, a few

different cell types may be present alongside the ECs, including fibroblasts or mural cells: such as smooth muscle cells (SMC) and pericytes (**Fig. 13**). Fibroblasts, which are ECM producing powerhouses are largely associated with the outermost, adventitial, layer of an artery, but recent research has identified a vasculogenic fibroblasts that can behave and even contribute to vasculogenic growth directly by adopting a more endothelial cell like morphology. These vasculogenic fibroblasts emerge under tissue injury which leads to a loss in miR-200b levels(184).

In our studies, we explored the various roles of fibroblasts, smooth muscle cells and pericytes in vascular assembly and stability. We first used HUVECs with NHLFs due to the success of NHLFs in literature(14,114,115). The NHLF is a type of fibroblast that has been shown to exhibit vasculogenic potential when cultured with ECs(185). Within our co-cultures, we observed network formation as early as 24hrs post seeding, with full vasculature typically formed by day 4, followed by a rapid degradation of the cultures between days 7 to 8 (**Appendix Fig. S10**). We believe this degradation to be the result of vascular network compaction and potentially a loss of ECM architecture. Although collagen hydrogels are also permissive in forming vasculature(186), we chose to use fibrin, as it mimics natural wound healing and can induce network formation after injury(187). While we were successful in producing perfusable vascular networks from HUVECS and NHLFs, the degradation suggests a missing component or imbalance in the overall ECM composition, cellular concentrations, or other cell-based on paracrine signals.

In our studies, the use of both SMCs found in most blood vessels, but not found in capillaries, and pericytes found in smaller vessels and capillaries were observed to aid in the formation and long-term stability of perfusable vascular networks. While its known that SMCs contribute to the overall strength and elasticity of larger vessels (182), we found that SMCs, specifically HuAoSMCs, also lead to the development of smaller vessel diameters compared to our NHLF cultures, or pericytes or SMCs separately **(Fig. 18H)**. Furthermore, the developing networks, which are under static conditions, not only stabilized the developing vessels but also extend their overall longevity (>2 months). These networks were also perfusable as early as day 9 (**supplemental video 5**). Moreover, the HuAoSMCs co- and tri- cultures exhibited a latency in vessel emergence of 2 and 7 days, respectfully, suggesting a level of cell-to-cell communication and organization that leads to the long-term stability.

The pericytes, a type of cell that is known for its ability to stabilized blood vessels by wrapping around the vessel wall, also played a critical role in remodeling, permeability, and vessel maturation (**Fig. 13**). However, pericytes are a not well-characterized cell type that are heterogeneous, and arise from various origins (188), and exhibiting plasticity by differentiating into fibroblast-like cells, ventricular cardiomyocytes, and smooth muscle cell(189). Although we expected that the pericytes would aid integration and stabilization in developing vessels, this was not case in our co-cultures with HUVECs and HBM-PCs. In fact, any vessel that did emerge was unstable from conception and would undergo

apoptosis, degradation, or remodeled with 2 weeks. Interestingly, when HBM-PC were present with HuAoSMCs and HUVECs, we did observe the longest vessel stabilization (**Fig. 20**). This synergy between HUVECs, HuAoSMCs, and HBM-PC is an intriguing vascular model to untangle the underlying cell-to-cell communications and/or unique ECM compositions that can lead to long term (> 2 months) stable vessel formation.

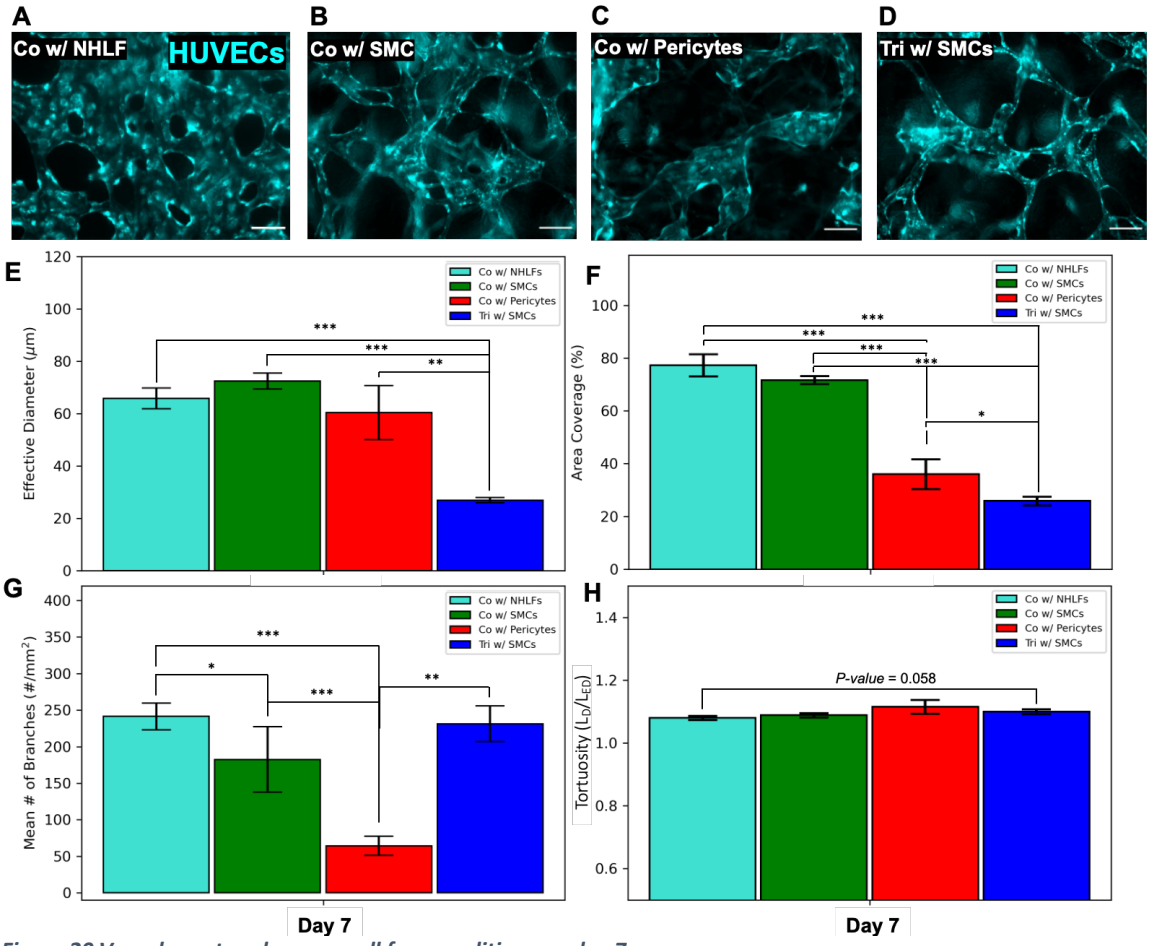

Figure 20 Vascular networks across all four conditions on day 7

*Images of vascular networks cultures composed of HUVEC with **A)** NHLFs, **B)** HuAoSMCs, **C)** HBM-PCs, and **D)** HuAoSMCs and HBM-PCs were allowed to self-assemble for 7 days under static conditions. Images were then quantified and plotted against each other. Shown here are their **E)** effective diameters (μm), **F)** area coverage, **G)** mean number of branches (normalized by area #/mm²) error bars are SEM, and **H)** the network tortuosity. Error bars represent the standard deviation unless otherwise mentioned. Image scale bars is 100μm. significance of * is determined by p-values less than 0.05, ** p-value < 0.01, and *** is for p-values less than 0.001.*

4.5. Conclusion

Here, we set out to explore the role that mural cells play in vascular assembly and long-term stability by using a simple three-channel microfluidic device. We found that HUVECs, cultured within a 3mg/mL fibrin gel with both HuAoSMCs and HBM-PCs will produce smaller-diameter vascular networks (~30μm) that remain stable for over 2 months, compared to conditions where ECs are seeded with either HuAoSMCs, HBM-PCs, or NHLFs alone. Moreover, we observed that after 21 days of continuous *stable* vasculature, the

vessels began exhibiting new angiogenic activity. To our knowledge, this is the first direct evidence of *in vitro* microvasculature remaining stable for more than 2 months and exhibiting both vasculogenic and angiogenic behavior. The next step would be to explore what leads to this long-term synergy. We hypothesis the ECM is playing a critical role in aiding and stabilizing this vascular development, but further testing is needed.

Chapter 5: Discussion and Conclusions

A major obstacle in the development of tissue engineered products for clinical applications is the challenge of generating perfusable vasculature, *in vitro*, throughout the tissue. This issue is amplified in both importance and scale when building larger, more complex, organs. Historically speaking, *in vitro* research has mostly looked at cell cultures under a 2D lens, however this method of studying the emergence of complex *in vivo* structures, such as blood vessels, is ineffective. Therefore, an important step in fully recapitulating the native tissue requires the use of 3D cell cultures such as those used in lab-on-a-chip technologies, including the use of microfluidic devices where primary vascular cells can be seeded within a 3D ECM and allowed to self-assemble into vascular network. Here mature cultures of endothelial cells and other accessory cell types can be seeded into microfluidic systems where they are allowed to self-assemble into perfusable vasculature(112,126,127). In these studies, co-cultures of ECs, such as HUVECs, and accessory cell types, such as fibroblasts (specifically NHLFs), are seeded into a fibrin or collagen ECM where they will, over the course of 4-7 days, migrate and self-assemble into perfusable vessels. This method, while promising, results in blood vessels that are limited in their long-term survival and stability, with most cultures degrading within 2 weeks.

Another promising approach for generating perfusable vasculature within tissues, employed the use of specific ECM components found within the specific organ system of interest. For the best results researchers are able to utilized a decellularized organ's ECM and repopulate it with the desired cells(118). While the use of these decellularized organs, such as heart(118,190), lung(191–193), kidney(194,195), and liver(196,197), are able to retain the highly branched vascular architecture, limited organ donor availability and shortages in desired cellular densities make this method challenging. A third approach for generating perfusable vasculature, utilizes stem cells for the direct differentiation of ECs (26,119) and accessory mural cells, such as SMCs (120–122). Here stem cells are guided into specific vascular fates by use of growth factors, specialized mediums, mechanical signaling, etc. (123). The benefit of this approach is the potential autologous use of a patient's own stem cells for the simultaneous directed differentiation of specific vascular cells that will immediately contribute to emerging vascular networks. While ideal, the simultaneous control of differentiating stem cells remains challenging. Additionally, such questions as to how vascular cells self-pattern, create primitive networks under different biological and mechanical conditions, as well as how to maintain functional vasculature stable for long terms once formed still remain elusive. In this dissertation I have attempted to shed light on these questions by exploring the 2D self-patterning of differentiating stem cell into EC and SMC (**Chapter 2**). I then used primary ECs, specifically HUVECs, to understand the importance of mechanical signals in cord-like vascular network development (**Chapter 3**). Lastly, I explored 3D vascular emergence by varying the types of vascular accessory cells (**Chapter 4**).

Firstly, I developed a computational population-based model that can be used to explore a broad range of motility, proliferation, and differentiation values to assess the impact that each has on the emergence of multicellular micropatterns within developing vascular tissues. Our work strongly suggests that, even in the absence of any specific mechanisms that can drive cell segregation, like chemotaxis, the observed experimental micropatterning of clustered ECs surrounded by SMCs can still emerge as long as the EC cellular factions are maintained within 30% – 70%. These computational results suggest that even though micropatterning can occur in the absence of sensing, the presence of such mechanisms greatly increases the robustness of the patterning, which we believe could be critical to fidelity in tissue development in the naturally noisy and heterogeneous *in vivo* setting.

Next, we explored two different seeding densities on a wide range of PAA stiffnesses in order to assess the relative importance of vascular cord-like network emergence from HUVEC monocultures. We found the HUVEC density to play a role in determining the timescale in which vascular cord-like networks would emerge. Specifically, we found the HUVEC density cannot be too high, or the network driving force will be outperformed by the HUVEC proliferation rate, leading to cluster formation rather than networks. Additionally, we found that HUVECs do indeed have a preferred stiffness range where they exhibited the greatest degree of network self-assembly, found here to be ~4.5kPa. These findings seem to suggest the presence of a tug of war feedback mechanism between cell-cell sensing and cell-substrate mechano-sensing. Simply put, we found that the underlying substrate's stiffness needs to be within the ideal range to facilitate cell spreading, sensing, and migration, while the cellular density has to simultaneously be low enough as to inhibit these behaviors. We hypothesize that the increase in cell densities leads to higher traction forces being generate and thus leading to an overall localized stiffening of the underlying substrate. This could explain the observed localized clustering of HUVECs rather than the desired chain-like networks. I believe this deserves further testing and exploration perhaps by conducting more thorough traction force microscopy measurement across the explored PAA stiffness range.

Lastly, I explored the role that mural cells, huAoSMCs and HBM-PCs, play in vascular assembly and long-term stability by seeding combinations of these cultures within a simple three-channel microfluidic device. We found that HUVECs, when cultured within a 3mg/mL fibrin gel with both HuAoSMCs and HBM-PCs would produce significantly smaller diameter perfusable vascular networks (~30μm) that could remain stable for over 2 months, compared to conditions where ECs are seeded alone with either HuAoSMCs, HBM-PCs, or NHLFs. Moreover, we observed that after 21 days of continuous stable vasculature, the vessels began to exhibit new angiogenic activity. To our knowledge, this is the first direct evidence of *in vitro* microvasculature remaining stable for more than 2 months while exhibiting both vasculogenic and angiogenic activity. However, these experiments raise many more questions about how to achieve vascular stability and why

other conditions were unable to do the same, including the co-culture of HUVECs with HuAoSMCs. We hypothesize that the relationship between the HuAoSMCs and HBM-PC plays a critical role in signaling the HUVECs to maintain their branched structure, but more studies are needed to explore this communication and cell-cell feedback. Alternatively, our observations could be the result of the ECM that is secreted by the SMCs in the presence of HBM-PC. If true this could explain why our cultures have such high longevity, but again further ECM quantification is needed.

During my Ph.D. I have had the opportunity to explore the differentiation process of ECs and SMCs from both mESCs and, to a lesser extent, human induced pluripotent stem cells. Unsurprisingly, this proved to be very challenging as stem cells are difficult to culture and during my early lab experiments the cultures were very prone to mycoplasma contamination. Regardless of these initial setbacks, I was eventually able to successfully culture these stem cells and fully differentiate the mESC in pure populations of ECs. Soon after we noticed the unique patters that ECs would produce during the early stages of the EC differentiation process where they would be surrounded by SMCs-like cells. These experiments helped motivate the development of my computational model which explore this patterning phenomenon and required me to learn to how to code.

Learning how to code came with a certain degree of difficulty but thanks to the Universities resources I was quickly able to learn and developed my computation model. My model strongly suggests that EC and SMCs can self-organize into distinct patterns as long as their ratios are conserved between 30% - 70%. However, upon trying to experimentally validate these results with primary cells, mainly HUVECs and HuAoSMCs, we ran into inconsistencies in the morphology and patterning of these cells. I believe this to be caused by culturing these cells on hard plastic tissue culture petri dishes. My solution was to transition these cultures on to soft hydrogels instead of traditional plastic petri dishes. However, a host of new question then arouse regarding the ideal stiffness range that should be used. As an initial experiment, I decided to first explore the find the ideal stiffness conditions that would be most conducive for EC growth. This led to an interesting observation of EC behavior under different PAA hydrogels that was later followed up with a computation model and a publication with the Dasbiswas lab, Noerr et. al.(171). However, the initial transition to using hydrogels was found to be too physically time consuming and very variable. This issue was amplified when seeding mESC and/or vascular progenitor cells (VPC), as the cells would rarely attach leading to apoptosis. After several years of trial and error I was finally able to develop a robust protocol for generating large quantities of PAA hydrogels at specific Young's Modulus (100Pa – 100kPa) that could support primary cells and VPCs. Unfortunately, I didn't have time to revisit the initial EC and SMC patterning validation experiments. What I did explore was chain-like network development of HUVECs on PAA hydrogels and found their preferred stiffness range to be around 4.5kPa(171). I believe these experiments highlight the importance of persistence and patience when developing new protocols. Additionally, these results contribute to the growing body of literature that aims at

transitioning cell cultures to more physiologically similar culture conditions via substrate manipulation.

My work also adds to the growing body of literature that explores the relationship between ECs and mural cells during vasculogenesis. The idea of culturing ECs with mural cells, while not new, come out of one of our group meetings where Dr. McCloskey mentioned that there was no direct literature evidence of these culture conditions. Baffled, I then proceeded to have numerous conversations with pivotal researchers in the field where I directly asked if culturing HUVECs with SMCs and PCs was possible and/or if they had seen anybody reporting it. Interestingly, I got very similar responses that were along the lines of “no, the maturity of the cells will be an issue”, “no, we tried and failed so we stopped”, and “no, why use primary cells if you can simply use SC or MSCs and directly differentiate them into the required cell phenotypes”. This last response perplexed me since I know that differentiating stem cells will often develop into teratomas(4) and other undesirable cell identities. Unconvinced, I decided to explore this issue for myself and found that not only is it possible to generate perfusable vessels with mural cells cultures, but these cultures had the potential to stabilize and initiate new angiogenic sprouts after 3 weeks. Put all together, my Ph.D. has explored the stem cell differentiation of vascular linages, the importance of mechanical signaling in network-like development, and lastly the development of vascular networks from HUVECs and mural cells. I expect my research contributions to aid in the development of perfusable organoids and organs, which are still currently limited to 200μm – 400μm diameters across(198) due to their inability to supply oxygen and nutrient to the cells in the inner core of the structure while simulations removing harmful waste byproducts.

References:

1. Spradling A, Drummond-Barbosa D, Kai T. Stem cells find their niche. Nature. 2001 Nov;414(6859):98–104.
2. Liu Y, Yang R, He Z, Gao WQ. Generation of functional organs from stem cells. Cell Regen. 2013;2(1):2:1.
3. Thomson JA. Embryonic stem cell lines derived from human blastocysts. Science (80-). 1998;282(5391):1145–7.
4. Takahashi K, Tanabe K, Ohnuki M, Narita M, Ichisaka T, Tomoda K, et al. Induction of Pluripotent Stem Cells from Adult Human Fibroblasts by Defined Factors. Cell. 2007;131(5):861–72.
5. Davis GE, Senger DR. Endothelial extracellular matrix: Biosynthesis, remodeling, and functions during vascular morphogenesis and neovessel stabilization. Circ Res. 2005;97(11):1093–107.
6. Tse JR, Engler AJ. Preparation of hydrogel substrates with tunable mechanical properties. Curr Protoc cell Biol. 2010 Jun;Chapter 10:Unit 10.16.
7. Engler AJ, Sen S, Sweeney HL, Discher DE. Matrix elasticity directs stem cell lineage specification. Cell. 2006 Aug;126(4):677–89.
8. Engler AJ, Griffin MA, Sen S, Bonnemann CG, Sweeney HL, Discher DE. Myotubes differentiate optimally on substrates with tissue-like stiffness: pathological implications for soft or stiff microenvironments. J Cell Biol. 2004 Sep;166(6):877–87.
9. Wingate K, Bonani W, Tan Y, Bryant SJ, Tan W. Compressive elasticity of three-dimensional nanofiber matrix directs mesenchymal stem cell differentiation to vascular cells with endothelial or smooth muscle cell markers. Acta Biomater. 2012 Apr;8(4):1440–9.
10. Xue R, Li JY-S, Yeh Y, Yang L, Chien S. Effects of matrix elasticity and cell density on human mesenchymal stem cells differentiation. J Orthop Res [Internet]. 2013 Sep;31(9):1360–5. Available from: http://www.ncbi.nlm.nih.gov/pubmed/23606500
11. Trappmann B, Gautrot JE, Connelly JT, Strange DGT, Li Y, Oyen ML, et al. Extracellular-matrix tethering regulates stem-cell fate. Nat Mater [Internet]. 2012;11(8):742–742. Available from: http://dx.doi.org/10.1038/nmat3339
12. Kim J, Jones CAR, Groves NS, Sun B. Three-dimensional reflectance traction microscopy. PLoS One. 2016;11(6):1–17.
13. Nerger BA, Siedlik MJ, Nelson CM. Microfabricated tissues for investigating traction forces involved in cell migration and tissue morphogenesis. Cell Mol Life Sci. 2017;74(10):1819–34.
14. Whisler JA, Chen MB, Kamm RD. Control of Perfusable Microvascular Network Morphology Using a Multiculture Microfluidic System. Tissue Eng Part C Methods. 2013;20(7):543–52.
15. Chen MB, Whisler JA, Fröse J, Yu C, Shin Y, Kamm RD. On-chip human microvasculature assay for visualization and quantification of tumor cell

extravasation dynamics. Nat Protoc. 2017;
16. Alvarez C V, Garcia-Lavandeira M, Garcia-Rendueles ME, Diaz-Rodriguez E, Garcia-Rendueles AR, Perez-Romero S, et al. Defining stem cell types: understanding the therapeutic potential of ESCs, ASCs, and iPS cells. J Mol Endocrinol. 2012 Aug;49(2):89.
17. Condic ML. Totipotency: What it is and what it is not. Stem Cells Dev. 2014;23(8):796–812.
18. Beeson D, Lippman A. Egg harvesting for stem cell research: medical risks and ethical problems. Reprod Biomed Online. 2006 Oct;13(4):573–9.
19. Meissner A, Wernig M, Jaenisch R. Direct reprogramming of genetically unmodified fibroblasts into pluripotent stem cells. Nat Biotechnol. 2007 Oct;25(10):1177–81.
20. Ko K, Tapia N, Wu G, Kim JB, Bravo MJA, Sasse P, et al. Induction of Pluripotency in Adult Unipotent Germline Stem Cells. Cell Stem Cell. 2009;5(1):87–96.
21. Lagasse E, Connors H, Al-Dhalimy M, Reitsma M, Dohse M, Osborne L, et al. Purified hematopoietic stem cells can differentiate into hepatocytes in vivo. Nat Med. 2000;6(11):1229–34.
22. Visvader JE, Clevers H. Tissue-specific designs of stem cell hierarchies. Nat Cell Biol. 2016;18(4):349–55.
23. Marcelo KL, Goldie LC, Hirschi KK. Regulation of Endothelial Cell Differentiation and Specification. Circ Res [Internet]. 2013 [cited 2017 Apr 24];112(9). Available from: http://circres.ahajournals.org/content/112/9/1272
24. Coffin JD, Harrison J, Schwartz S, Heimark R. Angioblast differentiation and morphogenesis of the vascular endothelium in the mouse embryo. Dev Biol. 1991;148(1):51–62.
25. Vokes SA, Krieg PA. Endoderm is required for vascular endothelial tube formation, but not for angioblast specification. Development. 2002;129(3):775–85.
26. Levenberg S, Golub JS, Amit M, Itskovitz-Eldor J, Langer R. Endothelial cells derived from human embryonic stem cells. Proc Natl Acad Sci [Internet]. 2002;99(7):4391–6. Available from: http://www.pnas.org/cgi/doi/10.1073/pnas.032074999
27. Itskovitz-Eldor J, Schuldiner M, Karsenti D, Eden A, Yanuka O, Amit M, et al. Differentiation of human embryonic stem cells into embryoid bodies compromising the three embryonic germ layers. Mol Med. 2000;6(2):88–95.
28. Robertson SM, Kennedy M, Shannon JM, Keller G. A transitional stage in the commitment of mesoderm to hematopoiesis requiring the transcription factor SCL/tal-1. Development [Internet]. 2000 Jun 1;127(11):2447–59. Available from: https://journals.biologists.com/dev/article/127/11/2447/40766/A-transitional-stage-in-the-commitment-of-mesoderm
29. Levenberg S, Ferreira LS, Chen-Konak L, Kraehenbuehl TP, Langer R. Isolation, differentiation and characterization of vascular cells derived from human embryonic stem cells. Nat Protoc. 2010;5(6):1115–26.
30. Ferreira LS, Gerecht S, Shieh HF, Watson N, Rupnick MA, Dallabrida SM, et al.

Vascular progenitor cells isolated from human embryonic stem cells give rise to endothelial and smooth muscle-like cells and form vascular networks in vivo. Circ Res. 2007;101(3):286–94.
31. Le Ricousse-Roussanne S, Barateau V, Contreres JO, Boval B, Kraus-Berthier L, Tobelem G. Ex vivo differentiated endothelial and smooth muscle cells from human cord blood progenitors home to the angiogenic tumor vasculature. Cardiovasc Res. 2004;62(1):176–84.
32. Wang ZZ, Au P, Chen T, Shao Y, Daheron LM, Bai H, et al. Endothelial cells derived from human embryonic stem cells form durable blood vessels in vivo. Nat Biotechnol. 2007;25(3):317–8.
33. Nakano T, Kodama H, Honjo T. In Vitro Development of Primitive and Definitive Erythrocytes from Different Precursors. Science (80-) [Internet]. 1996 May 3;272(5262):722–4. Available from: https://www.science.org/doi/10.1126/science.272.5262.722
34. Vodyanik MA, Bork JA, Thomson JA, Slukvin II. Human embryonic stem cell-derived CD34+ cells: Efficient production in the coculture with OP9 stromal cells and analysis of lymphohematopoietic potential. Blood. 2005;105(2):617–26.
35. Marcelo KL, Goldie LC, Hirschi KK. Regulation of endothelial cell differentiation and specification. Circ Res. 2013;112(9):1272–87.
36. Kane NM, Meloni M, Spencer HL, Craig MA, Strehl R, Milligan G, et al. Derivation of endothelial cells from human embryonic stem cells by directed differentiation: Analysis of microrna and angiogenesis in vitro and in vivo. Arterioscler Thromb Vasc Biol. 2010;30(7):1389–97.
37. Glaser DE, Turner WS, Madfis N, Wong L, Zamora J, White N, et al. Multifactorial Optimizations for Directing Endothelial Fate from Stem Cells. Rajasingh J, editor. PLoS One [Internet]. 2016 Dec 1;11(12):e0166663. Available from: https://dx.plos.org/10.1371/journal.pone.0166663
38. Glaser DE, Burns AB, Hatano R, Medrzycki M, Fan Y, McCloskey KE. Specialized mouse embryonic stem cells for studying vascular development. Stem Cells Cloning Adv Appl. 2014;7:79–88.
39. Blancas AA, Shih AJ, Lauer NE, McCloskey KE. Endothelial Cells from Embryonic Stem Cells in a Chemically Defined Medium. Stem Cells Dev [Internet]. 2011 Dec;20(12):2153–61. Available from: https://www.liebertpub.com/doi/10.1089/scd.2010.0432
40. Peichev M, Naiyer AJ, Pereira D, Zhu Z, Lane WJ, Williams M, et al. Expression of VEGFR-2 and AC133 by circulating human CD34+ cells identifies a population of functional endothelial precursors. Blood. 2000;95(3):952–8.
41. Asahara T. Isolation of Putative Progenitor Endothelial Cells for Angiogenesis. Science (80-) [Internet]. 1997;275(5302):964–6. Available from: http://www.sciencemag.org/cgi/doi/10.1126/science.275.5302.964
42. Gehling UM, Ergün S, Schumacher U, Wagener C, Pantel K, Otte M, et al. In vitro differentiation of endothelial cells from AC133-positive progenitor cells. Blood. 2000;95(10):3106–12.

43. Yamashita J, Itoh H, Hirashima M, Ogawa M, Nishikawa S, Yurugi T, et al. Flk1-positive cells derived from embryonic stem cells serve as vascular progenitors. Nature. 2000;408(6808):92–6.
44. Chen T, Bai H, Shao Y, Arzigian M, Janzen V, Attar E, et al. Stromal Cell-Derived Factor-1/CXCR4 Signaling Modifies the Capillary-Like Organization of Human Embryonic Stem Cell-Derived Endothelium In Vitro. Stem Cells. 2007;25(2):392–401.
45. Wong L, Kumar A, Gabela-Zuniga B, Chua J, Singh G, Happe CL, et al. Substrate stiffness directs diverging vascular fates. Acta Biomater [Internet]. 2019;96:321–9. Available from: https://doi.org/10.1016/j.actbio.2019.07.030
46. Humphrey JD, Dufresne ER, Schwartz MA. Mechanotransduction and extracellular matrix homeostasis. Nat Rev cell Biol. 2014 Dec;15(12):802–12.
47. Heinrichs A. Mechanotransduction: Switch and stretch. Nat Rev Mol Cell Biol [Internet]. 2009 Mar 11 [cited 2017 Apr 23];10(3):163–163. Available from: http://www.nature.com/doifinder/10.1038/nrm2642
48. Sawada Y, Tamada M, Dubin-Thaler BJ, Cherniavskaya O, Sakai R, Tanaka S, et al. Force Sensing by Mechanical Extension of the Src Family Kinase Substrate p130Cas. Cell [Internet]. 2006 [cited 2017 Apr 23];127(5):1015–26. Available from: http://www.sciencedirect.com/science/article/pii/S009286740601405X
49. Na S, Collin O, Chowdhury F, Tay B, Ouyang M, Wang Y, et al. Rapid signal transduction in living cells is a unique feature of mechanotransduction. Proc Natl Acad Sci U S A [Internet]. 2008 May 6 [cited 2017 Apr 23];105(18):6626–31. Available from: http://www.ncbi.nlm.nih.gov/pubmed/18456839
50. Riveline D, Zamir E, Balaban NQ, Schwarz US, Ishizaki T, Narumiya S, et al. Focal Contacts as Mechanosensors. J Cell Biol [Internet]. 2001 [cited 2017 Apr 23];153(6). Available from: http://jcb.rupress.org/content/153/6/1175.short
51. Dorland YL, Huveneers S. Cell–cell junctional mechanotransduction in endothelial remodeling. Cell Mol Life Sci. 2016;74(2):279–92.
52. Sun Z, Guo SS, Fässler R. Integrin-mediated mechanotransduction. J Cell Biol [Internet]. 2016;215(4):445–56. Available from: http://www.ncbi.nlm.nih.gov/pubmed/27872252%0Ahttp://www.pubmedcentral.nih.gov/articlerender.fcgi?artid=PMC5119943
53. Fukuda S, Schmid-Schonbein GW. Regulation of CD18 expression on neutrophils in response to fluid shear stress. Proc Natl Acad Sci. 2003;
54. Kiosses WB, Cao G, Schwartz MA, Engelhardt B, Dejana E, Schultz DA, et al. A mechanosensory complex that mediates the endothelial cell response to fluid shear stress. Nature. 2005;437(7057):426–31.
55. Plotkin LI, Speacht TL, Donahue HJ. Cx43 and Mechanotransduction in Bone. Curr Osteoporos Rep. 2015;13(2):67–72.
56. Treiser MD, Yang EH, Gordonov S, Cohen DM, Androulakis IP, Kohn J, et al. Cytoskeleton-based forecasting of stem cell lineage fates. Proc Natl Acad Sci. 2010;
57. Stanton AE, Tong X, Yang F. Extracellular matrix type modulates

mechanotransduction of stem cells. Acta Biomater [Internet]. 2019;96:310–20. Available from: https://doi.org/10.1016/j.actbio.2019.06.048
58. Humphries JD, Byron A, Humphries MJ. Integrin ligands at a glance. J Cell Sci. 2006;119(19):3901–3.
59. Piali L, Hammel P, Uherek C, Bachmann F, Gisler RH, Dunon D, et al. CD31/PECAM-1 is a ligand for αvβ3 integrin involved in adhesion of leukocytes to endothelium. J Cell Biol. 1995;130(2):451–60.
60. Peyton SR, Putnam AJ. Extracellular matrix rigidity governs smooth muscle cell motility in a biphasic fashion. J Cell Physiol. 2005;204(1):198–209.
61. Low BC, Pan CQ, Shivashankar G V., Bershadsky A, Sudol M, Sheetz M. YAP/TAZ as mechanosensors and mechanotransducers in regulating organ size and tumor growth. FEBS Lett. 2014;588(16):2663–70.
62. Harvey KF, Zhang X, Thomas DM. The Hippo pathway and human cancer. Nat Rev Cancer. 2013;13(4):246–57.
63. Ramos A, Camargo FD. The Hippo signaling pathway and stem cell biology. Trends Cell Biol [Internet]. 2012;22(7):339–46. Available from: http://dx.doi.org/10.1016/j.tcb.2012.04.006
64. Mammoto A, Connor KM, Mammoto T, Yung CW, Huh D, Aderman CM, et al. A mechanosensitive transcriptional mechanism that controls angiogenesis. Nature [Internet]. 2009 Feb 26 [cited 2017 Apr 23];457(7233):1103–8. Available from: http://www.nature.com/doifinder/10.1038/nature07765
65. Tse JR, Engler AJ. Preparation of hydrogel substrates with tunable mechanical properties. Curr Protoc Cell Biol. 2010;(SUPPL. 47):1–16.
66. Musah S, Wrighton PJ, Zaltsman Y, Zhong X, Zorn S, Parlato MB, et al. Substratum-induced differentiation of human pluripotent stem cells reveals the coactivator YAP is a potent regulator of neuronal specification. Proc Natl Acad Sci U S A [Internet]. 2014 Sep 23 [cited 2017 Apr 24];111(38):13805–10. Available from: http://www.ncbi.nlm.nih.gov/pubmed/25201954
67. Zhao W, Li X, Liu X, Zhang N, Wen X. Effects of substrate stiffness on adipogenic and osteogenic differentiation of human mesenchymal stem cells. Mater Sci Eng C [Internet]. 2014;40:316–23. Available from: http://dx.doi.org/10.1016/j.msec.2014.03.048
68. Sun Y, Yong KMA, Villa-Diaz LG, Zhang X, Chen W, Philson R, et al. Hippo/YAP-mediated rigidity-dependent motor neuron differentiation of human pluripotent stem cells. Nat Mater [Internet]. 2014 Jun 13;13(6):599–604. Available from: https://www.nature.com/articles/nmat3945
69. Smith Q, Chan XY, Carmo AM, Trempel M, Saunders M, Gerecht S. Compliant substratum guides endothelial commitment from human pluripotent stem cells. Sci Adv [Internet]. 2017 May;3(5):e1602883. Available from: http://www.ncbi.nlm.nih.gov/pubmed/28580421
70. Pearson S, Sroczynska P, Lacaud G, Kouskoff V. The stepwise specification of embryonic stem cells to hematopoietic fate is driven by sequential exposure to Bmp4, activin A, bFGF and VEGF. Development. 2008;135(8):1525–35.

71. Hill KL, Obrtlikova P, Alvarez DF, King JA, Keirstead SA, Allred JR, et al. Human embryonic stem cell-derived vascular progenitor cells capable of endothelial and smooth muscle cell function. Exp Hematol. 2010;
72. Smith Q, Stukalin E, Kusuma S, Gerecht S, Sun SX. Stochasticity and Spatial Interaction Govern Stem Cell Differentiation Dynamics. Sci Rep [Internet]. 2015;5:1–10. Available from: http://dx.doi.org/10.1038/srep12617
73. Lo W-C, Chou C-S, Gokoffski K, Wan F, Lander A, Calof A, et al. Feedback regulation in multistage cell lineages. Math Biosci Eng. 2008;
74. Porter B, Zauel R, Stockman H, Guldberg R, Fyhrie D. 3-D computational modeling of media flow through scaffolds in a perfusion bioreactor. J Biomech. 2005;38(3):543–9.
75. Mao Y, Tournier AL, Bates PA, Gale JE, Tapon N, Thompson BJ. Planar polarization of the atypical myosin Dachs orients cell divisions in Drosophila. Genes Dev. 2011;25(2):131–6.
76. Walker DC, Hill G, Wood SM, Smallwood RH, Southgate J. Agent-based computational modeling of wounded epithelial cell monolayers. IEEE Trans Nanobioscience. 2004;3(3):153–63.
77. Bearer EL, Lowengrub JS, Frieboes HB, Chuang YL, Jin F, Wise SM, et al. Multiparameter computational modeling of tumor invasion. Cancer Res. 2009;69(10):4493–501.
78. Drasdo D, Höhme S. A single-cell-based model of tumor growth in vitro: Monolayers and spheroids. Phys Biol. 2005;2(3):133–47.
79. Chou CS, Lo WC, Gokoffski KK, Zhang YT, Wan FYM, Lander AD, et al. Spatial dynamics of multistage cell lineages in tissue stratification. Biophys J. 2010;
80. Kelly DJ, Prendergast PJ. Mechano-regulation of stem cell differentiation and tissue regeneration in osteochondral defects. J Biomech. 2005;38(7):1413–22.
81. Du H, Wang Y, Haensel D, Lee B, Dai X, Nie Q. Multiscale modeling of layer formation in epidermis. PLoS Comput Biol. 2018;
82. Atala A. Re: Collective and single cell behavior in epithelial contact inhibition. J Urol. 2012;188(4):1396–7.
83. Grogan JA, Connor AJ, Markelc B, Muschel RJ, Maini PK, Byrne HM, et al. Microvessel Chaste: An Open Library for Spatial Modeling of Vascularized Tissues. Biophys J [Internet]. 2017;112(9):1767–72. Available from: http://dx.doi.org/10.1016/j.bpj.2017.03.036
84. Yachie-Kinoshita A, Onishi K, Ostblom J, Posfai E, Rossant J, Zandstra PW. Modeling signaling-dependent pluripotent cell states with Boolean logic can predict cell fate transitions. bioRxiv [Internet]. 2017; Available from: http://www.biorxiv.org/content/early/2017/03/10/115683.1
85. Nematbakhsh A, Sun W, Brodskiy PA, Amiri A, Narciso C, Xu Z, et al. Multi-scale computational study of the mechanical regulation of cell mitotic rounding in epithelia. PLoS Comput Biol. 2017;
86. Chen X, Wayne Brodland G. Multi-scale finite element modeling allows the mechanics of amphibian neurulation to be elucidated. Phys Biol. 2008;5(1).

87. Osborne JM, Fletcher AG, Pitt-Francis JM, Maini PK, Gavaghan DJ. Comparing individual-based approaches to modelling the self-organization of multicellular tissues. PLoS Comput Biol. 2017;
88. Viens D. A Three-dimensional Finite Element Model for the Mechanics of Cell-Cell Interactions. J Biomech Eng [Internet]. 2007;129(5):651. Available from: http://biomechanical.asmedigitalcollection.asme.org/article.aspx?doi=10.1115/1.2768375
89. Brodland GW, Clausi DA. Embryonic tissue morphogenesis modeled by FEM. J Biomech Eng [Internet]. 1994;116(2):146–55. Available from: http://www.ncbi.nlm.nih.gov/pubmed/8078321
90. Esch EW, Bahinski A, Huh D. Organs-on-chips at the frontiers of drug discovery. Nat Rev Drug Discov [Internet]. 2015;14(4):248–60. Available from: http://dx.doi.org/10.1038/nrd4539
91. Sung JH, Esch MB, Shuler ML. Integration of in silico and in vitro platforms for pharmacokinetic–pharmacodynamic modeling . Expert Opin Drug Metab Toxicol. 2010;6(9):1063–81.
92. Sung JH, Esch MB, Prot J, Long CJ, Smith A, Hickman J, et al. Integration into Models of Whole Animals and Humans. Lab Chip. 2014;13(7):1201–12.
93. Ghaemmaghami AM, Hancock MJ, Harrington H, Kaji H, Khademhosseini A. Biomimetic tissues on a chip for drug discovery. Drug Discov Today [Internet]. 2012;17(3–4):173–81. Available from: http://dx.doi.org/10.1016/j.drudis.2011.10.029
94. Shih YV, Varghese S. Tissue engineered bone mimetics to study bone disorders ex vivo: Role of bioinspired materials. Biomaterials [Internet]. 2019;198:107–21. Available from: https://doi.org/10.1016/j.biomaterials.2018.06.005
95. Yin F, Su W, Wang L, Hu Q. Microfluidic strategies for the blood-brain barrier construction and assessment. TrAC - Trends Anal Chem [Internet]. 2022;155:116689. Available from: https://doi.org/10.1016/j.trac.2022.116689
96. Portillo-Lara R, Spencer AR, Walker BW, Shirzaei Sani E, Annabi N. Biomimetic cardiovascular platforms for in vitro disease modeling and therapeutic validation. Biomaterials [Internet]. 2019;198(March 2018):78–94. Available from: https://doi.org/10.1016/j.biomaterials.2018.08.010
97. Sung JH, Yu J, Luo D, Shuler ML, March JC. Microscale 3-D hydrogel scaffold for biomimetic gastrointestinal (GI) tract model. Lab Chip. 2011;11(3):389–92.
98. Novik E, Maguire TJ, Chao P, Cheng KC, Yarmush ML. A microfluidic hepatic coculture platform for cell-based drug metabolism studies. Biochem Pharmacol. 2010;79(7):1036–44.
99. Huh D, Matthews BD, Mammoto A, Montoya-Zavala M, Hsin HY, Ingber DE. Reconstituting Organ-Level Lung Functions on a Chip. Science (80-) [Internet]. 2010 Jun 25;328(5986):1662–8. Available from: https://www.science.org/doi/10.1126/science.1188302
100. Valverde MG, Mille LS, Figler KP, Cervantes E, Li VY, Bonventre J V., et al. Biomimetic models of the glomerulus. Nat Rev Nephrol. 2022;18(4):241–57.

101. Shin Y, Han S, Jeon JS, Yamamoto K, Zervantonakis IK, Sudo R, et al. Microfluidic assay for simultaneous culture of multiple cell types on surfaces or within hydrogels. Nat Protoc [Internet]. 2012 Jun 7;7(7):1247–59. Available from: https://www.ncbi.nlm.nih.gov/pubmed/22678430
102. Siddique A, Meckel T, Stark RW, Narayan S. Improved cell adhesion under shear stress in PDMS microfluidic devices. Colloids Surfaces B Biointerfaces [Internet]. 2017;150:456–64. Available from: http://dx.doi.org/10.1016/j.colsurfb.2016.11.011
103. Wong AP, Perez-Castillejos R, Christopher Love J, Whitesides GM. Partitioning microfluidic channels with hydrogel to construct tunable 3-D cellular microenvironments. Biomaterials. 2008;29(12):1853–61.
104. Wang CC, Yang KC, Lin KH, Liu HC, Lin FH. A highly organized three-dimensional alginate scaffold for cartilage tissue engineering prepared by microfluidic technology. Biomaterials [Internet]. 2011;32(29):7118–26. Available from: http://dx.doi.org/10.1016/j.biomaterials.2011.06.018
105. Fischbach C, Chen R, Matsumoto T, Schmelzle T, Brugge JS, Polverini PJ, et al. Engineering tumors with 3D scaffolds. Nat Methods. 2007;4(10):855–60.
106. Krsko P, Libera M. Biointeractive hydrogels. Mater Today [Internet]. 2005;8(12):36–44. Available from: http://dx.doi.org/10.1016/S1369-7021(05)71223-2
107. Arslan U, Brescia M, Meraviglia V, Nahon DM, van Helden RWJ, Stein JM, et al. Vascularized hiPSC-derived 3D cardiac microtissue on chip. Stem Cell Reports [Internet]. 2023;18(7):1394–404. Available from: https://doi.org/10.1016/j.stemcr.2023.06.001
108. Chen Y, Chan HN, Michael SA, Shen Y, Chen Y, Tian Q, et al. A microfluidic circulatory system integrated with capillary-assisted pressure sensors. Lab Chip [Internet]. 2017;17(4):653–62. Available from: http://xlink.rsc.org/?DOI=C6LC01427E
109. Zervantonakis IK, Kothapalli CR, Chung S, Sudo R, Kamm RD. Microfluidic devices for studying heterotypic cell-cell interactions and tissue specimen cultures under controlled microenvironments. Biomicrofluidics. 2011;5(1).
110. Polacheck WJ, Li R, Uzel SGM, Kamm RD. Microfluidic platforms for mechanobiology. Lab Chip. 2013;13(12):2252–67.
111. Hsu H-H, Ko P-L, Peng C-C, Cheng Y-J, Wu H-M, Tung Y-C. Studying sprouting angiogenesis under combination of oxygen gradients and Co-culture of fibroblasts using microfluidic cell culture model. Mater Today Bio [Internet]. 2023;21(March):100703. Available from: https://doi.org/10.1016/j.mtbio.2023.100703
112. Hsu Y-H, Moya ML, Hughes CCW, George SC, Lee AP. A microfluidic platform for generating large-scale nearly identical human microphysiological vascularized tissue arrays. Lab Chip [Internet]. 2013;13(15):2990. Available from: http://xlink.rsc.org/?DOI=c3lc50424g
113. Campisi M, Shin Y, Osaki T, Hajal C, Chiono V, Kamm RD. 3D self-organized

microvascular model of the human blood-brain barrier with endothelial cells, pericytes and astrocytes. Biomaterials [Internet]. 2018;180:117–29. Available from: https://doi.org/10.1016/j.biomaterials.2018.07.014
114. Wan Z, Zhang S, Zhong AX, Shelton SE, Campisi M, Sundararaman SK, et al. A robust vasculogenic microfluidic model using human immortalized endothelial cells and Thy1 positive fibroblasts. Biomaterials [Internet]. 2021;276(March):121032. Available from: https://doi.org/10.1016/j.biomaterials.2021.121032
115. Kim S, Lee H, Chung M, Jeon NL. Engineering of functional, perfusable 3D microvascular networks on a chip. Lab Chip. 2013;13(8):1489–500.
116. Jeon JS, Bersini S, Gilardi M, Dubini G, Charest JL, Moretti M, et al. Human 3D vascularized organotypic microfluidic assays to study breast cancer cell extravasation. Proc Natl Acad Sci U S A. 2015;112(1):214–9.
117. Yamamoto K, Tanimura K, Watanabe M, Sano H, Uwamori H, Mabuchi Y, et al. Construction of Continuous Capillary Networks Stabilized by Pericyte-like Perivascular Cells. Tissue Eng Part A. 2019;25(5–6):499–510.
118. Ott HC, Matthiesen TS, Goh SK, Black LD, Kren SM, Netoff TI, et al. Perfusion-decellularized matrix: Using nature's platform to engineer a bioartificial heart. Nat Med. 2008;14(2):213–21.
119. McCloskey KE, Smith DA, Jo H, Nerem RM. Embryonic stem cell-derived endothelial cells may lack complete functional maturation in vitro. J Vasc Res. 2006;
120. Gong Z, Niklason LE. Use of Human Mesenchymal Stem Cells as Alternative Source of Smooth Muscle Cells in Vessel Engineering. In: Vemuri M, Chase LG, Rao MS, editors. Mesenchymal Stem Cell Assays and Applications [Internet]. Totowa, NJ: Humana Press; 2011. p. 279–94. Available from: https://doi.org/10.1007/978-1-60761-999-4_21
121. Owens GK. Regulation of differentiation of vascular smooth muscle cells. Physiol Rev. 1995;75(3):487–517.
122. Shen EM, McCloskey KE. Development of Mural Cells: From In Vivo Understanding to In Vitro Recapitulation. Stem Cells Dev [Internet]. 2017;26(14):1020–41. Available from: http://online.liebertpub.com/doi/10.1089/scd.2017.0020
123. Descamps B, Emanueli C. Vascular differentiation from embryonic stem cells: Novel technologies and therapeutic promises. Vascul Pharmacol [Internet]. 2012;56(5–6):267–79. Available from: http://dx.doi.org/10.1016/j.vph.2012.03.007
124. Blancas AA, Shih AJ, Lauer NE, McCloskey KE. Endothelial Cells from Embryonic Stem Cells in a Chemically Defined Medium. Stem Cells Dev [Internet]. 2011 Dec;20(12):2153–61. Available from: http://www.liebertonline.com/doi/abs/10.1089/scd.2010.0432
125. Szabó A, Ünnep R, Méhes E, Twal WO, Argraves WS, Cao Y, et al. Collective cell motion in endothelial monolayers. Phys Biol. 2010;7(4).

126. Sakaguchi K, Shimizu T, Horaguchi S, Sekine H, Yamato M, Umezu M, et al. In vitro engineering of vascularized tissue surrogates. Sci Rep. 2013;3:1–7.
127. Zhang J, Chu L, Hou Z, Schwartz MP, Hacker T, Vickerman V, et al. Functional characterization of human pluripotent stem cell-derived arterial endothelial cells. Proc Natl Acad Sci [Internet]. 2017;201702295. Available from: http://www.pnas.org/lookup/doi/10.1073/pnas.1702295114
128. Schreier B, Schwerdt G, Heise C, Bethmann D, Rabe S, Mildenberger S, et al. Substance-specific importance of EGFR for vascular smooth muscle cells motility in primary culture. Biochim Biophys Acta - Mol Cell Res [Internet]. 2016;1863(7):1519–33. Available from: http://dx.doi.org/10.1016/j.bbamcr.2016.03.017
129. Walter-Yohrling J, Morgenbesser S, Rouleau C, Bagley R, Callahan M, Weber W, et al. Murine Endothelial Cell Lines as Models of Tumor Endothelial Cells. Clin Cancer Res. 2004;10(6):2179–89.
130. Endlich N, Endlich K, Taesch N, Helwig JJ. Culture of vascular smooth muscle cells from small arteries of the rat kidney. Kidney Int. 2000;57(6):2468–75.
131. Nishikawa SI, Nishikawa S, Hirashima M, Matsuyoshi N, Kodama H. Progressive lineage analysis by cell sorting and culture identifies FLK1+VE-cadherin+ cells at a diverging point of endothelial and hemopoietic lineages. Development [Internet]. 1998;125(9):1747–57. Available from: http://www.ncbi.nlm.nih.gov/pubmed/9521912
132. Van Rossum G, Drake Jr FL. Python tutorial. Centrum voor Wiskunde en Informatica Amsterdam, The Netherlands; 1995.
133. MATLAB. version 9.1.0.441655 (R2016b). Natick, Massachusetts: The MathWorks Inc.; 2016.
134. Huttenlocher A, Lakonishok M, Kinder M, Wu S, Truong T, Knudsen KA, et al. Integrin and cadherin synergy regulates contact inhibition of migration and motile activity. J Cell Biol. 1998;141(2):515–26.
135. Abercrombie M, Heaysman JEM. Observations on the social behaviour of cells in tissue culture. II. “Monolayering” of fibroblasts. Exp Cell Res. 1954;6(2):293–306.
136. Steinberg MS. Does differential adhesion govern self-assembly processes in histogenesis? Equilibrium configurations and the emergence of a hierarchy among populations of embryonic cells. J Exp Zool. 1970;173(4):395–433.
137. Lilly B. We have contact: Endothelial cell-smooth muscle cell interactions. Physiology. 2014;29(4):234–41.
138. Moiseeva EP. Adhesion receptors of vascular smooth muscle cells and their functions. Cardiovasc Res. 2001;52(3):372–86.
139. Noseda M, Chang L, McLean G, Grim JE, Clurman BE, Smith LL, et al. Notch Activation Induces Endothelial Cell Cycle Arrest and Participates in Contact Inhibition: Role of p21Cip1 Repression. Mol Cell Biol. 2004;24(20):8813–22.
140. Sasine JP, Yeo KT, Chute JP. Concise Review: Paracrine Functions of Vascular Niche Cells in Regulating Hematopoietic Stem Cell Fate. Stem Cells Transl Med [Internet]. 2017 Feb 1;6(2):482–9. Available from:

https://doi.org/10.5966/sctm.2016-0254
141. Kirschenlohr HL, Metcalfe JC, Weissberg PL, Grainger DJ. Adult human aortic smooth muscle cells in culture produce active TGF-β. Am J Physiol - Cell Physiol. 1993;265(2 34-2).
142. Huang H, Zhao X, Chen L, Xu C, Yao X, Lu Y, et al. Differentiation of human embryonic stem cells into smooth muscle cells in adherent monolayer culture. Biochem Biophys Res Commun. 2006;351(2):321–7.
143. Rens EG, Zeegers MT, Rabbers I, Szabó A, Merks RMH. Autocrine inhibition of cell motility can drive epithelial branching morphogenesis in the absence of growth: Epithelial branching morphogenesis. Philos Trans R Soc B Biol Sci. 2020;375(1807).
144. Yoon SH, Kim YK, Han ED, Seo YH, Kim BH, Mofrad MRK. Passive control of cell locomotion using micropatterns: The effect of micropattern geometry on the migratory behavior of adherent cells. Lab Chip. 2012;12(13):2391–402.
145. Albert PJ, Schwarz US. Modeling cell shape and dynamics on micropatterns. Cell Adhes Migr [Internet]. 2016;10(5):516–28. Available from: http://dx.doi.org/10.1080/19336918.2016.1148864
146. Jiang X, Bruzewicz DA, Wong AP, Piel M, Whitesides GM. Directing cell migration with asymmetric micropatterns. Proc Natl Acad Sci U S A. 2005;102(4):975–8.
147. Ojeh N, Pastar I, Tomic-Canic M, Stojadinovic O. Stem Cells in Skin Regeneration, Wound Healing, and Their Clinical Applications. Int J Mol Sci. 2015 Oct;16(10):25476–501.
148. Johnson RI. Hexagonal patterning of the Drosophila eye. Dev Biol [Internet]. 2021;478(July):173–82. Available from: https://doi.org/10.1016/j.ydbio.2021.07.004
149. Wiley HS, Shvartsman SY, Lauffenburger DA. Computational modeling of the EGF-receptor system: A paradigm for systems biology. Trends Cell Biol. 2003;13(1):43–50.
150. Herbert SP, Stainier DYR. Molecular control of endothelial cell behaviour during blood vessel morphogenesis. Nat Rev Mol Cell Biol [Internet]. 2011;12(9):551–64. Available from: http://www.nature.com/doifinder/10.1038/nrm3176
151. Lee C-H, Poburko D, Kuo K-H, Seow CY, van Breemen C. Ca 2+ oscillations, gradients, and homeostasis in vascular smooth muscle. Am J Physiol Circ Physiol [Internet]. 2002 May 1;282(5):H1571–83. Available from: https://www.physiology.org/doi/10.1152/ajpheart.01035.2001
152. Giannotta M, Trani M, Dejana E. VE-cadherin and endothelial adherens junctions: Active guardians of vascular integrity. Dev Cell [Internet]. 2013;26(5):441–54. Available from: http://dx.doi.org/10.1016/j.devcel.2013.08.020
153. Humphrey JD, Dufresne ER, Schwartz MA. Mechanotransduction and extracellular matrix homeostasis. Nat Rev Mol Cell Biol. 2014;15(12):802–12.
154. Ling Y, Rubin J, Deng Y, Huang C, Demirci U, Karp JM, et al. A cell-laden microfluidic hydrogel. Lab Chip. 2007;7(6):756–62.
155. SMIDSROD O, SKJAKBRK G. Alginate as immobilization matrix for cells. Trends

Biotechnol [Internet]. 1990;8:71–8. Available from: https://linkinghub.elsevier.com/retrieve/pii/0167779990090139O
156. Ma J, Wang H, He B, Chen J. A preliminary in vitro study on the fabrication and tissue engineering applications of a novel chitosan bilayer material as a scaffold of human neofetal dermal fibroblasts. Biomaterials. 2001;22(4):331–6.
157. Azab AK, Orkin B, Doviner V, Nissan A, Klein M, Srebnik M, et al. Crosslinked chitosan implants as potential degradable devices for brachytherapy: In vitro and in vivo analysis. J Control Release. 2006;111(3):281–9.
158. Li Q, Williams CG, Sun DDN, Wang J, Leong K, Elisseeff JH. Photocrosslinkable polysaccharides based on chondroitin sulfate. J Biomed Mater Res - Part A. 2004;68(1):28–33.
159. Gillette BM, Jensen JA, Tang B, Yang GJ, Bazargan-Lari A, Zhong M, et al. In situ collagen assembly for integrating microfabricated three-dimensional cell-seeded matrices. Nat Mater. 2008;7(8):636–40.
160. Eyrich D, Brandl F, Appel B, Wiese H, Maier G, Wenzel M, et al. Long-term stable fibrin gels for cartilage engineering. Biomaterials. 2007;28(1):55–65.
161. Fukuda J, Khademhosseini A, Yeh J, Eng G, Cheng J, Farokhzad OC, et al. Micropatterned cell co-cultures using layer-by-layer deposition of extracellular matrix components. Biomaterials. 2006;27(8):1479–86.
162. Sahoo S, Chung C, Khetan S, Burdick JA. Hydrolytically degradable hyaluronic acid hydrogels with controlled temporal structures. Biomacromolecules. 2008;9(4):1088–92.
163. Rüdiger D, Kick K, Goychuk A, Vollmar AM, Frey E, Zahler S. Cell-Based Strain Remodeling of a Nonfibrous Matrix as an Organizing Principle for Vasculogenesis. Cell Rep. 2020;32(6).
164. Kim HJ, Kim UJ, Kim HS, Li C, Wada M, Leisk GG, et al. Bone tissue engineering with premineralized silk scaffolds. Bone. 2008;42(6):1226–34.
165. Vlierberghe S Van, Dubruel P, Schacht E. Biopolymer-based hydrogels as scaffolds for tissue engineering applications: a review. Biomacromolecules. 2011 May;12(5):1387–408.
166. Peloquin J, Huynh J, Williams RM, Reinhart-King CA. Indentation measurements of the subendothelial matrix in bovine carotid arteries. J Biomech [Internet]. 2011;44(5):815–21. Available from: http://dx.doi.org/10.1016/j.jbiomech.2010.12.018
167. Schindelin J, Arganda-Carreras I, Frise E, Kaynig V, Longair M, Pietzsch T, et al. Fiji: An open-source platform for biological-image analysis. Nat Methods. 2012;9(7):676–82.
168. Lowe DG. Distinctive image features from scale-invariant keypoints. Int J Comput Vis. 2004;60(2):91–110.
169. Butler JP, Toli-Nørrelykke IM, Fabry B, Fredberg JJ. Traction fields, moments, and strain energy that cells exert on their surroundings. Am J Physiol - Cell Physiol. 2002;282(3 51-3):595–605.
170. Wood JA, Liliensiek SJ, Russell P, Nealey PF, Murphy CJ. Biophysical cueing and

vascular endothelial cell behavior. Materials (Basel). 2010;3(3):1620–39.
171. Noerr PS, Zamora Alvarado JE, Golnaraghi F, McCloskey KE, Gopinathan A, Dasbiswas K. Optimal mechanical interactions direct multicellular network formation on elastic substrates. Proc Natl Acad Sci U S A. 2023;120(45):1–12.
172. Tsao CW, Aday AW, Almarzooq ZI, Anderson CAM, Arora P, Avery CL, et al. Heart Disease and Stroke Statistics—2023 Update: A Report From the American Heart Association. Circulation [Internet]. 2023 Feb 21;147(8). Available from: https://www.ahajournals.org/doi/10.1161/CIR.0000000000001123
173. Gaengel K, Genové G, Armulik A, Betsholtz C. Endothelial-mural cell signaling in vascular development and angiogenesis. Vol. 29, Arteriosclerosis, Thrombosis, and Vascular Biology. 2009. p. 630–8.
174. Carmeliet P, Jain RK. Molecular mechanisms and clinical applications of angiogenesis. Nature. 2011.
175. Potente M, Gerhardt H, Carmeliet P. Basic and therapeutic aspects of angiogenesis. Cell [Internet]. 2011;146(6):873–87. Available from: http://dx.doi.org/10.1016/j.cell.2011.08.039
176. Bergers G. The role of pericytes in blood-vessel formation and maintenance. Neuro Oncol [Internet]. 2005;7(4):452–64. Available from: https://academic.oup.com/neuro-oncology/article-lookup/doi/10.1215/S1152851705000232
177. Jung O, Tung YT, Sim E, Chen YC, Lee E, Ferrer M, et al. Development of human-derived, three-dimensional respiratory epithelial tissue constructs with perfusable microvasculature on a high-throughput microfluidics screening platform. Biofabrication. 2022;14(2).
178. Carrion B, Huang CP, Ghajar CM, Kachgal S, Kniazeva E, Jeon NL, et al. Recreating the perivascular niche ex vivo using a microfluidic approach. Biotechnol Bioeng. 2010;107(6):1020–8.
179. Tajeddin A, Mustafaoglu N. Design and fabrication of organ-on-chips: Promises and challenges. Micromachines. 2021;12(12):1–33.
180. Han HC. Twisted blood vessels: Symptoms, etiology and biomechanical mechanisms. J Vasc Res. 2012;49(3):185–97.
181. Jaminon A, Reesink K, Kroon A, Schurgers L. The role of vascular smooth muscle cells in arterial remodeling: Focus on calcification-related processes. Int J Mol Sci. 2019;20(22).
182. Lacolley P, Regnault V, Segers P, Laurent S. Vascular smooth muscle cells and arterial stiffening: Relevance in development, aging, and disease. Physiol Rev. 2017;97(4):1555–617.
183. Lawson ND, Weinstein BM. Arteries and veins: Making a difference with zebrafish. Nat Rev Genet. 2002;3(9):674–82.
184. Pal D, Ghatak S, Singh K, Abouhashem AS, Kumar M, El Masry MS, et al. Identification of a physiologic vasculogenic fibroblast state to achieve tissue repair. Nat Commun. 2023;14(1).
185. Sewell-Loftin MK, Bayer SVH, Crist E, Hughes T, Joison SM, Longmore GD, et al.

Cancer-associated fibroblasts support vascular growth through mechanical force. Sci Rep. 2017;7(1):1–12.
186. Raghavan S, Nelson CM, Baranski JD, Lim E, Chen CS. Geometrically controlled endothelial tubulogenesis in micropatterned gels. Tissue Eng - Part A. 2010;16(7):2255–63.
187. Clark RAF. Fibrin and wound healing. Ann N Y Acad Sci. 2001;936:355–67.
188. Henrique Dias Moura Prazeres P, Fernandes Gilson Sena I, da Terra Borges I, Orestes de Azevedo P, Peres Andreotti J, Emília de Paiva A, et al. PERICYTES ARE HETEROGENEOUS IN THEIR ORIGIN WITHIN THE SAME TISSUE HHS Public Access Author manuscript. Dev Biol [Internet]. 2017;427(1):6–11. Available from: https://www-ncbi-nlm-nih-gov.ezproxy.lib.ucalgary.ca/pmc/articles/PMC6076854/pdf/nihms982467.pdf
189. Birbrair A, Da Terra Borges I, Gilson Sena IF, Almeida GG, Da Silva Meirelles L, Gonçalves R, et al. How Plastic Are Pericytes? Stem Cells Dev. 2017;26(14):1013–9.
190. Wainwright JM, Czajka CA, Patel UB, Freytes DO, Tobita K, Gilbert TW, et al. Preparation of Cardiac Extracellular Matrix from an Intact Porcine Heart. Tissue Eng Part C Methods [Internet]. 2010;16(3):525–32. Available from: http://www.liebertonline.com/doi/abs/10.1089/ten.tec.2009.0392
191. Daly AB, Wallis JM, Borg ZD, Bonvillain RW, Deng B, Ballif BA, et al. Initial Binding and Recellularization of Decellularized Mouse Lung Scaffolds with Bone Marrow-Derived Mesenchymal Stromal Cells. Tissue Eng Part A. 2012;
192. Cortiella J, Niles J, Cantu A, Brettler A, Pham A, Vargas G, et al. Influence of Acellular Natural Lung Matrix on Murine Embryonic Stem Cell Differentiation and Tissue Formation. Tissue Eng Part A [Internet]. 2010;16(8):2565–80. Available from: http://www.liebertonline.com/doi/abs/10.1089/ten.tea.2009.0730
193. Ott HC, Clippinger B, Conrad C, Schuetz C, Pomerantseva I, Ikonomou L, et al. Regeneration and orthotopic transplantation of a bioartificial lung. Nat Med [Internet]. 2010;16(8):927–33. Available from: http://dx.doi.org/10.1038/nm.2193
194. Nakayama KH, Batchelder CA, Lee CI, Tarantal AF. Decellularized Rhesus Monkey Kidney as a Three-Dimensional Scaffold for Renal Tissue Engineering. Tissue Eng Part A [Internet]. 2010;16(7):2207–16. Available from: http://www.liebertonline.com/doi/abs/10.1089/ten.tea.2009.0602
195. Orlando G, Booth C, Wang Z, Totonelli G, Ross CL, Moran E, et al. Discarded human kidneys as a source of ECM scaffold for kidney regeneration technologies. Biomaterials [Internet]. 2013;34(24):5915–25. Available from: http://www.ncbi.nlm.nih.gov/pubmed/23680364
196. Uygun BE, Soto-Gutierrez A, Yagi H, Izamis ML, Guzzardi MA, Shulman C, et al. Organ reengineering through development of a transplantable recellularized liver graft using decellularized liver matrix. Nat Med. 2010;
197. Soto-Gutierrez A, Zhang L, Medberry C, Fukumitsu K, Faulk D, Jiang H, et al. A Whole-Organ Regenerative Medicine Approach for Liver Replacement. Tissue Eng

Part C Methods [Internet]. 2011;17(6):677–86. Available from: http://www.liebertonline.com/doi/abs/10.1089/ten.tec.2010.0698

198. Auger FA, Gibot L, Lacroix D. The pivotal role of vascularization in tissue engineering. Annu Rev Biomed Eng. 2013;15:177–200.

Appendix

Appendix Table 1:Linear Fit Equations.

	d_B= 0.001	**d_B= 0.01**	**d_B= 0.025**	**d_B= 0.03**	**d_B= 0.05**	**d_B= 0.08**	**d_B= 0.1**
J_B= 0.001	Y = 19.84x -146.12	Y = 21.26x -165.53	Y = 17.64x - 43.44	Y = 16.66x - 31.43	Y = 14.87x -19.04	-	-
J_B= 0.0079	Y = 286.79x - 1956.65	Y = 283.86x - 1940.75	Y = 281.36x - 1986.97	Y = 148.59x - 260.54	Y = 224.94x - 959.26	Y = 106.93x - 116.78	-
J_B= 0.01	Y = 371.96x - 2246.09	Y = 365.01x - 2126.33	Y = 362.36x - 2166.01	Y = 355.47x - 2117.49	Y = 337.73x - 1807.71	Y = 144.67x - 169.30	-
J_B= 0.03	Y = 1118.94x -2729.90	Y = 1116.90x -2960.47	Y = 1098.93x -2816.26	Y = 1092.09x -2744.39	Y = 1066.05x -2642.59	Y = 1049.67x -2865.79	Y = 1014.87x -2619.39
J_B= 0.05	Y = 1870.09x -3139.01	Y = 1859.48x -3232.19	Y = 1836.85x -3301.56	Y = 1816.78x -3036.47	Y = 1782.94x -3262.71	Y = 1725.46x -2975.61	Y = 1710.48x -3217.93
J_B= 0.08	Y = 2999.64x -3618.62	Y = 2974.24x -3769.00	Y = 2931.58x -3576.58	Y = 2902.39x -3457.22	Y = 2852.90x -3577.29	Y = 2773.15x -3521.62	Y = 2729.22x -3531.51
J_B= 0.1	Y = 3732.18x -3770.78	Y = 3705.19x -3935.06	Y = 3644.27x -3569.18	Y = 3639.61x -3949.63	Y = 3561.01x -3788.22	Y = 3472.11x -4032.90	Y = 3401.06x -3838.41

Appendix Table 2: R^2 fit values for Linear Equations.

	d_B= 0.001	**d_B= 0.01**	**d_B= 0.025**	**d_B= 0.03**	**d_B= 0.05**	**d_B= 0.08**	**d_B= 0.1**
J_B= 0.001	0.987	0.988	0.993	0.995	0.998	NaN	NaN
J_B= 0.0079	0.998	0.998	0.997	0.994	0.991	1	NaN
J_B= 0.01	0.999	0.999	0.999	0.999	0.996	0.999	NaN
J_B= 0.03	1	1	1	1	1	1	0.999
J_B= 0.05	1	1	1	1	1	1	1
J_B= 0.08	1	1	1	1	1	1	1
J_B= 0.1	1	1	1	1	1	1	1

Appendix Table 3: Quadratic Fit Equations.

	d_B= 0.001	d_B= 0.01	d_B= 0.025	d_B= 0.03	d_B= 0.05	d_B= 0.08	d_B= 0.1
J_B= 0.001	-	-	$Y = 0.38x^2 + 2.16x + 125.86$	$Y = 0.51x^2 - 1.29x + 157.69$	$Y = 0.91x^2 - 1.45x + 33.32$	$Y = 2.21x^2 - 40.24x + 367.39$	$Y = 3.01x^2 - 50.67x + 359.71$
J_B= 0.0079	-	-	-	$Y = 0.20x^2 + 263.59x - 1944.62$	$Y = 7.70x^2 - 431.20x + 13964.86$	$Y = 11.18x^2 - 245.55x + 3268.49$	$Y = 15.25x^2 - 332.77x + 3437.50$
J_B= 0.01	-	-	-	-	$Y = 11.68x^2 - 931.27x + 32528.30$	$Y = 13.90x^2 - 319.12x + 4407.44$	$Y = 18.70x^2 - 409.63x + 4193.76$
J_B= 0.03	-	-	-	-	-	$Y = 53.97x^2 -3495.21x + 86527.69$	$Y = 62.63x^2 - 2958.44x + 57364.95$
J_B= 0.05	-	-	-	-	-	$Y = 101.51x^2 - 8466.75x + 240123.21$	$Y = 108.78x^2 - 6214.86x + 131037.29$
J_B= 0.08	-	-	-	-	-	$Y = 199.59x^2 - 21049.61x + 691693.12$	$Y = 185.83x^2 - 12837.28x + 300726.96$
J_B= 0.1	-	-	-	-	-	$Y = 279.16x^2 - 32513.41x + 1138285.27$	$Y = 240.13x^2 - 17980.69x + 445481.52$

Appendix Table 4: R^2 fit values for Quadratic Equations.

	d_B= 0.001	d_B= 0.01	d_B= 0.025	d_B= 0.03	d_B= 0.05	d_B= 0.08	d_B= 0.1
J_B= 0.001	-	-	1.0000	0.9999	0.9995	0.9975	0.9978
J_B= 0.0079	-	-	-	0.9998	0.9995	0.9985	0.9988
J_B= 0.01	-	-	-	-	0.9999	0.9987	0.9989
J_B= 0.03	-	-	-	-	-	0.9999	0.9999
J_B= 0.05	-	-	-	-	-	0.9997	0.9998
J_B= 0.08	-	-	-	-	-	0.9993	0.9996
J_B= 0.1	-	-	-	-	-	0.9991	0.9994

Appendix Table 5: Time-point Transitions (in hours) from Linear to Quadratic Domains.

	d_B= 0.001	d_B= 0.01	d_B= 0.025	d_B= 0.03	d_B= 0.05	d_B= 0.08	d_B= 0.1
J_B= 0.001	-	-	26	18	8	2	1
J_B= 0.0079	-	-	-	12	39	3	1
J_B= 0.01	-	-	-	-	63	4	1
J_B= 0.03	-	-	-	-	-	50	35
J_B= 0.05	-	-	-	-	-	59	42
J_B= 0.08	-	-	-	-	-	66	49
J_B= 0.1	-	-	-	-	-	70	51

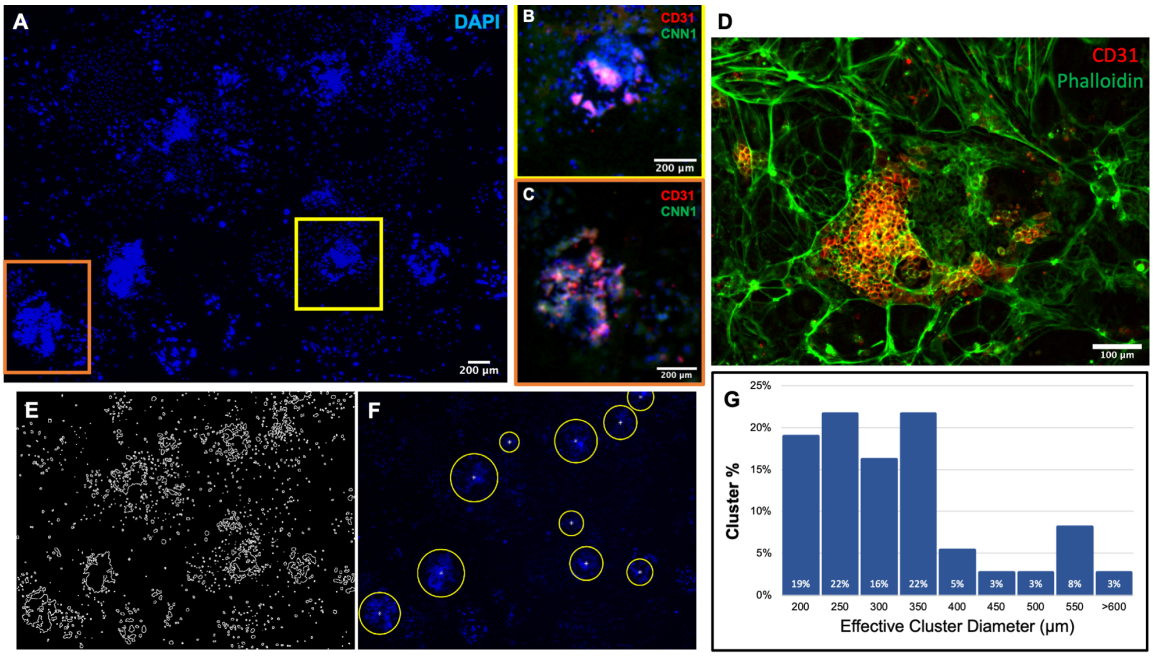

Appendix Figure S1 EC clusters emerge during differentiation.

A) Image taken at low magnification captures wide distribution of cellular nuclear stain, DAPI. Nuclear staining allowed for cluster analysis by capturing areas of dense cell clusters. **B-C)** Cropped images of clusters show, faint, CD31+ ECs (red), CNN1+ SMCs (green), and DAPI expression. Images show the CD31+ ECs mostly present within the center of dense DAPI clusters, while CNN1+ SMCs are mostly found on the periphery of these clusters. **D)** A cell cluster stained for CD31+ ECs counterstained with phalloidin (green). Phalloidin binds to F-actin, a common cytoskeleton protein. **E-G)** A custom MATLAB script was used to identify EC clusters and determine the effective cluster diameters distribution from the DAPI stain. **E)** Shows the binary outline of the DAPI stain after some image processing. **D)** Dense clusters are then identified by thresholding their area, shown here encased by yellow circles with a white star identifying their center. **G)** Graph of the effective cluster diameter distribution, with a bin size of 50µm. Here the mean effective cluster diameter was calculated to be 340µm ± 110µm taken from a total of 4 experimental cultures.

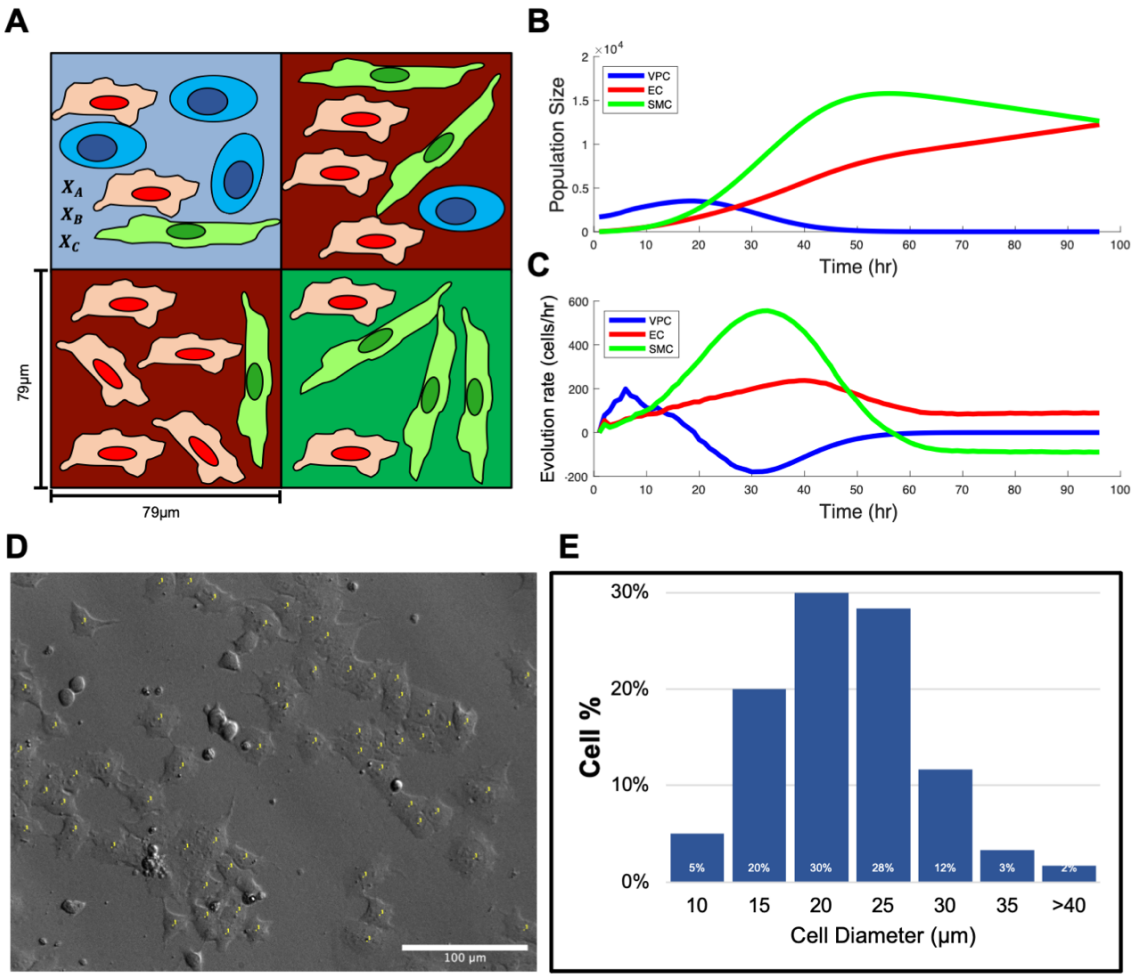

Appendix Figure S2 Relating simulations to experiments.

A) Schematic of a 2x2 lattice, where each lattice site has a length 79µm and can house a maximum of 10 cells. As the simulation evolves in time, the cell distributions are visualized by their RGB color assignment (red-EC, green-SMC, blue-VPC). While the simulation is running **B)** the total population size and **C)** evolution/devolution rates, a relative measurement of the number of cells added or removed between time steps, are tracked for all three cell types. In this example, we assume paracrine signaling with a □ value equal to 0.6. Additionally, motility, J_θ, was the same for all cell types at 0.0078 (corresponding to 14µm/hr), the proliferation, δ_θ, was set to 0.083 (12hrs) for VPCs and 0.059 (17hrs) for ECs and 0.045 (22hrs) SMCs. Lastly, the differentiation rate, α_θ, set to 0.016 (62.5hrs) and 0.01 (100hrs) for EC and SMC, respectively. Note* these are same conditions as supplementary Video S2. **B)** We observed the VPC population quickly falls to zero in response to VPC differentiation, i.e., VPCs turn into ECs and SMCs. **C)** Examining the evolution/devolution rates reveals the point at which these cells reach steady state, here occurring after 60hrs. **D)** Image of differentiating VPCs taken from time-lapse video (Supplementary video S1). **E)** Cell diameter distribution from **D,** with a bin size of 5µm.

Combinations:	**1A** = B cells **Induce** both B and C cells **1B** = Each **Induce** their own cells	**2A** = Opposite **induction** of cells **2B** = C cells **induce** both B and C cells
EC $\alpha_B =$ 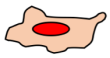	1 $\alpha_B\left(1 \pm \beta\left(\frac{X_B^i + \sum_{j \in n*n\ of\ i}(X_B^j)]}{X_{max}}\right)\right)$	OR $\alpha_B\left(1 \pm \beta\left(\frac{X_C^i + \sum_{j \in n*n\ of\ i}(X_C^j)]}{X_{max}}\right)\right)$ 2
	AND	
SMC $\alpha_C =$ 	A $\alpha_C\left(1 \pm \beta\left(\frac{X_B^i + \sum_{j \in n*n\ of\ i}(X_B^j)]}{X_{max}}\right)\right)$	OR $\alpha_C\left(1 \pm \beta\left(\frac{X_C^i + \sum_{j \in n*n\ of\ i}(X_C^j)]}{X_{max}}\right)\right)$ B
Paracrine signal strength: β = ±0.016; ±0.5		

Appendix Figure S3 Differentiation equations regulating cell-directed differentiation and alternate cell-directed differentiation.

Shown here are the combinations of equations that regulate same cell-directed differentiation and alternate cell-directed differentiation as well as other methods of sensing. Based on the exact combination, we can explore situations where cells induce either the same cell type or the opposite cell type, see combinations list for full details. Additionally, these equations depend on the β variable, defined as the paracrine signal strength, which acts to amplify or damp the sensed effect (for our purposes we explored β values equal to ± 0.5 and ± 0.016).

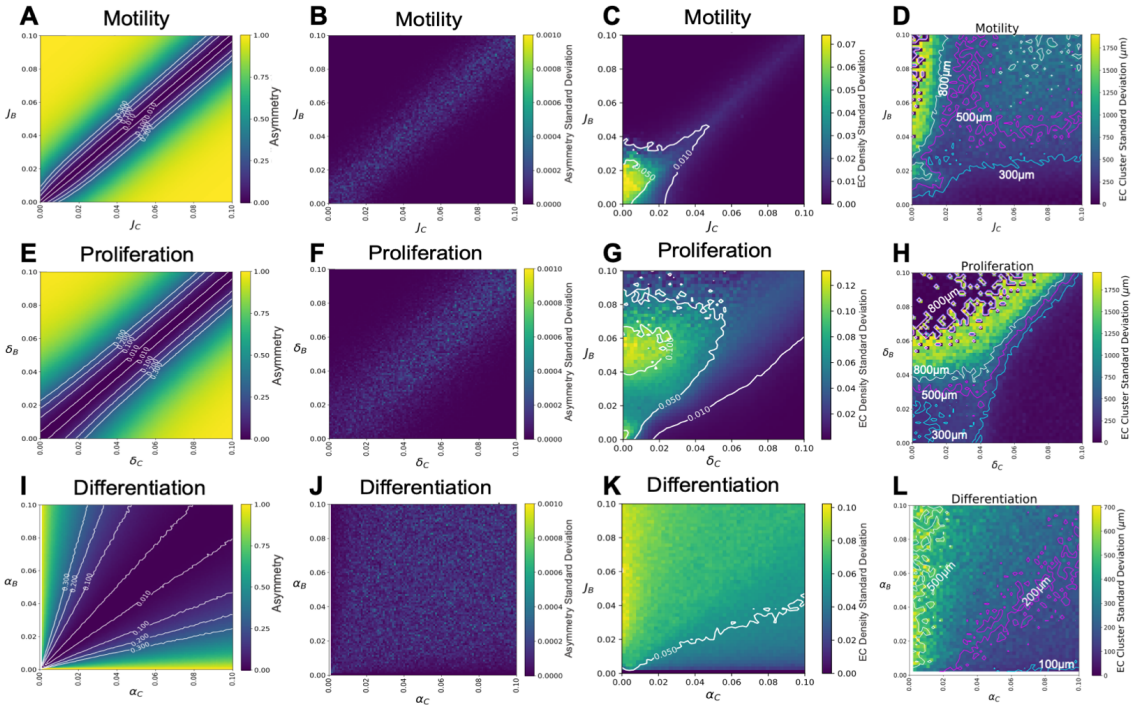

Appendix Figure S4 Cellular asymmetry plots under no sensing mechanism and standard deviation plots for Asymmetry, EC density, and EC cluster diameters.

Cell asymmetry measurements reflect the relative presence of EC and SMCs. With values close to 0 indicating roughly equal densities of both cell types, while values close to 1 denoting the presence of only cell types. In conditions where VPCs are no long present after 96hrs, these asymmetry graphs can serve as

useful indicators of pattern formation. Indeed, when compared to EC fraction parameter sweeps, they tend to mirror, and even better identify, the zone of co-emergence. Presented here are the cell asymmetry parameter sweeps for **A)** Motility, **E)** Proliferation, and **I)** differentiation. Contour lines here reflect the 0.01, 0.1, 0.2, and 0.3 boundaries. Parameter sweeps were run 10 times for Asymmetry and EC density while only 3 times for EC cluster diameters, thus allowing us to gauge the variance over repeated simulations. Shown here are the standard deviation graphs for motility parameter sweeps of **B)** asymmetry, **C)** EC density, and **D)** EC cluster diameter. As well as parameter sweeps of proliferation **F)** asymmetry, **G)** EC density, and **H)** EC cluster diameter. Lastly, the parameter sweeps of for differentiation, **J)** asymmetry, **K)** EC density, and **L)** EC cluster diameter.

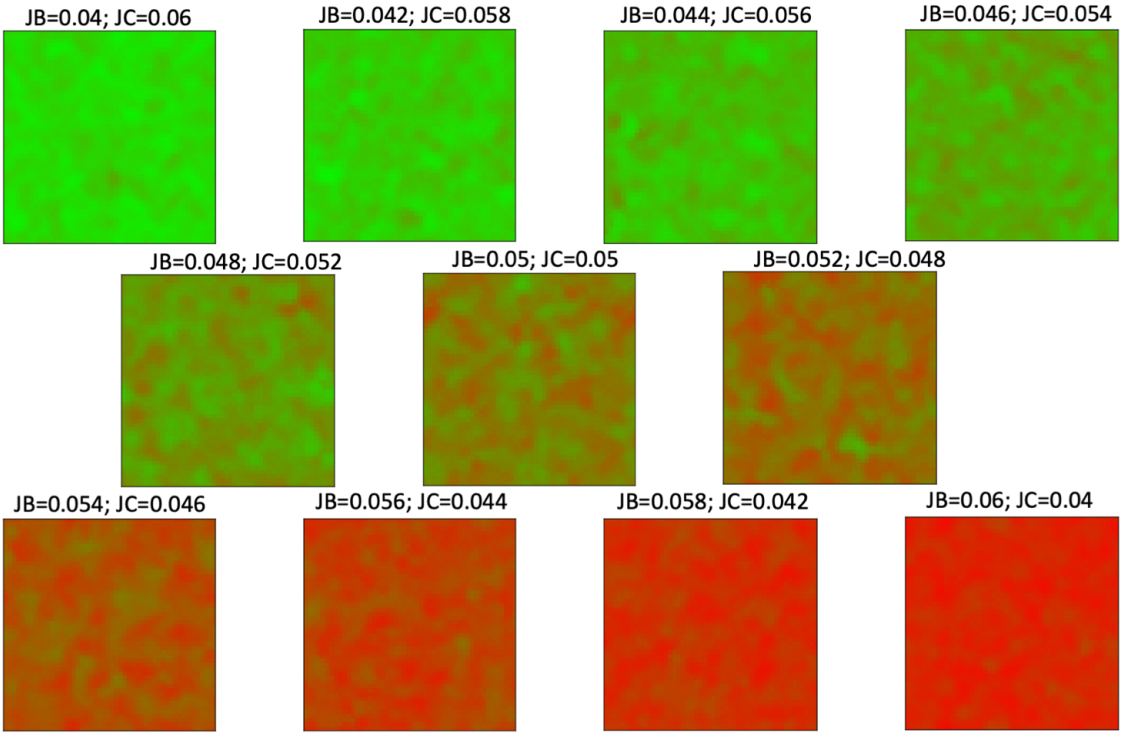

Appendix Figure S5 Cross-sectional scan of the zone of co-emergence as seen in the motility EC fraction parameter sweep.

Shown here are the individual micropattern simulations for values that cross the zone of co-emergence for the non-sensing motility EC fraction parameter sweep (Fig. 3A**)**. At the point of symmetry were J_B = 0.05 and J_C = 0.05, ECs (red) and SMCs (green) clusters emerge in roughly equal quantities. By varying the motility values away from the point of symmetry a preference towards one cell type becomes apparent and benefits the faster cell type (e.g., increase J_B, favors ECs, leading to more ECs in the simulation until they eventually fill the available space leaving little space for the SMCs to fill, and vice-versa).

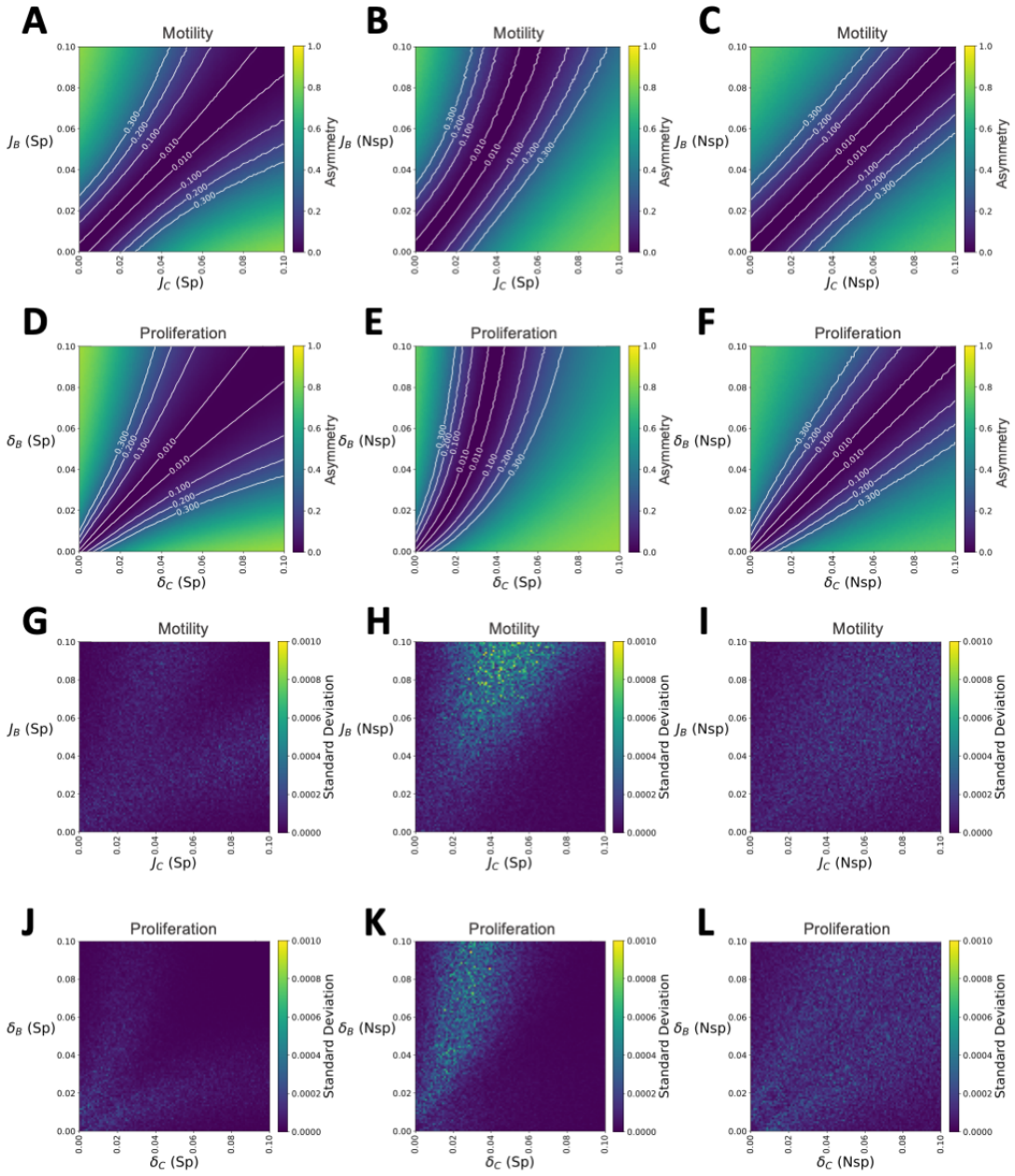

Appendix Figure S6 Cellular asymmetry plots under sensing mechanisms for motility and proliferation. Shown here are the cell asymmetry parameter sweeps for motility and proliferation under imposed sensing rules that govern the interactions VPCs, ECs, and SMCs have with each other. Explored here are specific cell adhesions (Sp) where only cells of the same identity will sense each other, and nonspecific cell adhesions (Nsp) which allows cells to sense all other cell types. The explored combinations are Specific-Specific, Nonpecific-Specific, and Nonspecific-Nonspecific for **A-C)** motility and **D-F)** proliferation, respectfully. Here values close to 0 indicate similar population densities, and the presence of patterning, while values closer to 1 denote the presence of only one cell type and thus no patterning. Simulations were run 10 times for the three conditions (Specific-Specific, Nonpecific-Specific, and Nonspecific-Nonspecific) and their standard deviations were calculated and plotted for **G-I)** motility and **J-L)** proliferation, respectfully.

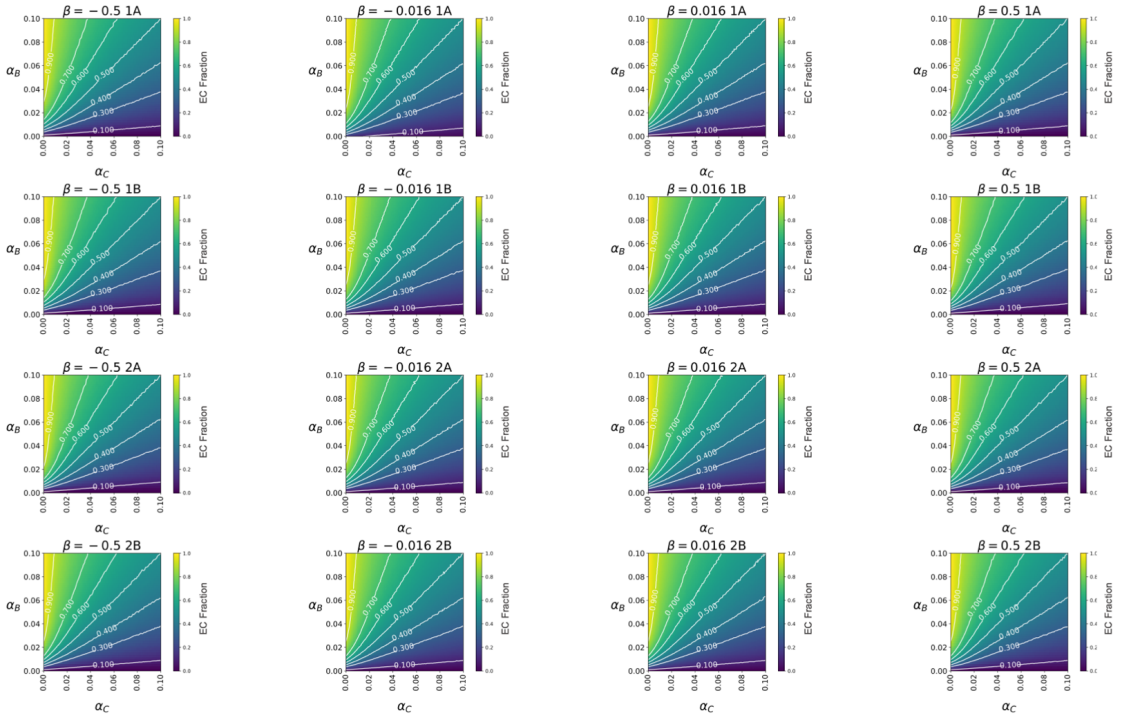

Appendix Figure S7 Total EC fraction results for differentiation under all sensing mechanisms.
Shown here are all the parameter sweeps for differentiation under the four different sensing mechanisms, and under the four different □ values (± 0.5 and ± 0.016). Condition 1A: ECs induce both EC an SMC differentiation. 1B: ECs induce the differentiation of ECs and SMCs induce the differentiation of SMCs, termed same cell-directed differentiation. 2A: ECs induce the differentiation of SMCs and SMCs induce the differentiation of ECs, termed alternate cell-directed differentiation. lastly 2B: SMCs induce both EC an SMC differentiation. Alas, there was no observable difference in the EC fraction plots for these different combinations.

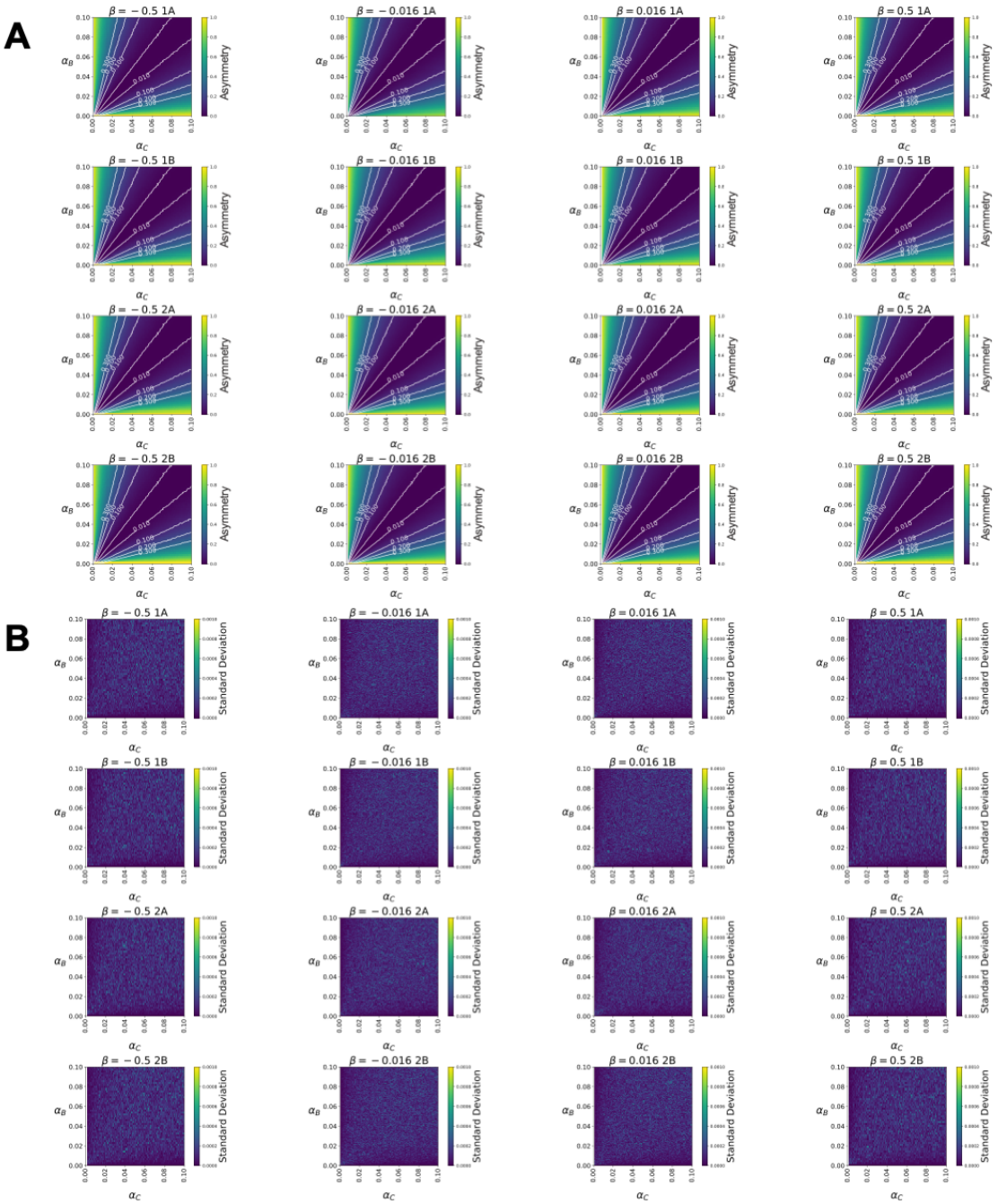

Appendix Figure S8 Cellular asymmetry plots, for differentiation under all sensing mechanisms.

A) Shown here are all the cell asymmetry parameter sweeps under the four different sensing mechanisms, and under the four different □ values (± 0.5 and ± 0.016). Condition 1A: ECs induce both EC an SMC differentiation. 1B: ECs induce the differentiation of ECs and SMCs induce the differentiation of SMCs. 2A: ECs induce the differentiation of SMCs and SMCs induce the differentiation of ECs. lastly 2B: is when SMCs induce both EC an SMC differentiation. Here values close to 0 indicate similar population densities, and in most cases the presence of patterning, while values closer to 1 denote the presence of only one cell type and thus no patterning. **B)** The corresponding standard deviations for the asymmetry parameter sweep taken from 10 replicated runs.

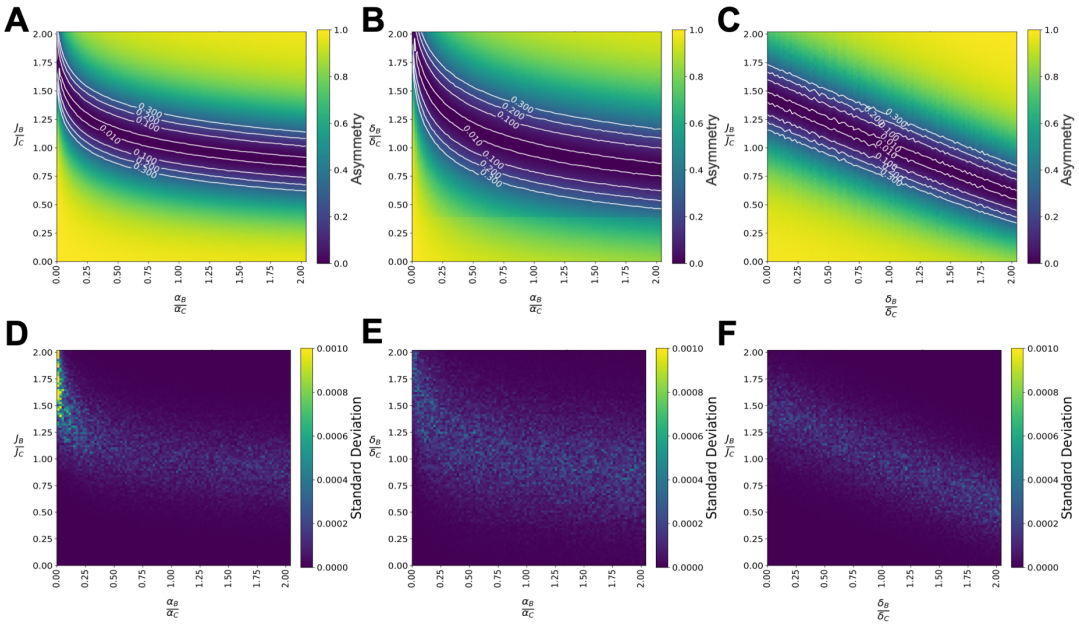

Appendix Figure S9 Multiparameter cellular asymmetry phase diagrams of micropatterning behavior.
A) Cell asymmetry phase diagram for relative ratios of motility (J_B/J_C) and differentiation (α_B/α_C). Here the motility of SMCs (J_C) is fixed at 14 μm^2/hr while EC motility (J_B) is varied between no motion and twice that SMC motility. For differentiation, SMC differentiation (α_C) is fixed at a differentiation rate of 62.5 hrs and EC differentiation (α_B) is varied between cells differentiating at twice that rate to cells that never differentiate. **B)** Cell asymmetry phase diagram for relative ratios of proliferation (δ_B/δ_C) and differentiation (α_B/α_C). Here SMC proliferation (δ_C) is fixed at a rate of one cell division every 40 hrs, and ECs proliferation is varied between no cell divisions to twice the rate of SMCs. **C)** Cell asymmetry phase diagram for relative values of motility and proliferation. **A-C)** Values close to 0 indicate similar population densities, and the presence of patterning, while values closer to 1 denote the presence of only one cell type and thus no patterning. **D-F)** The standard deviations for these phase diagrams were taken from 10 replicated simulations. Shown here **D)** motility and differentiation, **E)** proliferation and differentiation, and **F)** motility and proliferation.

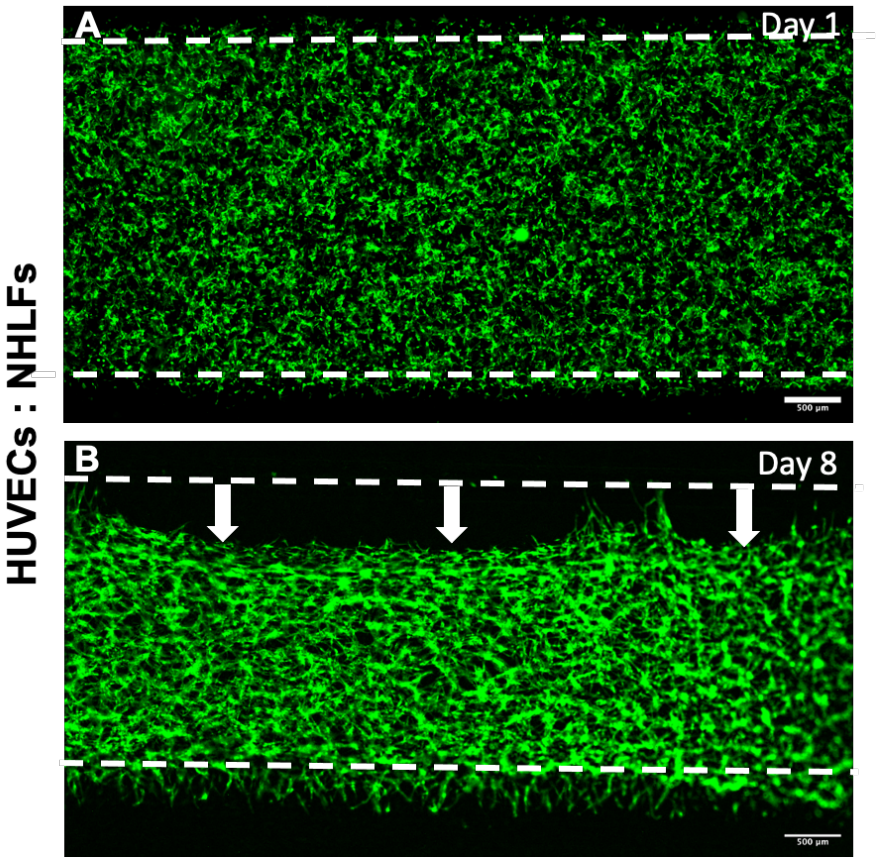

Appendix Figure S10 Compaction of HUVEC and NHLF co-cultures.

Shown here are fluorescent images of GFP-tagged HUVECs seeded in the center channel of the microfluidic device. Cultures of HUVECs and NHLFs were seeded at a 1:1 ratio at $4x10^6$ cells/mL. **A)** shows the culture at Day 1 post seeding, and **B)** shows the cultures at day 8 when they have started to undergo compaction. The white dashed lines demarcate the edges of the center channel. Scale bars are 500mm.

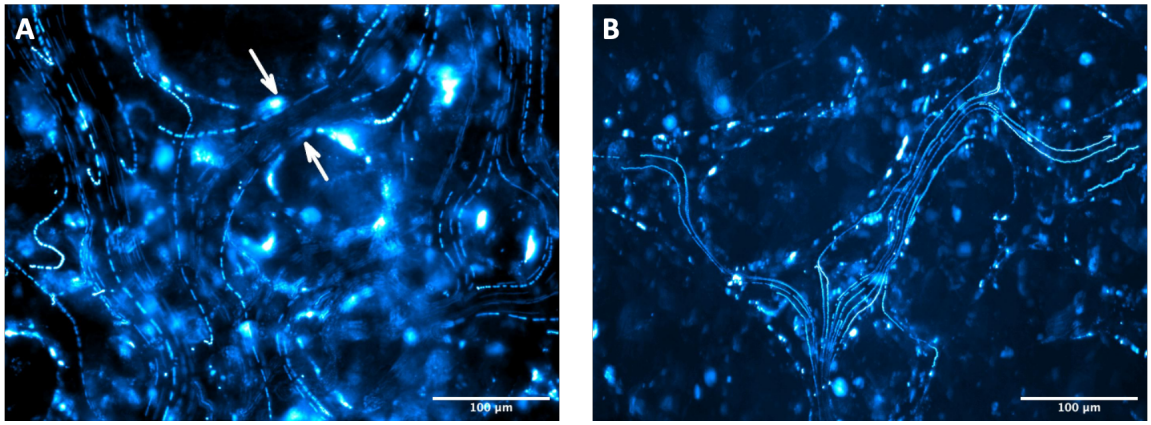

Appendix Figure S11 Perfusion of vascular networks containing mural cells.

A) Shows a long-exposure image of the vascular networks with the various bead paths. The vascular network is composed of HUVECs and HuAoSMCs seeded at $4x10^6$ cell/mL at a ratio of 1:1 on day 8. **B)** Shows a long-exposure image with the bead paths within the vascular network composed of HUVECs, HuAoSMCs and HBM-PCs seeded at $4x10^6$ cell/mL at a ratio of 10:10:1, respectfully, on day 10.

https://osf.io/h2mdt/files/osfstorage/65b028a899d01004c9626719

Appendix Supplemental Video 1: Time-lapse video of differentiating VPCs

Shown here is a 24h time-lapse video of R1 VPCs taken during day 1-2 of post differentiation supplemented with stage 2 differentiation medium.

https://osf.io/h2mdt/files/osfstorage/65b02acbebe5e60586f5e347

Appendix Supplemental Video 2: Simulation of emerging micropattern.

Video of simulation shows the emergence of EC (red) and SMC (Green) micropatterning from a starting VPCs population, the starting density is equivalent to a seeding density of 10k cells/cm^2. In this example, we assume paracrine signaling, which benefits SMC differentiation (condition 1A), and with a β value equal to 0.6. Additionally, migration, J_θ, was the same for all cell types at 0.0078 (corresponding to 14μm/hr), the proliferation, δ_θ, was set to 0.083 (12hrs) for VPCs and 0.059 (17hrs) for ECs and 0.045 (22hrs) SMCs. Lastly, the differentiation rate, α_θ, set to 0.016 (62.5hrs) and 0.01 (100hrs) for EC and SMC, respectively.

https://osf.io/h2mdt/files/osfstorage/65b17750973819063239764d

Appendix Supplemental Video 3: Branching networks emerge under co-cultures of HUVECs and HBM-PC:

Video shows a branch composed of HUVECs sprouting in the z-direction on day 8 of co-culture with HBM-PC. Here the GFP-HUVECs have been pseudo-colored blue. Scale bar is 100μm.

https://osf.io/h2mdt/files/osfstorage/65b185b64aa63c0682df1ca8

Appendix Supplemental Video 4: Perfusion of vessels composed of GFP-HUVECs with HuAoSMCs

Video shows vascular networks composed of GFP-HUVECs, pseudo-colored blue, and HuAoSMCs are perfusable by day 9. Fluorescent beads, 1μm, are flowed through the vasculature. Arrows points at narrow vessel passes where cells are flowed through. Scale bar is 100μm.

https://osf.io/h2mdt/files/osfstorage/65b17503b1f2b50650b0e6c1

Appendix Supplemental Video 5: Brightfield perfusion of vessels emerging from GFP-HUVECs with mural cells

Brightfield video shows vascular networks composed of GFP-HUVECs and mural cells, HuAoSMCs and HBM-PCs, are perfusable by day 9. Here asymmetric flow is applied to the microfluidic devices to flush out cellular debris. Shown here is the path that this debris will follow. Scale bar is 100μm.

https://osf.io/h2mdt/files/osfstorage/65b175e399d0100606626cfe

Appendix Supplemental Video 6: Perfusion of vessels composed of GFP-HUVECs with mural cells on day 10

Video shows vascular networks composed of GFP-HUVECs, pseudo-colored blue, and mural cells, HuAoSMCs and HBM-PCs, showing perfusable networks on day 10. Fluorescent beads, 1μm, are flowed through the vasculature. Scale bar is 100μm.

https://osf.io/h2mdt/files/osfstorage/65b1706a99d0100605626a03

Appendix Supplemental Video 7: Complex vascular networks are present at day 53 under tri-culture condition

Z-stack of only GFP-HUVECs imaged by confocal microscope, Woo Lab, on day 53. HUVECs are pseudo-colored cyan. Z-stack acquisition rage was 380μm with a 2μm step size.

https://osf.io/h2mdt/files/osfstorage/65b170114aa63c0677df1c2b

Appendix Supplemental Video 8: Pericytes wrapping around vasculature on day 53

Z-stack of GFP-HUVECs with RFP-HBM-PCs imaged by confocal microscope, Woo Lab, on day 53. HUVECs here are green and HBM-PC are red. Z-stack acquisition rage was 38μm with a 2μm step size.